ANALYTICAL AND EXPERIMENTAL INVESTIGATION OF A TURBULENT MIXING LAYER OF DIFFERENT GASES IN A PRESSURE GRADIENT

Thesis by

Manuel R. Rebollo

In Partial Fulfillment of the Requirements

For the Degree of

Doctor of Philosophy

California Institute of Technology
Pasadena, California

1973

(Submitted November 1972)

ACKNOWLEDGMENTS

The author wishes to express his appreciation to his advisor, Professor Anatol Roshko, for his guidance and direction of the present research. In addition, the timely advice of Professor Donald Coles is gratefully acknowledged.

Special thanks go to Dr. G. L. Brown for his assistance during the early part of the experiments. The author appreciates the cooperation of Mr. Jimenez Sendin on the development of the asymptotic behavior of the numerical solution.

It is a pleasure to thank Mrs. Geraldine Krentler for typing the manuscript.

The author is indebted to the California Institute of Technology, the European Space Research Organization, the National Aeronautics and Space Administration, and the Spanish Government for their financial assistance. The research was supported by the Department of the Navy, Office of Naval Research.

The deepest appreciation of all is felt for the author's wife, Paquita, and daughter, Maria del Carmen, for their encouragement, sacrifice, understanding, and diversion during the difficult years.

ABSTRACT

An analytical and experimental study has been made of the turbulent mixing layer in a pressure gradient. Theory predicts the possible existence of equilibrium flows, and this was confirmed experimentally for turbulent shear layers between streams of helium and nitrogen.

The only case for which similarity is possible is for $\rho_2 U_2^2 = \rho_1 U_1^2$, since then $P_2(x) = P_1(x)$. These equilibrium flows are of the form $U_1 \sim x^{\alpha}$ and $\delta \sim x$, where $\alpha = \frac{x}{U_1} \frac{dU_1}{dx}$ is a non-dimensional pressure gradient parameter.

The experimental investigation was conducted in the facility designed by Brown to produce turbulent flows at pressures up to 10 atmospheres. The adjustable walls of the test section of the apparatus were modified in order to set the pressure gradient.

Shadowgraphs of the mixing zone for $\alpha = 0$ and $\alpha = -0.18$, at different Reynolds numbers, revealed a large scale structure noticeably different for each α.

The similarity properties of the shear layer were established from mean profiles of total head and density. In addition, the rms density fluctuations were found to be self-preserving. From the mean profiles, the spreading rate, turbulent mass diffusion, Reynolds stress and Schmidt number distributions were calculated from the equations of motion.

The experimental results show that the spreading rate for the adverse pressure gradient is 60% greater than for the $\alpha = 0$ case. The

maximum shearing stress is 70% larger and the maximum value of the turbulent mass diffusion is 20% larger than their $\alpha = 0$ counterparts. The maximum rms density fluctuations are approximately 0.2 in both flows.

Surprisingly low values of turbulent Schmidt numbers were found; e.g., at the dividing streamline $Sc_t \doteq 0.16$ for $\alpha = 0$ and $Sc_t \doteq 0.33$ for $\alpha = -0.18$.

TABLE OF CONTENTS

TABLE OF CONTENTS (cont'd.)

TABLE OF CONTENTS (cont'd.)

TABLE OF CONTENTS (cont'd.)

NOMENCLATURE

C_d	constant in equation (3. 1. 2)
C_μ	constant in equation (3. 1. 2)
$\mathfrak{D}_t$	eddy diffusivity
f	normalized non-dimensional profile of mean velocity U
h	dimensionless maximum slope thickness (equation (9. 2. 1))
p	pressure
P	mean pressure
S	non-dimensional turbulent mass diffusion = $\frac{\overline{\rho' v'}}{\rho_1 U_1}$
Sc_t	turbulent Schmidt number = $\frac{\nu_t}{\mathfrak{D}_t}$
u	velocity in direction x
$\sqrt{\overline{u'^2}}$	rms velocity fluctuation in direction x
U	mean velocity in direction x
U_{10}	high speed velocity at the exit of the nozzle
U_{20}	low speed velocity at the exit of the nozzle
v	velocity in direction y
$\sqrt{\overline{v'^2}}$	rms velocity fluctuation in direction y
V	mean velocity in direction y
x	streamwise coordinate
x_o	displacement of virtual origin from coordinate origin
y	transverse coordinate
α	non-dimensional pressure gradient parameter = $\frac{x}{U_1}\frac{dU_1}{dx}$
β	constant in equation (2. 2. 8) = $\frac{d\delta}{dx}$
γ	constant = $\frac{C_\mu}{\beta}\frac{\Delta U}{U_1}$
δ	characteristic dimension in the transverse direction

NOMENCLATURE (cont'd.)

δ_1 thickness in the dynamic pressure profile; defined by distance between maximum and minimum

δ_2 thickness in the density profile; defined by distance between points corresponding to $\frac{\rho}{\rho_1} = 1.60$ and $\frac{\rho}{\rho_1} = 6.40$

ΔU reference velocity difference = $U_1 - U_2$

η similarity variable = $\frac{y}{x} \Big/ \frac{d\delta}{dx}$

η_o location of the dividing streamline

λ constant in equation (2.2.9) = $\frac{\delta}{U_1} \frac{dU_1}{dx}$

μ viscosity

ξ similarity variable = $\frac{y}{x}$

ρ density

$\sqrt{\overline{\rho'^2}}$ rms density fluctuation

τ non-dimensional Reynolds shear stress = $-\frac{\overline{\rho u'v'}}{\rho_1 U_1^2}$

Φ non-dimensional stream function = $\frac{\Psi}{\delta \rho_1 U_1}$

Ψ stream function

Subscripts and Superscripts

$(\ )_1$ free stream conditions on high speed side

$(\ )_2$ free stream conditions on low speed side

$(\ )'$ fluctuating quantity about the time average

$\overline{(\ )}$ time average

$\tilde{(\ )}$ mass weighted time average

LIST OF TABLES

LIST OF FIGURES

LIST OF FIGURES (cont'd.)

LIST OF FIGURES (cont'd.)

I. INTRODUCTION

The present work had its prime motivation from a continuing effort at the California Institute of Technology directed towards the understanding of heterogeneous turbulent mixing.

Within the framework of that aim a new facility was constructed several years ago, and the first investigations were carried out by Brown and Roshko (Ref. 1) on turbulent mixing layers between two streams of different gases.

During the course of those investigations it was realized that it should be possible to establish equilibrium turbulent mixing layers in pressure gradients, for particular combinations of the free stream parameters. This led to the present research.

1.1 Previous Investigations

Equilibrium flows are rather scarce due to the fact that they exist only for properly adjusted external pressure gradients, and for special combinations of the parameters involved in the problem. Two examples are well known in the case of boundary layers:

a) In the laminar boundary layer case the ordinary differential equation was first deduced by Falkner and Skan, and is widely reported in the literature; its solutions were later investigated in detail by D. R. Hartree (Ref. 2).

b) For the case of turbulent boundary layers, a very thorough experimental analysis was performed by Clauser (Ref. 3), who was able to establish self-similar turbulent boundary layers in adverse pressure gradients.

For turbulent jets and wakes in pressure gradients the theoretical conditions for the existence of similarity solutions of the boundary layer equations were set out by Townsend (Ref. 4), Wygnanski and Fiedler (Ref. 5), and Gartshore and Newman (Ref. 6), but the only relevant experiments were carried out by Gartshore (Ref. 7) on a two-dimensional wake, and Fekete (Ref. 8) on a two-dimensional jet in streaming flow.

Very little research has been done on the case of a homogeneous mixing layer in a pressure gradient. One of the few works in this area has been that of Sabin (Ref. 9) who found "a self-similar solution to an approximate equation which is not dependent upon a particular choice of either the eddy viscosity or pressure gradient". It should be noted here that no equilibrium flow or similarity solution, in the precise sense of the word, exists for the plane, homogeneous, turbulent mixing layer in any type of pressure gradient. The reason for this is that the only case for which similarity is possible is for $\rho_2 U_2^2 = \rho_1 U_1^2$, which can occur only for $\rho_2 \neq \rho_1$*.

During the course of Brown and Roshko's investigations on the case $\rho_2 U_2^2 = \rho_1 U_1^2$ for zero pressure gradient it was realized, by arguing in physical terms, that the only way an equilibrium mixing layer in a pressure gradient could be established was by having $\rho_2 U_2^2 = \rho_1 U_1^2$, since then $P_2(x) = P_1(x)$ and the rate of change of the free stream velocities with the downstream coordinate is such that $\frac{U_2(x)}{U_1(x)}$ = constant for all x. Doing the theoretical analysis on the

* Sabin was aware of the problem as can be deduced from his paper.

equations of motion* it turns out that these equilibrium flows are of the form $U_1 \sim x^{\alpha}$ and $\delta \sim x$, where δ is a characteristic thickness; i.e., the shear layer still grows linearly in x. The non-dimensional pressure gradient parameter is $\alpha = \frac{x}{U_1}\frac{dU_1}{dx} = \frac{x}{U_2}\frac{dU_2}{dx}$ = constant. Clearly, for $\alpha = 0$, U_1 = const and U_2 = const (zero pressure gradient); for $\alpha > 0$ the flow is accelerated (favorable pressure gradient); and for $\alpha < 0$ the flow is decelerated (adverse pressure gradient).

1.2 Goals of the Present Study

Much attention has been given to the problem of free turbulent mixing, due to the fact that a large number of flow configurations of engineering significance are related to this process, as is the case for fully separated flows, where an important element is the shear layer which develops behind the separation point. Turbulent mixing with large density non-uniformities plays a very important role in combustion, chemical mixing of different species, and more recently in chemical lasers. In most of these important flows the pressure varies along the streamwise direction; therefore the analysis of these cases requires knowledge of the properties of the heterogeneous turbulent mixing layer in a pressure gradient.

Our main interest was in trying to find equilibrium solutions, since the study of these configurations is simpler than that of non-preserving flows; the former are of fundamental importance to provide insight for the more complicated flow cases.

---

* See section II for a more detailed account.

From the equations of motion we found the conditions for the existence of similarity. Once the boundary-layer equations were reduced to ordinary differential equations we obtained numerical solutions by using the hypotheses of constant eddy viscosity and eddy diffusivity. The procedure contains two empirical constants left free to be adjusted from experiment.

In the experimental work, external pressure gradient of the form prescribed by the theory was imposed upon a two-dimensional turbulent mixing layer between streams of nitrogen and helium with equal dynamic pressures, with the following goals in mind. First, profiles of mean total head and density at several downstream stations were desired so that the possible similarity flow found analytically could be verified; measurements of rms density fluctuations were sought to the end that self-preservation of the turbulent quantities as set out by Townsend's criteria could be established. Second, a determination of the basic flow parameters, e.g., spreading rate, shear stress, turbulent mass diffusion and Schmidt number distributions were required. Finally, measurements for the case of zero pressure gradient were desired for reasons of completeness.

We should mention that a photographic investigation, by means of shadowgraphs, was conducted, partially as a guide in setting up the flow and getting the data, and partially as a visual check of some of the results that were going to be found during the experiments, e.g., spreading angle.

1.3 Experimental Techniques

The experimental investigation was carried out in the facility designed by Brown to produce turbulent flows at pressure up to 10 atmospheres with very short running times.

Because of the short duration of the flow, only a few seconds, high-speed measurement techniques were used.

The side walls of the test section of the apparatus (Ref. 1) were changed for adjustable slats and a perforated plate was added at the channel exit.

The highest speeds were 1000 cm/sec for the light gas and 378 cm/sec for the heavy one. Experiments were made at three different tank pressures (7, 4 and 2 atmospheres) to study the behavior of the mixing layer at different Reynolds numbers. Mean dynamic pressure profiles were obtained at several downstream locations using a fast electronic manometer (Barocel) and a pitot tube. Analog signals from the Barocel were converted through an A/D converter, to digital form and written on magnetic tape. A Kennedy Incremental Tape Recorder was used for this purpose.

Composition measurements of the binary mixture were made at several downstream locations using an aspirating probe developed by Brown and Rebollo (Ref. 10)*. A very fast data acquisition system (Data Slicer), designed by Coles, was used; first, to traverse the aspirating probe across the shear layer; second, to command the A/D conversion of the analog voltage coming from the feedback bridge of

---

* See Appendix B.

the hot wire; and third, to control the writing of the digital signal on magnetic tape for later computer processing. The recording of the data was by means of a Kennedy Synchronous Tape Recorder.

Sections II and III contain the analytical study of the equations of motion and their numerical solution. A detailed description of the experimental equipment, instrumentation and the procedures used to acquire and process the data is given in sections IV through VII. The results and conclusions are presented in section VIII and IX.

II. ANALYTICAL STUDY OF EQUILIBRIUM FLOWS

2.1 Derivation of the Equations of Motion for Heterogeneous Flow

The equations of motion for an incompressible, two-dimensional flow in a non-uniform medium can be written as follows:

x-momentum

$$\frac{\partial(\rho u)}{\partial t} + \frac{\partial(\rho u^2)}{\partial x} + \frac{\partial(\rho uv)}{\partial y} = -\frac{\partial p}{\partial x} + \frac{\partial}{\partial x}\left(\mu\frac{\partial u}{\partial x}\right) + \frac{\partial}{\partial y}\left(\mu\frac{\partial u}{\partial y}\right) \qquad (2.1.1)$$

y-momentum

$$\frac{\partial(\rho v)}{\partial t} + \frac{\partial(\rho uv)}{\partial x} + \frac{\partial(\rho v^2)}{\partial y} = -\frac{\partial p}{\partial y} + \frac{\partial}{\partial x}\left(\mu\frac{\partial v}{\partial x}\right) + \frac{\partial}{\partial y}\left(\mu\frac{\partial v}{\partial y}\right) \qquad (2.1.2)$$

Continuity

$$\frac{\partial \rho}{\partial t} + \frac{\partial(\rho u)}{\partial x} + \frac{\partial(\rho v)}{\partial y} = 0 \qquad (2.1.3)$$

Gravitational forces have been neglected in the momentum equation.

Following Reynolds (1895) we divide the flow quantities into their mean and fluctuating parts:

$$u = U + u'$$

$$v = V + v'$$

$$p = P + p'$$

$$\rho = \bar{\rho} + \rho'$$

Substituting these expressions into (2.1.1), (2.1.2), and (2.1.3) and taking mean values we arrive at the equations of mean motion:

$$\frac{\partial}{\partial x}(\bar{\rho}U^2) + \frac{\partial}{\partial y}(\bar{\rho}UV + U\overline{\rho'v'}) = -\frac{\partial P}{\partial x} - \frac{\partial}{\partial y}(\overline{\rho u'v'}) \qquad (2.1.4)$$

$$\frac{\partial}{\partial y}(\overline{\rho v'^2}) = -\frac{\partial P}{\partial y} \qquad (2.1.5)$$

$$\frac{\partial}{\partial x}(\bar{\rho}U) + \frac{\partial}{\partial y}(\bar{\rho}V + \overline{\rho'v'}) = 0 \qquad (2.1.6)$$

after the following approximations have been made:

a) gradients in x are small compared with gradients in y (boundary layer approximation) i.e., $\left|\frac{\partial/\partial x}{\partial/\partial y}\right| \ll 1$

b) values of $\sqrt{\overline{u'^2}}$ and $\sqrt{\overline{v'^2}}$ are comparable

c) $\frac{\delta(x)\Delta U(x)}{\nu} \gg 1$, where $\delta(x)$ is a measure of the width of the shear zone, and $\Delta U(x)$ is a reference velocity difference at each cross section.

As a consequence of the above assumptions, the Reynolds stresses are supposed to be very large relative to the viscous stress for sufficiently high Reynolds numbers.

The only remaining equation is the diffusion equation which reduces to

$$\frac{\partial U}{\partial x} + \frac{\partial V}{\partial y} = 0 \qquad (2.1.7)$$

if the molecular diffusion is neglected, which is consistent, for a turbulent flow, with the approximations already made (Ref. 1). From equation (2.1.5) we get

$$P + \overline{\rho v'^2} = P_1(x) \qquad (2.1.8)$$

This expression can be used to replace $\frac{\partial P}{\partial x}$ in equation (2.1.4) and clearly within our present approximation we finally have*

$$\frac{\partial}{\partial x}(\rho U^2) + \frac{\partial}{\partial y}(\rho U\tilde{V}) = -\frac{dP_1(x)}{dx} - \frac{\partial}{\partial y}(\overline{\rho u'v'}) \qquad (2.1.9)$$

$$\frac{\partial}{\partial x}(\rho U) + \frac{\partial}{\partial y}(\rho\tilde{V}) = 0 \qquad (2.1.10)$$

$$\frac{\partial U}{\partial x} + \frac{\partial \tilde{V}}{\partial y} = \frac{\partial}{\partial y}\left(\frac{\overline{\rho'v'}}{\rho}\right) \qquad (2.1.11)$$

where $$\rho\tilde{V} = \rho V + \overline{\rho'v'} \qquad (2.1.12)$$

It should be noted that with this substitution the equation of continuity recovers its normal form, but a mass-weighted turbulent mass diffusion term appears in the right hand side of the diffusion equation.

2.2 Heterogeneous Turbulent Mixing Layer: Equilibrium Flow in a Pressure Gradient

Let us consider that at $x = 0$ there is a meeting of two parallel streams of different gases, densities ρ_1 and ρ_2, whose velocities are U_1 and U_2 respectively, it being assumed that $U_1 > U_2$. Downstream of the point of encounter the streams will form a mixing zone subject to a pressure gradient in the streamwise direction (Fig. 1).

To find the conditions for similarity when $\frac{dP_1(x)}{dx} \neq 0$, we assume following Townsend (Ref. 4), that

---

* From here on the dash on $\bar{\rho}$ will be dropped in order to simplify the notation.

$$\frac{U}{U_1} = u(\eta) \tag{2.2.1}$$

$$\frac{\rho}{\rho_1} = \rho(\eta) \tag{2.2.2}$$

$$-\frac{\overline{\rho u'v'}}{\rho_1 U_1^2} = \tau(\eta) \tag{2.2.3}$$

$$\frac{\overline{\rho' v'}}{\rho_1 U_1} = S(\eta) \tag{2.2.4}$$

where $U_1 = U_1(x)$

$\eta = y/\delta(x)$

$\delta(x)$ is a characteristic dimension in the transverse direction, i.e., a measure of the width of the mixing region.

The boundary conditions are as follows

$$\eta \to +\infty \begin{cases} u(\eta) \to 1 \\ \rho(\eta) \to 1 \end{cases}$$

$$\eta \to -\infty \begin{cases} u(\eta) \to \frac{U_2}{U_1} \\ \rho(\eta) \to \frac{\rho_2}{\rho_1} \end{cases}$$

Hence from the boundary conditions we deduce that $\frac{U_2(x)}{U_1(x)}$ has to be a constant.

Within the boundary layer approximation, we will have outside the layer, where $\frac{\partial U}{\partial y}$ is very small,

$$-\frac{dP_1(x)}{dx} = \rho_1 U_1 \frac{dU_1}{dx}$$

$$= \rho_2 U_2 \frac{dU_2}{dx} = -\frac{dP_2(x)}{dx}$$

After integration

$$\frac{U_1^2(x)}{2}\left(\rho_1 - \rho_2 \frac{U_2^2}{U_1^2}\right) = C$$

where C is a constant; but since $U_1 = U_1(x)$ and $\frac{U_2}{U_1}$ = const, this implies that C = 0; therefore in order to have $P_2(x) = P_1(x)$

$$\rho_1 U_1^2 = \rho_2 U_2^2 \quad , \quad \text{or} \quad \frac{U_2}{U_1} = \sqrt{\frac{\rho_1}{\rho_2}} \tag{2.2.5}$$

In homogeneous flow, $\rho_1 = \rho_2$, the only way to satisfy this condition is with $U_1 = U_2$, i.e., "no shear between the two streams."

Let us define a stream function $\Psi(x, y)$, such that the continuity equation is identically satisfied.

$$\rho U = \frac{\partial \Psi}{\partial y}$$

$$\rho \tilde{V} = - \frac{\partial \Psi}{\partial x}$$

where $\Psi(x, y)$ is made dimensionless, and assumed to be only a function of η, by the substitution

$$\Phi(\eta) = \frac{\Psi(x, y)}{\delta(x)\rho_1 U_1(x)}$$

Consequently, the relation between the velocity components and $\Phi(\eta)$ is given by

$$\frac{d\Phi}{d\eta} = \rho u \tag{2.2.6}$$

and

$$\rho \tilde{v} = \left(\frac{d\delta}{dx}\right) \eta \rho u - \frac{1}{U_I} \frac{dU_1 \delta}{dx} \Phi(\eta) \tag{2.2.7}$$

where $\tilde{v} = \frac{\tilde{V}}{U_1}$.

Introducing the non-dimensional quantities from (2. 2. 1), (2. 2. 2), (2. 2. 3), and (2. 2. 4) into the equations of motion, and after replacing $\tilde{v}$ for its expression in (2. 2. 7) we obtain

$$\frac{\delta(x)}{U_1(x)} \frac{dU_1(x)}{dx} (\rho u^2 - 1) - \left[\frac{d\delta(x)}{dx} + \frac{\delta(x)}{U_1(x)} \frac{dU_1(x)}{dx}\right] \int \frac{du}{d\eta} = \frac{d\tau}{d\eta}$$

$$- \left[\frac{d\delta(x)}{dx} + \frac{\delta(x)}{U_1(x)} \frac{dU_1(x)}{dx}\right] \int \frac{d(1/\rho)}{d\eta} = \frac{d}{d\eta}(S/\rho)$$

Similarity solutions exist only if

$$\frac{d\delta(x)}{dx} = \text{const} = \beta \qquad (2.2.8)$$

$$\frac{\delta(x)}{U_1(x)} \frac{dU_1(x)}{dx} = \text{const} = \lambda \qquad (2.2.9)$$

From these two equations the potential velocity $U_1(x)$ and the scale factor $\delta(x)$ for the ordinate can be evaluated.

$$\delta(x) \sim x \qquad (2.2.10)$$

$$U_1(x) \sim x^{\alpha} \qquad (2.2.11)$$

where $\alpha = \lambda/\beta$

$$= \frac{x}{U_1} \frac{dU_1}{dx}$$

In conclusion, the only case for which similarity is possible is when $\rho_2 U_2^2 = \rho_1 U_1^2$ and the equilibrium flows are of the form given by the equations (2. 2. 10) and (2. 2. 11).

The similarity form of the equations is

$$- \eta \frac{d(\rho u)}{d\eta} + \frac{1}{\beta} \frac{d(\rho \tilde{v})}{d\eta} + \alpha \rho u = 0 \qquad (2.2.12)$$

$$- \eta \frac{d(\rho u^2)}{d\eta} + \frac{1}{\beta} \frac{d(\rho u \tilde{v})}{d\eta} + \alpha (2 \rho u^2 - 1) = \frac{1}{\beta} \frac{d\tau}{d\eta} \qquad (2.2.13)$$

$$- \eta \frac{du}{d\eta} + \frac{1}{\beta} \frac{d\tilde{v}}{d\eta} + \alpha u = \frac{1}{\beta} \frac{d}{d\eta} (S/\rho) \qquad (2.2.14)$$

2.3 Shear Stress and Turbulent Mass Diffusion Distributions

Integrating the equation (2.2.6) we find that

$$\Phi(\eta) = \int_o^{\eta} \rho u \, dx$$

where at $\eta_b = 0$, $\Phi(\eta_o) = 0$

and $\tilde{v}(\eta_o) = 0$

η_o is the dividing streamline of the flow. Across this line the transport of mass is equal to zero.

To get the distributions of shear stress and turbulent mass diffusion across the layer we integrate the similarity equations.

Continuity yields

$$- (\xi u + \tilde{v}) \rho + (1 + \alpha) \int_o^{\xi} \rho u \, dx = 0 \qquad (2.3.1)$$

where $\xi = y/x$.

From the momentum equation (2.2.13) and after using continuity we have

$$- (1+\alpha) u \int_{\xi_o=0}^{\xi} \rho u dx + (1+\alpha) \int_{\xi_o=0}^{\xi} \rho u^2 dx + \alpha \int_{\xi_o=0}^{\xi} (\rho u^2 - 1) \, dx$$

$$= \tau(\xi) - \tau(\xi_o)_{\xi_o=0} \qquad (2.3.2)$$

Similarly, integrating (2. 2. 14) and after using equation (2. 3. 1), we obtain for the turbulent mass diffusion distribution

$$-\frac{(1+\alpha)}{\rho}\int_{\xi_o=0}^{\xi}\rho u\,dx + (1+\alpha)\int_{\xi_o=0}^{\xi} u\,dx = (S/\rho) - (S/\rho)_{\xi_o=0} \qquad (2.3.3)$$

Hence, if we measure the velocity and density profiles, and locate the dividing streamline on them, the shear stress and turbulent mass diffusion can be calculated from equations (2. 3. 2) and (2. 3. 3).

We should note that since

$$\left(\frac{d\tau}{d\xi}\right)_{\xi_o=0} = \alpha\,(\rho u^2 - 1)\Big|_{\xi_o=0} \qquad (2.3.4)$$

The maximum shearing stress occurs on the dividing streamline only for two cases: either

$$\alpha = 0, \text{ or } (\rho u^2 - 1)_{\xi_o=0} = 0$$

however

$$\left(\frac{d(S/\rho)}{d\xi}\right)_{\xi_o=0} = 0 \quad \text{for} \quad \begin{matrix}\alpha = 0 \\ \text{and} \\ \alpha \neq 0\end{matrix} \qquad (2.3.5)$$

A mass-weighted transverse velocity fluctuation $\frac{\overline{\rho' v'}}{\rho}$ is a maximum at $\xi = \xi_o$ independently of the pressure gradient.

2. 3a Location of the Dividing Streamline

Considering that $\tau(\xi)$ should tend towards zero at both edges of the mixing layer; we deduce from equation (2. 3. 2) that: as $\xi \to -\infty$

$$-\tau(\xi_o)_{\xi_o=0} = (1+\alpha)\int_{\xi_o=0}^{-\infty} \rho u\,(u - \frac{U_2}{U_1})\,dx + \alpha\int_{\xi_o=0}^{-\infty}(\rho u^2 - 1)dx \quad (2.3.6)$$

and when $\xi \to +\infty$

$$-\tau(\xi_o)_{\xi_o=0} = (1+\alpha)\int_{\xi_o=0}^{\infty} \rho u(u-1)dx + \alpha\int_{\xi_o=0}^{\infty}(\rho u^2 - 1)dx \quad (2.3.7)$$

Consequently

$$(1+\alpha)\int_{\xi_o=0}^{\infty} \rho u(u-1)dx + \alpha\int_{\xi_o=0}^{\infty}(\rho u^2 - 1)dx$$

$$= (1+\alpha)\int_{\xi_o=0}^{-\infty} \rho u(u - \frac{U_2}{U_1})dx + \alpha\int_{\xi_o=0}^{-\infty}(\rho u^2 - 1)dx \quad (2.3.8)$$

will define $\xi_o=0$ in our experimental profiles.

Following the same procedure an equation for $\xi_o=0$ can also be found from equation (2.3.3)

$$-(S/\rho)_{\xi_o=0} = (1+\alpha)\int_{\xi_o=0}^{\infty} u(1-\rho)dx \quad (2.3.9)$$

$$-(S/\rho)_{\xi_o=0} = (1+\alpha)\int_{\xi_o=0}^{-\infty} u(1 - (\frac{\rho}{\rho_2/\rho_1}))dx \quad (2.3.10)$$

Hence

$$\int_{\xi_o=0}^{\infty} u(\rho-1)dx = \int_{-\infty}^{\xi_{o=0}} u(1 - \frac{\rho}{(\rho_2/\rho_1)})dx \quad (2.3.11)$$

is also an equation for determining the position of $\xi_o=0$ from our experimental data.

Naturally both equations ought to give the same location for ξ_o.

2.3b Mass Flow Entrainment

We can define the mass entrainment as $\rho\tilde{v}(\xi)$ when $|\xi| \to \infty$, but subtracting from it the value which exists in conjunction with the pressure gradient.

From equation (2.3.1) we have

$$\rho\tilde{v} = \xi\rho u - (1 + \alpha) \int_{\xi_o=0}^{\xi} \rho u dx$$

as $\xi \to \pm\infty$ and taking into account the boundary conditions we arrive at

$$\frac{\rho_1 V(+\infty)}{\rho_1 U_1} = \underbrace{- \int_{\xi_o=0}^{\infty} (\rho u - 1) dx}_{\text{Entrainment}} - \alpha \int_{\xi_o=0}^{\infty} \rho u dx \qquad (2.3.12)$$

$$\frac{\rho_2 V(-\infty)}{\rho_1 U_1} = \underbrace{- \int_{\xi_o=0}^{-\infty} \left(\rho u - \frac{\rho_2 U_2}{\rho_1 U_1}\right) dx}_{\text{Entrainment}} - \alpha \int_{\xi_o=0}^{-\infty} \rho u dx \qquad (2.3.13)$$

The last term in each equation is connected with the existence of the pressure gradient, and is left out of our definition of mass entrainment.

III. NUMERICAL SOLUTION OF THE EQUATIONS

3.1 Eddy Viscosity and Eddy Diffusivity Model

In order to predict any turbulent flow a certain number of assumptions have to be made about the Reynolds transport terms. Accuracy and scope of the predictions are normally dependent upon the equations chosen for the closure of the system.

During the Langley Working Conference on Turbulent Free Shear Flows in 1972 a wide and representative spectrum of turbulence models were presented*. Two general techniques that have been used extensively to evaluate the needed turbulence input are the eddy-viscosity and the turbulent kinetic energy approaches.

Of the current alternatives available for modeling the turbulent transport terms we should indicate that, since our primary interest is devoted to establishing the possibility of equilibrium flows which have been found in section II, we have used a very simple eddy viscosity and diffusivity model in order to give us a qualitative idea of what to expect from the experiments. Naturally, the election of this or any other turbulent model would yield the same form of the growth laws for the equilibrium flows.

We therefore assume

$$\text{(a)} \quad \overline{\rho' v'} = - \mathcal{D}_t \frac{\partial \rho}{\partial y} \qquad \overline{\rho u' v'} = - \rho \nu_t \frac{\partial U}{\partial y} \tag{3.1.1}$$

---

* Some of these models representing different approaches are given in references 11-22.

(b) $\mathcal{D}_t = C_d \, \delta \, \Delta U$ *

$$\nu_t = C_\mu \, \delta \, \Delta U \qquad (3.1.2)$$

Substituting these assumptions into the similarity form of the equations we get:

Continuity

$$AX + A' + u(1 + \alpha) = 0 \qquad (3.1.3)$$

Momentum

$$AY + \alpha(\rho u^2 - 1) = \frac{C_\mu}{\beta} \frac{\Delta U}{U_1} Y' \qquad (3.1.4)$$

Diffusion

$$A' + u(1 + \alpha) = - \left(\frac{C_\mu}{\beta} \frac{\Delta U}{U_1}\right) \frac{1}{Sc_t} X' \qquad (3.1.5)$$

where

$$A = - \eta u + \frac{\tilde{v}}{\beta} \qquad (3.1.6)$$

$$X = \frac{1}{\rho} \frac{d\rho}{d\eta} \qquad (3.1.7)$$

$$Y = \rho \frac{du}{d\eta} \qquad (3.1.8)$$

$Sc_t = \dfrac{\nu_t}{\mathcal{D}_t}$ (turbulent Schmidt number)

with boundary conditions

$$\eta \to +\infty \begin{cases} \rho \to 1 \\ u \to 1 \end{cases}$$

$$\eta \to -\infty \begin{cases} \rho \to \rho_2/\rho_1 \\ u \to U_2/U_1 \end{cases}$$

---

* $\delta = \delta(x)$
$\Delta U = U_1 - U_2$

3.2 Zero Pressure Gradient Case: $\alpha = 0$

When no pressure gradient is imposed upon the mixing layer, U_1 = constant and $\alpha = 0$, hence, replacing this value of α into the equations and after eliminating $A' + u(1 + \alpha)$ out of the continuity and diffusion equations we find

$$AX = \frac{\gamma}{Sc_t} X'$$

$$AY = \gamma Y'$$

where $$\gamma = \frac{C_\mu \Delta U}{\beta U_1}$$

Consequently

$$Sc_t \frac{Y'}{Y} = \frac{X'}{X}$$

Integrating twice, and after using the boundary conditions to calculate the two constants of integration, we will have a direct relationship between $\rho(\eta)$ and $u(\eta)$; if we now set

$$u(\eta) = \frac{U_1 + U_2}{2 U_1} \left(1 + \frac{U_1 - U_2}{U_1 + U_2} f(\eta)\right)$$

we finally arrive at

$$\rho(\eta) = \left\{ 1 + \frac{\left(\frac{\rho_2}{\rho_1}\right) - 1}{\int_{-\infty}^{\infty} [f'(x)]^{Sc_t} dx} \int_{\eta}^{\infty} [f'(x)]^{Sc_t} dx \right\}^{-1/Sc_t} \qquad (3.2.1)$$

From the momentum equation, and taking into account that

$$A(\eta) = -\frac{1}{\rho} \int_{\eta_o = 0}^{\eta} \rho u \, dx$$

we deduce

$$- f' \int_{\eta_o=0}^{\eta} \rho \left(1 + \frac{U_1 - U_2}{U_1 + U_2} f(x)\right) dx = 2 \frac{C_\mu}{\beta} \left(\frac{U_1 - U_2}{U_1 + U_2}\right) \frac{d}{d\eta}(\rho f')$$

After multiplying and dividing the left hand side by $\rho(\eta)$, defining β such that,

$$\frac{C_\mu}{\beta} \left(\frac{U_1 - U_2}{U_1 + U_2}\right) = \frac{1}{2}$$

and integrating we get

$$f'(\eta) = \frac{f'(0)\ \rho(0)}{\rho(\eta)}\ e^{-\int_{\eta_o=0}^{\eta} \frac{1}{\rho} \left(\int_0^x \rho\left(1 + \frac{U_1 - U_2}{U_1 + U_2} f(\zeta)\right) d\zeta\right) dx} \qquad (3.2.2)$$

We should note that the linearized result $\frac{U_1 - U_2}{U_1 + U_2} << 1$ for ρ = const reduces to the solution obtained by Görtler (Ref. 23); if our definition of β is made compatible with his, namely

$$\frac{C_\mu}{\beta} \left(\frac{U_1 - U_2}{U_1 + U_2}\right) = \frac{1}{4}$$

then

$$f'(\eta) = f'(0)\ e^{-\eta^2}$$

$$f(\eta) = f(0) + f'(0) \int_0^{\eta} e^{-x^2} dx$$

and from the boundary conditions

$$\eta = \pm \infty \ ; \ f(\eta) = \pm 1$$

we get

$$f(0) = 0$$

$$f'(0) = \frac{2}{\sqrt{\pi}}$$

Therefore when $(U_1 - U_2) \to 0$ and ρ = const the solution is given by the error function

$$f(\eta) = \frac{2}{\sqrt{\pi}} \int_0^{\eta} e^{-x^2} dx$$

To solve our problem for $\alpha = 0$ we try an iterative procedure; first, we introduce $f(\eta) = \text{erf}(\eta)$ into (3.2.1); second, with the calculated profile $\rho(\eta)$ we go to (3.2.2) and compute $f'(\eta)$ which is integrated and back again to the same loop till convergence is achieved.

As an illustration of the solutions, the case $\rho_2 U_2^2 = \rho_1 U_1^2$ for different values of the turbulent Schmidt number is shown in figure 2.

3.3 Pressure Gradient Case: $\alpha \neq 0$

In our first attempt to solve this problem we made the assumption that the velocity profile would never exceed its free stream value in a similar iteration procedure to the one already followed in section 3.2. This supposition proved to be false, as shown in Appendix A. For the case $-1 < \alpha < 0$, and $Sc_t < 1$, the velocity will approach asymptotically its low speed side from below, and that of high speed from above.

With this knowledge of the asymptotic behavior a different procedure was adopted, wherein no restrictions were imposed upon the iterative procedure.

From equations (3.1.3) and (3.1.5), eliminating $A' + u(1 + \alpha)$,

we have

$$\frac{X'}{X} = \frac{Sc_t}{\gamma} A$$

But $A(\eta) = -\frac{(1+\alpha)}{\rho} \int_{\eta_o=0}^{\eta} \rho u \, dx$

Integrating twice and using the boundary conditions to find the constants, this expression yields

$$\rho(\eta) = e^{\ell n \left(\frac{\rho_2}{\rho_1}\right) \frac{\int_{\eta}^{\infty} e^{-B(x)} dx}{\int_{-\infty}^{\infty} e^{-B(x)} dx}} \qquad (3.3.1)$$

where, as before

$$\frac{C_\mu}{\beta} \left(\frac{U_1 - U_2}{U_1 + U_2}\right) = \frac{1}{2}$$

and

$$B(x) = Sc_t \int_0^x \left\{ \frac{(1+\alpha)}{\rho(\zeta)} \int_0^{\zeta} \rho \left(1 + \frac{U_1 - U_2}{U_1 + U_2} f\right) dy \right\} d\zeta$$

The momentum equation can be put in the form

$$Y' - \frac{A}{\gamma} Y = \frac{\alpha}{\gamma} (\rho u^2 - 1)$$

and multiplying left and right hand sides by

$$e^{-\frac{1}{\gamma} \int_{\eta_o}^{\eta} A(x) \, dx}$$

we get

$$\frac{d}{d\eta}\left[Y\, e^{-\frac{1}{\gamma}\int_{\eta_b=0}^{\eta} A(x)\,dx}\right] = \frac{\alpha}{\gamma}(\rho u^2 - 1)\, e^{-\frac{1}{\gamma}\int_{\eta_o=0}^{\eta} A(x)\,dx}$$

We can now integrate to arrive at

$$f'(\eta) = D(\eta)\left\{\rho(0)\, f'(0) + \frac{\alpha}{\gamma\left(\frac{\Delta U}{2U_1}\right)} F(\eta)\right\} \qquad (3.3.2)$$

where

$$D(\eta) = \frac{e^{-\frac{B(\eta)}{Sc_t}}}{\rho(\eta)}$$

and

$$F(\eta) = \int_{\eta_b}^{\eta} (\rho u^2 - 1)\, e^{\frac{B(x)}{Sc_t}}\, dx$$

We start our iterative procedure introducing $\rho(\eta)$ and $f(\eta)$ from the $\alpha = 0$ solution into (3.3.1). Getting a new $f'(\eta)$ from equation (3.3.2) and integrating we will have first iteration profiles for $\rho(\eta)$ and $f(\eta)$ which, substituted back into the expressions for $\rho(\eta)$ and $f'(\eta)$ will give us a second approximation, and so on till convergence is accomplished.

As the technique for $\alpha \neq 0$ is different from the one we used before, a comparison was made with those results by setting $\alpha = 0$ in our expressions for $\rho(\eta)$ and $f'(\eta)$; the solution was the same as the one we had obtained earlier for the case $\rho_1 U_1^2 = \rho_2 U_2^2$.

Taking into account the work of other investigators, e.g., Brown and Roshko (Ref. 1), Way and Libby (Ref. 24), we deduced that a very plausible turbulent Schmidt number for our experiments was going to be about 0.30. Having this in mind we kept constant Sc_t and compared our numerical solutions for different values of α. From these comparisons it can be clearly seen that the effect of an adverse pressure gradient ($\alpha < 0$) is far more pronounced than that of a favorable one ($\alpha > 0$).

Based upon this finding we decided to concentrate our experiments on the adverse pressure gradient.

Figure 3 shows a comparison for the u and ρu^2 profiles across the layer.

IV. EXPERIMENTAL FACILITY, INSTRUMENTATION, AND EQUIPMENT

4.1 Flow Apparatus

The experiments were performed in the high-pressure flow facility (Ref. 1) designed to produce a turbulent shear flow between two streams of different gases.

Basically it consists of two supply lines each one coming from eight 2000 psi bottles; the gas streams are brought together at the exit of two 4" x 1" nozzles in the test section; a schematic representation is shown in figure 4. The test section is enclosed by a cylinder which slides over and seals against O-rings placed on circular plates at both ends of the section, and the whole tank can then be pressurized up to 10 atmospheres. The upstream and downstream regulators and valves which control the flow rates and pressures in the tank have very fast time response characteristics. Operating the system at 7 atm, steady flow in the test section is established in about 150 milliseconds with velocities up to 50 ft/sec. Normal running times vary from 1 to 3 seconds. The turbulence level is less than 0.5%. Reynolds number at 10 atmospheres can be as high as 10^5/cm. Adjustable side walls which span the test section are used to adjust or remove pressure gradients in the flow.

A traversing gear, which incorporates a stepping motor, moves the probe in steps of .001" at the command of an input voltage pulse train, hence by counting pulses the position of the probe can be determined within .001" at any instant of time.

The thickness of the splitter plate, which separates the two streams till they meet at the nozzles exit, is approximately . 002" at its downstream end.

Some modifications were made in the test section in order to impose an adverse pressure gradient on the mixing layer. The 4" x 1" nozzles were replaced by 4" x $\frac{1}{2}$", so that the transition region needed in adjusting the flow to the desired free stream conditions would be shortened. The side walls of the working section, used for the zero pressure gradient case,had been a solid wall for the high velocity side and a 10% slotted wall for the other side. To set the adverse pressure gradient (cf. Fekete, Ref. 8), we changed these walls for ones with adjustable slats and installed a perforated plate at the downstream exit of the channel (Fig. 5).

4.2 Instrumentation

Because of the very short duration of the flow and the intrinsic difficulties of unknown composition, high turbulence levels and frequencies, very sophisticated and fast data acquisition systems were used for the collection of the data; this equipment, described in section 4. 3, handled the information coming from three different types of probes: an array of static pressure tubes, a pitot tube, and an aspirating probe.

4.2a Static and Pitot Tubes

The array of static ports consists of six static pressure tubes of different lengths mounted on a slanted holder (Fig. 6.) Taking

the sensor holes of the longest tube as reference, each of the successive ones is 1" lower so that, by placing the array in the free stream of our two-dimensional turbulent shear layer oriented in the spanwise direction, the static pressure, or $U_1(x)$ and $U_2(x)$, can be measured at every inch down to 5" from the splitter plate.

This probe was used in the preliminary measurements made to set up the desired external flow field; during these measurements one of the inputs of the pressure transducer was directly connected to the reference tube; the other five static pressure tubes were joined by means of plastic tubing to the entries of a fast pressure scanner (Scanivalve), a device that sequentially communicates each one of the static ports to the collector, which in turn goes to the other input of the pressure transducer.

The pitot tube, in connection with a Datametrics electronic manometer and Barocel differential pressure sensor, was used to obtain dynamic pressure profiles across the mixing layer, and to take the final measurements in order to establish an adverse pressure gradient.

4.2b Aspirating Probe

Due to the necessity of knowing the local composition in our plane turbulent mixing layer, a novel probe was developed for this study by Brown and Rebollo (Ref. 10). A complete account of the way it works is given in Appendix B.

Several modifications were made on this probe till a final version was achieved. Major difficulties of the design shown in

figure 1 of Appendix B were first, the replacement of the wire whenever it broke; second, too large length/diameter ratios when using smaller wires; in addition, some minor problems were related to the warming up of the glass. Based upon these considerations our final design was that of a normal hot wire inside a hollow holder. The hot wire is enclosed by a long tipped glass hood which slides over and is sealed with epoxy against the outside surface of the holder (Fig. 7). To avoid flow instabilities inside the probe a very gradual area expansion was chosen for the glass cover, and in order to have faster time response* a smaller wire diameter (. 0002") was used.

4.3 Description of the Experimental Equipment

The equipment used during the experiments could be divided into different categories according to its function. Some components of the apparatus receive a physical signal from the measuring probes and convert it into an analog voltage; e. g. , electronic manometer (Barocel), constant temperature anemometer (Thermo-Systems); that voltage is digitized by means of an A/D converter, and it is delivered to an output unit; e. g. , incremental or synchronous tape recorder. A very important function is that of regulating the flow of data; this task is performed by the control equipment; e. g. , Scanivalve and controller, electronic pulsing circuit and coupler for the incremental tape recorder, coupler (Data Slicer) for the synchronous tape recorder.

---

* Section 8 of Appendix B indicates how the time response of the probe is evaluated.

4.3a Electronic Manometer and Constant Temperature Anemometer

The basic system is made up of the Barocel pressure differential sensor and the Type 1014A Datametrics electronic manometer. The Type 1014A provides the electrical excitation for the pressure sensor and in turn accepts the pressure generated signals for voltage conversion.

The Barocel was used to measure the static pressure from the array of tubes at several downstream locations in the free stream when establishing the pressure gradient, and to measure the dynamic pressure across the layer when traversing the pitot tube.

The aspirating probe was used in connection with a high frequency and low noise constant temperature anemometer Model 1050 (Thermo-Systems) which provided the usual feedback bridge.

4.3b A/D Converter and Control Equipment

The A/D converter (Raytheon Model ADC Multiverter) is capable of operating at 33,000 conversions per second while multiplexing up to 16 channels of analog data. The analog input via BNC connectors is bipolar, ± 10 v, into 10^8 ohms. The resolution is 11 bits and sign; i.e., 2048 counts on either side of zero. The output is binary integer, positive-time logic.

The Scanivalve is a scanning type pressure sampling valve for switching multiple pressure points. The pressure transducer is sequentially connected to the various P_x ports via a radial hole in the rotor which terminates at the collector hole. As the rotor rotates, this collector hole passes under the P_x ports in the stator. Our

Scanivalve has a wafer switch with 24 entries plus collector, and it is driven by a Ledex solenoid.

The solenoid controller regulates the stepping speed of our Ledex solenoid driven Scanivalve. It will drive the solenoid motor at any rate up to 20 steps per second. The command to advance the Scanivalve one step can be given remotely, by an external switch closure of 5 milliseconds minimum, or through a manual or local command push button.

In order to control the flow of data coming from the Barocel, which is going to be written on tape by means of an incremental tape recorder, a pulsing circuit, and an 8 bit-1 byte coupler between the Raytheon Multiverter and the Kennedy incremental recorder were used.

The electronic pulsing circuit provided the necessary pulses to step the stepping motor, so that it would traverse the pitot probe at any rate up to 500 pulses/second ($\frac{1}{2}$ inch/second), or 1000 pulses/second when slewing up the frequency of the pulses; these pulses were also used as a clock for the operation of writing the data. The electronic coupler synchronizes the traversing mechanism with the Raytheon Multiverter and the digital incremental tape recorder.

As we have already mentioned, the data signals from the constant temperature anemometer were handled by a very fast data acquisition systems designed by Coles. The coupler (Data Slicer) controls the operation of the Raytheon Multiverter writing on a Kennedy Model 3110-05 synchronous digital tape recorder; it also commands the stepping pulses to traverse the aspirating probe across

the shear layer.

The coupler controls provide a limited choice of data word length, record length, and file length. A short record containing a two-digit file-identification number may be written if desired.

4.3c Magnetic Tape Recorders

All data signals were written on a 9 track 800 BPI magnetic tape using two types of recorders. The Kennedy Model 1600/360 digital incremental recorded all pressure measurements. Data can be commanded to be written, by the coupler, at any rate up to 500 bytes per second, or 1000 bytes/second if we slew up the frequency of the write pulses coming from the pulsing clock.

The Kennedy Model 3110-05 synchronous digital tape recorder writes 9 track at a fixed tape speed of $37\frac{1}{2}$ inches per second; it was used to record all density measurements. The IBM compatible writing mode is 800 bytes per inch. The fixed data rate is therefore, 30,000 bytes per second.

V. EXPERIMENTAL PROCEDURES

5.1 Facility Tests

A large number of tests were performed to know and, whenever was possible, to improve the flow quality of the test section as well as some of the characteristics of the instruments we were going to use.

During the experiments carried out in reference 1 the turbulence level in the free stream was thoroughly measured and reduced from about 1% to 0.3% using honeycombs and screens. Absorbing material to damp the acoustic level was used in the supply section of the system. Side wall positions to remove pressure gradients were investigated for different velocity ratios.

To provide a reference experiment for the experiments with two gases, Brown and Roshko made measurements in the shear layer between two streams of nitrogen traversing a pitot tube and a hot wire side by side ($\frac{1}{2}$" apart). Since accurate experimental measurements for homogeneous flows had been made previously by Liepmann and Laufer (Ref. 25), Spencer and Jones (Ref. 26), Miles and Shih (Ref. 27), and others, sufficient comparative information existed to verify the validity of the experimental data processing procedures. No significant differences were found between the results of Brown's and Roshko's homogeneous experiments and those of other investigators.

Further tests of the facility have been undertaken during the present investigation and we shall describe some of them.

Figure 8 shows an oscilloscope photo of the response of a

hot wire (upper trace) and a pitot tube (lower trace), placed side by side, to the process of starting the flow in the test section. The horizontal scale is 100 milliseconds/cm, vertical scale is 1 volt/cm. The time needed to establish steady flow is about 150 milliseconds for a tank pressure of 7 atm. and velocities of 30 ft/sec.

When measuring the static pressure in the free streams (Sec. 5.2) a very important question arises: how long should we keep the Scanivalve connecting a certain pressure static tube with the pressure transducer? A minimum value is set by the time response of the line once the step command has been given to the Scanivalve, a maximum time is limited by the duration of the flow.

To measure the time response of the line, the total head probe was connected to, say, entry No. 2 of the fluid wafer switch; the collector joined to one of the inputs of the pressure sensor, and the other input was directly communicated to the static probe; the rotor of the pressure scanner was facing entry No. 1 at this time. With the flow on, the Scanivalve was commanded to step to entry No. 2, thus putting in communication the pitot tube signal with the pressure sensor via the wafer's collector. Figure 9 shows an oscilloscope photo of the output of the electronic manometer. The oscilloscope was triggered with the leading edge of the step command pulse (horizontal scale = 20 ms/cm, vertical scale = .5 volt/cm); the first 25 to 30 milliseconds agree with the manufacturer's claim of 30 ms duration for the step command pulse, needed for the solenoid drive to move the rotor to the next port. It is clear from figure 9 that the

time response of the line going through the Scanivalve is approximately 100 milliseconds when using a plastic tubing of 2/16" in diameter.

Although the two-dimensionality of the flow had already been shown in reference 1, several tests were made to confirm it.

Two platinum hot wires .0002" in diameter, and almost the same cold resistance, were separated 2" apart and operated at the same overheat ratio. The two wires were placed approximately in the middle of the mixing layer, and aligned in the spanwise direction. The outputs from a two channel constant temperature anemometer are shown, for several downstream locations, in the oscilloscope pictures of figure 10. The photographs reveal a high degree of correlation between the two signals, as would be expected from a two-dimensional flow. The experiments were performed at a tank pressure of 3 atm., but it should be noted that the same tests done by Brown and Roshko at 7 atm. correlated equally well the outputs of the two platinum hot wires.

5.2 Procedure to Set Up the Equilibrium Flow

Preliminary measurements to set up the desired potential flow were made with the array of static pressure probes; a schematic representation of the way this was done is shown in figure 11; the required timing of the operation is presented in figure 12. Five records were written for every run, i.e., one record for each static pressure tube; the interval of time between record gaps was 470 milliseconds during which 200 data signals were taken, but out of this 200 only the last 150 data signals were accepted due to the fact that the

rest was affected by the time response of the pressure instrumentation (Sec. 5.1).

The following procedure was followed to set up the adverse pressure gradient on the mixing layer. First, the velocities of the two streams (N_2 and He) were set such that the dynamic pressures of both gases were the same at the exit of the nozzles. The adjustable slats of the working section were pre-set with a uniform separation of 1/32", to give an adverse pressure gradient. The free stream static pressures of the nitrogen and the helium flows were measured at several streamwise stations with the static probe array aligned spanwise in the flow. Once the static pressure distributions in the downstream direction were known for both potential flows, the orientation of the array was reversed, by rotation of 180^{o} around the vertical axis of the slanted holder, and the above mentioned measurements were repeated again in order to see whether non-two-dimensional effects could be present; no difference was found in the distributions of static pressure by orienting the array either way. Using Bernouilli's equation the free stream velocities were then calculated, and the condition of equality of total heads at those downstream locations checked. The slat spacing was re-set a few times by trial and error till the condition $\rho_1 U_1^2 = \rho_2 U_2^2$ was satisfied; direct measurements of the velocities were then made using a pitot tube and static pressure probe. Photographs were taken to look for linear spreading and to try to locate the virtual origin x_o*. With an estimate of x_o, (U_1/U_{10})**

---

* A more accurate location of the virtual origin is determined in section VIII.

** U_{10} is the value of U_1 at the nozzle exit.

was plotted against $(x - x_o)$ on log-log paper, so that from the slope an approximate value of α could be found.

The above mentioned procedure was repeated several times for different perforated plates until a value of α between -0.17 to -0.20 was achieved. According to our numerical calculations this value of α was adequate to show significant differences from the free mixing layer at $\alpha = 0$. An indication of that was provided by comparing instantaneous shadowgraphs of the two cases as shown in figure 13; a faster spreading rate and a squeezing of the large structure can be noticed in the shear layer under adverse pressure gradient. To get that value of α an exit obstruction, a perforated plate of 31% open area, was used; the slat separation in the helium side decreased continuously from about 2/32" at 3/4" downstream of the splitter plate, to approximately 1/32" at the middle of the working section, until it finally reached 1/64" at the end of it. In the nitrogen side from 3/64" we went down to a separation of the order of 1/32" at 5" and from this it reduced to a gap of approximately 1.5/64".

5.3 Selection of Flow and Traversing Procedure

In contrast to the experimental procedure used by Brown and Roshko of traversing density, pitot and static probes at the same time, we decided to traverse them separately for several reasons; first, due to the differences in time response of the two probes we wanted to traverse the pitot tube very slowly in order to spend a maximum of time at every location, so that its slow response could be compensated, and hence a very reliable profile of dynamic pressure across the layer

could be obtained. On the other hand, if we wished good statistics for the density measurements, two things were desirable: for one, using the incremental digital tape recorder we were limited to 1 kHz (when slewing up the frequency and traversing only the aspirating probe), for another, we wanted to take composition measurements at several "points" in the mixing region; i. e., the aspirating probe standing still at those points while taking the data, that could not easily be done with the present pulsing circuit. Since we had the intention of measuring rms density fluctuations, we concluded that the aspirating probe would have to be traversed in a new and more sophisticated way. In addition, a faster method of collecting the data was also needed, the answer as explained in section 5. 5 was Coles' coupler, the "Data Slicer".

As indicated earlier an ideal aspirating probe should give us first, large change in voltage when used from pure helium to pure nitrogen; second, fast time response; third, stability of the flow inside the probe when the sonic throat Reynolds number varies appreciably.

Unfortunately, as with any real probe it is impossible to satisfy these ideal properties without a limit; this limit will depend among other factors: on the probe construction, on the gases we are dealing with, i. e., nitrogen and helium, and on the external conditions, i. e., tank pressure. In our case the best characteristics were found to be at 4 atm; the change of voltage was about 350 millivolts; probe rise time between 5 and 10 kHz and noise to signal ratio of the order of 1%. At higher pressures the noise to signal ratio increased very

slowly, till at 7 atm it was about 6% due to the fact that the probe started to become unstable when exposed to pure nitrogen.

With this knowledge we decided to carry out our experiments at a tank pressure of 4 atm, though they were repeated at 2 and 7 atm to see the influence of the Reynolds number on the properties of the mixing layer.

The shear layer with no pressure gradient was also measured at 4 atm, so that comparisons could be drawn as to what effect the pressure gradient would have on the mixing region; e. g., would it affect the turbulent transport of momentum the same way as the transport of turbulent mass diffusion?

Table I presents a summary of the flow conditions for all the experiments.

5.4 Dynamic Pressure Traverse

The data were recorded in a very similar way to that used for static pressure measurements (Fig. 11); the only differences were a) that the line carrying the signal to step the solenoid drive disappeared since we no longer needed the Scanivalve; consequently the total and static tubes went directly to the entries P_1 and P_2 in the pressure sensor; b) a new line connected the output of the pulse shaper to the inputs of the stepping motor.

The required timing of the operation, as shown in figure 12, was the same as before, except that in step 7 the shaped pulse was directed to the Beckman Counter and stepping motor, and step 9 was unnecessary as already explained in a).

Two records were taken at any given station, one when traversing the probe from the nitrogen side towards the helium side, the other when going in the opposite direction. The traverse rate of the probe which is directly proportional to the trigger frequency (N pulses/second), was constant for any downstream location, but changed from station to station depending on the thickness of the mixing layer; i.e., the thinner the shear layer, the slower the crossing rate; e.g., N could be 1000 pulses/second at x = 3/4", and N = 3000 pulses/second at x = 3.25".

The number n of pulses needed to traverse the mixing region at any station, which is also the number of data signals to be written on each of the two records for that location, was set (Beckman Counter reset) according to the thickness of the mixing layer at that station; e.g., n = 500 pulses at x = 3/4", n = 1200 pulses at x = 3.25".

Fourteen traverses at seven downstream locations were made for the case $\alpha < 0$ and tank pressure of 4 atm, 12 and 8 traverses at 6 and 4 stations respectively were investigated for the other tank pressures of 7 and 2 atm.

The last station measured was at x = 3.25" for $\alpha < 0$, since from there down the effect of the walls interacting with the mixing layer began to be felt.

From the photographic study (Sec. VI), we found where to start the traversing and where to finish it. Once these two points were fixed we had a very good estimate of the number n of pulses needed to cross the shear region; this procedure saved taking unnecessary data, and consequently it shortened the required duration of the flow.

5.5 Density Traverse

Composition profiles of the binary mixture were evaluated at 4 downstream locations for all the experiments.

As we have mentioned earlier, the Data Slicer was used with a threefold purpose: traversing of the probe, command of the A/D conversion and control of the writing of the digital data onto tape.

The traverse was done in such a way that the aspirating probe was half-time stepping and half-time stopped. Although data collection proceeded during all the time, only the one taken while the probe was not moving was used for later processing in the computer. Since the fixed data rate of the synchronous digital tape recorder is 30,000 bytes/second, and we used 1 byte/word for all the experiments, our recording speed was 30 kHz for all density measurements.

Table II shows a summary of the possible traverses which could be made by using the Data Slicer when the recording time is limited to 4.368 seconds, or what is equivalent, the total distance traveled by the probe is fixed at 1.024 inches. These were the limits generally used in our experiments, since a longer duration of the flow could introduce temperature effects into the problem due to the cooling of the expanded gases. Nevertheless longer distances were needed at the most downstream stations to cover the wider mixing region; e.g., 9 records instead of 8, for a total distance of 1.152 inches, and 4.914 seconds of running time when using 8,192 samples per data point. For these the following procedure was used. A clock of 30,000 pulses/second, provided by the coupler, was divided by 64 and the resulting pulses were used as step pulses; during the second half

of the record period the train of pulses was inhibited and the probe remained stopped at that position till the beginning of the next record.

Out of all the possibilities described in table II the one with 8,192 samples per data point was chosen. A large number of samples were desired in order to have good statistics, and 8 or 9 points across the mixing layer were considered as sufficient to describe a mean density profile. A larger number (16,384) of samples per data point was available, but then only 4 or 5 points across the layer would have been too few to describe an adequate average profile; possibly a better mean density could have been achieved with the 4,096 samples/data point mode because then at least 16 data points, or probe steps, were possible, but the smaller number of samples would have resulted in a less accurate measurement of the rms density fluctuations at each point.

Resuming, therefore, at any x station, 8 or 9 data points were measured, 8 or 9 records of .546 seconds were written, and the probe traveled a distance of .128" per record. 16,384 samples were taken per record, but only the second half, 8,192, were used and processed as data samples per record. The duration of the record gap or gap time was 21.3 milliseconds.

The photographs were a very useful tool in fixing beforehand the end points of the traversing and, consequently, in deciding whether to take 7, 8 or 9 records per run.

VI. PHOTOGRAPHIC INVESTIGATION

6.1 Flow Structure

Spark shadowgraphs were used to evaluate the flow qualitatively and to plan the experiments. A spark source was placed at the focal point of a parabolic mirror to produce a parallel light beam. The light was directed through a tank window across the flow field and onto a sheet of film placed inside the pressure vessel against the glass end-wall of the working section. The spark light duration was a few microseconds, therefore the photos can be considered as instantaneous shots of the flow structure (Fig. 13). The reality of this large structure as being an essential feature of the plane turbulent shear layer was confirmed by many experiments performed by Brown and Roshko (Ref. 1); more important, it is not produced by the density difference, as they proved it by taking shadowgraphs of a shear layer between two streams having essentially the same density (air and nitrogen).

The large structures do most of the turbulent transport of momentum and mass diffusion, since as we can imagine, it convects gas from one side of the layer to the other.

It can be seen from the photographs that these large eddies are as big as the width of the flow, which is the relevant length scale in the analysis of the interaction of the turbulence with the mean flow. One would then expect that two flows having dissimilar large structures, as in our case, with $\alpha < 0$ and $\alpha = 0$, must reflect that fact by affecting in a different way the turbulent transport terms in each case. Since

these turbulent terms are intimately related to the mean profiles, the ultimate effects of structure differences ought to appear in the profiles of the mean motion*.

That the "big eddies" are two-dimensional rather than three-dimensional is strongly suggested by the high correlation of the spikes in figure 10.

6.2 Flow Structure at Different Reynolds Numbers: Zero and Adverse Pressure Gradients

As is well known, the main difference between two turbulent flows with different Reynolds number, but with the same integral scale, is in the smallest eddies: a turbulent flow at a relatively low Reynolds number has a relatively "coarse" small scale structure. The variation of the Reynolds number can be achieved by either changing the tank pressure, or the velocity of the gas streams. As the Reynolds number of the flow as a whole increases, e.g., raising the pressure of the tank from 2 up to 7 atm, large eddies appear first (at 2 atm only a large structure is visible); the smaller the eddies, the later they appear (at 8 atm a fine scale motion is clearly observable). Figures 14 and 15 show shadowgraphs of the mixing layer for the two cases $\alpha = 0$ and $\alpha < 0$, at different Reynolds numbers.

At the lowest Reynolds number only the large structure appears. These large eddies have the largest amplitudes. The velocity and density in them are comparable with the variation of mean

---

* See section VIII for a comparison of the mean profiles for $\alpha < 0$ and $\alpha = 0$. See also section 9.2.

velocity and density over the distance δ (Ref. 28); a verification of this assertion can be found in the density traverse across the turbulent flow (Sec. VIII).

The period with which this flow pattern is repeated when observed in some fixed frame of reference is of the order of δ/U where U is the mean flow velocity.

Regarding our two-dimensional test photos (Fig. 10), U is of the order of 500 cm/sec, and δ changes from about .3" to approximately 1" in the most downstream station; therefore the order of magnitude of the time scale T of the large eddies could vary from about 2 to 10 milliseconds which agrees well with the periodicity of the spikes in figure 10.

As the Reynolds number increases, smaller eddies appear which correspond to larger frequencies, and at the highest Re number a fine, high frequency, detailed structure is superposed on the big turbulent eddies.

This wavy structure, as pointed out by Brown and Roshko, is reminiscent of the late stages of instability waves in laminar free shear layers (Ref. 29). Although in this case it is clear from the photographs that the scale of the instability structure increases downstream, probably linearly in the mean like the thickness of the layer.

It seems plausible that through a highly intermittent, up and down wabbling process these waves continuously adjust themselves so that in the average, as similarity would require, their wave length grows linearly with x.

Among other features that can be seen in the shadowgraphs we would like to indicate: the differences in the large structures presented by the zero and adverse pressure gradient cases* which should have a bearing on the turbulent transport terms as we have discussed earlier, and the contrast between the two interfaces, sharper and better defined in the nitrogen side.

6.3 Spreading Rates

Multiple exposure shadowgraphs were taken, using neutral density filters to reduce the light per exposure; from such a superposition of instantaneous photos, an average picture of the flow could be obtained. Figure 16 shows multiple exposure shadowgraphs of the mixing layer at different Reynolds numbers for the adverse pressure gradient case.

In the shadowgraphs at low Reynolds number a double regime is more clearly distinguishable than in the other; in the most upstream portion of the layer there exists a transition flow into the adverse pressure gradient region where the spreading rate of the layer grows much faster; this transition region and in consequence the virtual origin moves upstream towards the splitter plate as the Reynolds number increases.

When the virtual origins for the flows at different Reynolds numbers are known (Sec. VIII), e. g. , from the dynamic pressure or density traverse (one estimate can be obtained from the photographs

---

* A possible explanation of this difference is given in section IX. (section 9. 2).

themselves) we will be able to get one measure of the spreading rates for the zero and adverse pressure gradients from the shadowgraphs. The spreading rate is defined as

$$\text{spreading rate} = \frac{\text{width of the layer}}{(x - x_o)}$$

where the width of the layer, at any x, is the distance between two points on two straight lines traced tangentially to the outer edges of the mixing layer and passing through the virtual origin (see illustration below).

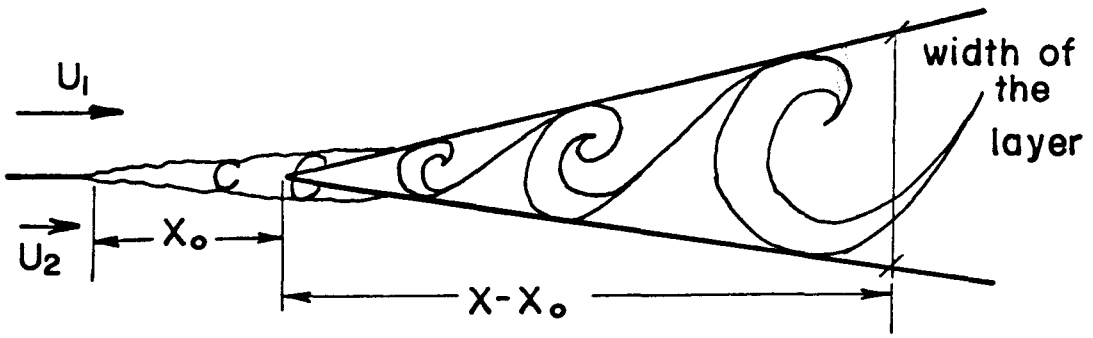

A total of 85 photos were taken for both cases and the margin of error around the average spreading rate was never higher than ± 5%. The average spreading rate for the $\alpha = 0$ case and $\rho_1 U_1^2 = \rho_2 U_2^2$ was about 0.24. The average spreading rate of the $\alpha < 0$ case was of the order of 0.39. Consequently the mixing layer under an adverse pressure gradient of $\alpha = -0.18$ (Sec. VIII) spreads approximately 60% faster. Finally we should mention that these pictures were of great help in planning the total head and density traverses across the shear region.

VII. DATA PROCESSING

7.1 Pressure Measurements

The recorded signals from the array of static pressure tubes, five records per run and 200 data signals per record, were read record by record. An arithmetic mean value of the last 150 readings of every record was obtained. This mean value gave us the average static pressure difference between the static probe corresponding to that record, located x inches downstream of the splitter plate, and the reference static tube, located at the exit of the nozzles (x = 0 inches).

The digitized data recorded during the dynamic pressure traverses for $\alpha < 0$ were read record by record and checked for obvious errors; e.g., skipped record, short record, etc.

The data of every traverse were normalized with the free stream dynamic pressure reading corresponding to that traverse; these normalized valueswere then plotted against the distance traveled across the shear layer. From these plots it was very easy to check whether the condition $\rho_1 U_1^2 = \rho_2 U_2^2$ was satisfied or not for all the runs; out of 34 traverses only two were repeated because $\rho_1 U_1^2 \neq \rho_2 U_2^2$. It should be mentioned that the helium and nitrogen velocities at the exit of the nozzles changed slightly after a few runs due to a pressure drop in the supply lines; in order to minimize the error that this variation could introduce in the final data, the velocities of the two gas streams were re-set and re-adjusted, after every 2 or 3 runs, to maintain their original values.

To get a profile of mean dynamic pressure ($\rho U^2 / \rho_1 U_1^2$) from the normalized data we proceeded in the following way. Two records were taken for each downstream location (record one while moving from N_2 to He, record two going in the opposite direction). We reversed record two when reading the tape and a profile resulting from the arithmetic mean of these two records was obtained. A new smoothed profile was now produced from this one by replacing, at every 10th data point, whatever value of the dynamic pressure we had, for the local time-space mean dynamic pressure obtained by averaging over 10 data signals from each side. If the primitive profile had n data points the smoothed one would have only $(\frac{n}{10} + 1)$. An illustration of the smoothing procedure is presented below.

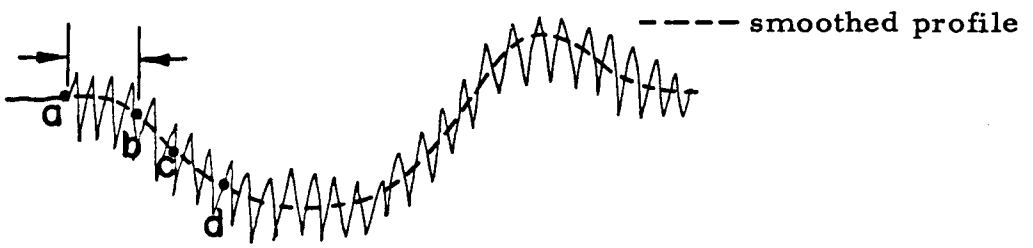

$$\text{Value of } \left(\frac{\rho U^2}{\rho_1 U_1^2}\right)_b = \frac{\sum_{i=1}^{10} \text{Values } \left(\frac{\rho u^2}{\rho_1 U_1^2}\right)_i \text{from ab} + \sum_{i=1}^{10} \text{Values} \left(\frac{\rho u^2}{\rho_1 U_1^2}\right)_i \text{from bc}}{20}$$

$$\text{Value of } \left(\frac{\rho U^2}{\rho_1 U_1^2}\right)_c = \frac{\sum_{i=1}^{10} \text{Values } \left(\frac{\rho u^2}{\rho_1 U_1^2}\right)_i \text{from bc} + \sum_{i=1}^{10} \text{Values } \left(\frac{\rho u^2}{\rho_1 U_1^2}\right)_i \text{from cd}}{20}$$

. . .
. . .
. . .
. . .
. etc . .

We should note that when smoothing the pitot tube readings we

do not actually get $\rho U^2/\rho_1 U_1^2$ but some other extra terms as well, $\overline{\rho' u'}$, $\overline{\rho' u'^2}$, etc. . . ; in neglecting these terms an error of less than 5% is introduced (see Appendix C).

Ten data point signals or .01" distance between the points of the averaged profile was considered to be an acceptable separation since the opening of the total head pressure tube in the transverse direction was about 1/64" wide, and one would expect that the pitot tube was already making some kind of smoothing over that distance.

A completely similar procedure was followed for the $\alpha = 0$ case.

All the data processing was carried out using an IBM 370/155 computer.

7.2 Density Measurements

As previously indicated, the Data Slicer formatted the information onto the tape in the following way.

$$\frac{\text{Bytes}}{\text{Word}} = 1 \; ; \quad \frac{\text{Words}}{\text{Record}} = 16,384 \; ; \quad \frac{\text{Records}}{\text{File}} = \begin{matrix} 08 \\ \text{or} \\ 09 \end{matrix}$$

The first half of the samples, contained in every record, were disregarded (aspirating probe was moving while taking these samples) and only the last 8,192 digital readings, taken while the probe was still, were processed as useful data.

The helium and nitrogen velocities at the exit of the nozzles were checked, re-set and re-adjusted after every two runs.

The digitized voltages from the constant temperature hot wire anemometer were converted to concentration measurements by using

the calibration curve of the new aspirating probe (Fig. 17).

The values from readings taken in the pure gases were used to determine the maximum voltage variations ($V_{max} - V_{min}$, V_{max} in pure helium, V_{min} in pure nitrogen)*. Other readings were then converted to a percentage of the maximum. This normalization permitted the use of a single calibration curve, for every tank pressure, when the voltages were transformed to concentration. Several calibrations showed that, although the absolute value of the voltages and the maximum variation changed slightly over a period of time, the scaled values would always yield the same concentration measurement, within the accuracy of the probe.

Once the measurements were density converted, a probability function of the density was computed at every data point. Therefore at any downstream station 8 or 9 density probability functions of 8,192 data samples each were generated.

From the probability distribution at any point, the average density and rms value of the density flucuations were calculated for that particular point.

---

* See Appendix B.

VIII. RESULTS

8.1 Adverse Pressure Gradient Experiment

As we have shown in section II, turbulent mixing between two streams of different gases in a pressure gradient can have equilibrium structure provided $\rho_1 U_1^2 = \rho_2 U_2^2$ and $\alpha = \frac{x}{U_1}\frac{dU_1}{dx} = \text{const.}$

The analysis of the dynamics of self-preservation involved only the equations of mean motion, and did not prove that self-preserving flow is possible. Experimental evidence is needed to verify the physical occurrence of equilibrium flow.

An equilibrium flow of the kind described above has been established experimentally in our turbulent mixing apparatus (Sec. V). To determine the similarity properties of the mixing layer we measured mean profiles of dynamic pressure and density as well as rms density fluctuations.

8.1a Dynamic Pressure Profiles

Measurements of the dynamic pressure were carried out at seven streamwise stations, and two traverses were made at every location. The maximum velocity was 1080 cm/sec, and the tank pressure was 4 atm; the Reynolds numbers per unit length were $3.6 \times 10^3 \text{cm}^{-1}$ for the helium stream, and $1.2 \times 10^4 \text{cm}^{-1}$ for the nitrogen stream. For each run a traverse of $1\frac{1}{4}$" (or less) produced 1250 measurements.

The digitized data from the total pressure probe were read from the tape and normalized with the free stream dynamic pressure.

The normalized profiles were then plotted against the distance in inches traveled across the mixing layer.

Seven of these traverse plots, at different downstream stations, are shown in figures 18 and 19.

Considering the maximum and minimum values of the dynamic pressure in these plots it can be seen that equilibrium flow has not yet been attained at x = 1.5", and possibly is not fully developed at 2" downstream of the splitter plate.

Following the procedure already explained in section VII, we obtained profiles of mean dynamic pressure at each streamwise location. A characteristic length in the transverse direction, δ_1, was defined as the distance between the maximum and the minimum in these smoothed profiles. The virtual origin for x was found by extrapolating a straight line through the thicknesses determined at each traverse (Fig. 20). The origin was found to be 0.75" downstream of the splitter plate edge.

With the virtual origin x_o known we found the value of $\alpha = -0.18$ from the slope of the straight line in figure 21. This figure is a log-log plot of the free-stream velocity decay in the streamwise direction ($\frac{U_1}{U_{10}}$ vs $x - x_o$)*; U_{10} is the helium velocity at the exit of the nozzle.

Figure 22 is a similarity plot from the smoothed pitot tube profiles. Traverses corresponding to x = 0.75", x = 1", and x = 1.5" have not been included, since it was obvious that an equilibrium flow

---

* (U_2/U_{20}) would naturally give the same value of α, since $\rho_2 U_2^2 = \rho_1 U_1^2$, U_{20} is the nitrogen velocity at the exit of the nozzle.

was not yet established at these stations. It can be seen that even at x = 2" the similarity properties are not yet fully established.

It should be noted that this is a better test than the velocity or density profiles to verify the similarity properties of the shear layer, because of the sensitivity of the dynamic pressure profile, especially its maximum and minimum, to different pressure gradients; constant values should indicate equilibrium flow (cf. Figs.18 and 19).

The total dimensionless width of the shear layer is approximately 0.40 which agrees very well with our findings from the shadowgraphs.

8.1b Density Profiles

Four density traverses were made from x = 2.25" to x = 3.25", after which the side wall begins to interfere with the mixing layer. The maximum velocity (helium side) was 1000 cm/sec, and the ambient tank pressure 4 atm.

Eight data points were recorded per traverse, and 8,192 samples were processed per data point. An example of a density traverse is shown in figure 23; four data points and their corresponding probability distributions have been plotted. The plots with 'continuous trace' represent the voltage from the constant temperature anemometer, after A/D conversion, as a function of time. This computer plot draws a continuous line between individual data points, so the latter are not clearly distinguishable.

These voltages were converted to concentration by means of the calibration curve, and a density probability function was generated

for each record.

It is clear from this figure that the voltages are neither smaller than V_{min} (nitrogen) nor bigger than V_{max} (helium), and that variations in voltage are of the same order of magnitude as the voltage difference between the two streams. This is consistent, as indicated by Brown and Roshko (Ref. 1), with the large structure evident in the shadowgraphs, which one imagines can convect gas from one side of the layer to the other.

From the probability distributions a mean density profile at each station was obtained, and a characteristic transverse length, δ_2, was defined as the distance between two points in this profile which corresponded to

$$\rho \text{ (point 1)} = \rho_1 + 0.90\,(\rho_2 - \rho_1)$$

$$\rho \text{ (point 2)} = \rho_1 + 0.10\,(\rho_2 - \rho_1)$$

In our case for helium and nitrogen

$$\frac{\rho}{\rho_1}\text{(point 1)} = 6.40$$

$$\frac{\rho}{\rho_1}\text{(point 2)} = 1.60$$

Figure 20 shows a plot of the variation of this length with the streamwise coordinate x. Clearly both mean profiles, dynamic pressure and density, define the same location for the virtual origin, x_o.

The resulting equilibrium profile for the mean density is shown in figure 24.

Profiles of rms density fluctuations, deduced from the probability distribution functions, also exhibit similarity (Fig. 25);

i.e., self-preservation. The maximum rms density fluctuation is approximately 20% of $(\rho_2 - \rho_1)$, and it occurs close to the nitrogen side of the mixing layer; in the helium side the fluctuations are less violent, but their high frequency content is higher than on the other side (Fig. 23).

8.1c Measurements at Different Reynolds Numbers

Measurements of dynamic pressure, density and rms density fluctuations at different streamwise positions were repeated for tank pressures of 2 and 7 atm. The virtual origins, found the same way as before, were 0.82" and 0.65" downstream of the dividing plate edge respectively.

Maximum velocities were about 1000 cm/sec for both experiments. An estimate of the buoyancy forces revealed that these were unimportant since the Froude number for these conditions was of the order of 100.

Figure 26 shows a log-log plot of the velocity decay for these two cases; the circles belong to the previous experiment (4 atm), and are shown for comparison. It can be seen that, even without re-setting the slats the value of α is the same as before; i.e., $\alpha = -0.18$.

Twelve dynamic pressure traverses at six stations were measured for the highest tank pressure, but only eight profiles and four positions were taken for the lowest one. Four downstream locations were investigated for all density measurements.

Figures 27 through 32 show the similarity profiles obtained from these experiments; the dashed lines represent the results obtained at 4 atm.

It can be observed that the mean profiles are virtually indistinguishable from the ones in figures 22 and 24. Some slight scatter is visible at both ends for the mean dynamic pressure at 2 atm (Fig. 30). On figure 27 only the four most downstream locations have been plotted; as before the equilibrium flow is not yet completely developed at x = 2".

With respect to the rms density fluctuations it is clear from figure 29 that the same self-preserving form of the profile, with all its pecularities, is obtained, although a deviation of 6 or 7% occurs in the middle of the mixing layer. This is accounted for partly by the different behavior of the aspirating probe at higher pressure, and partly because the probe begins to become unstable at 7 atm reducing the fluctuations whenever large concentrations of nitrogen are sampled*.

At the lowest Reynolds number (Fig. 32) the data points from the two nearest stations to the splitter plate edge deviate from the self-preserving profile close to the helium part of the layer. This indicates that the fluctuating density field has not yet reached a self-preserving form at x = 2.50" for this Reynolds number.

8.1d Calculation of Reynolds Stress and Turbulent Mass Diffusion

From the measurements of density and pitot pressure the velocity is obtained using the Bernouilli equation (Fig. 33). As predicted by the asymptotic behavior of the mixing layer**the undershoot on the low speed side is clearly observable; however the over-

---

* The reason for taking data at 7 atm was that we wanted to get a wide range in Reynolds number, and at the same time we considered that the probe behavior was adequate for comparison purposes with the data at 4 atm. See section V.

** See Appendix A.

shoot on the high speed side is negligible; both things are in agreement with the theoretical analysis. A comparison with the numerical solution of the eddy viscosity and eddy diffusivity model is presented in section IX.

We can now locate the dividing streamline in our experimental profiles by using the expression (2. 3. 8). Equation (2. 3. 11) was also used as a check on our calculations, and it gave the same position for η_o, that is, corresponding to a density ratio $\frac{\rho}{\rho_1} = 1.70$ and a dynamic pressure ratio $\rho U^2/\rho_1 U_1^2 \doteq 0.60$.

The distributions of shear stress and turbulent mass diffusion were then computed from equations (2. 3. 2) and (2. 3. 3) respectively; they are shown in figures 34 and 35. Note that the maximum shearing stress, about 0. 021, is not at the dividing streamline but displaced towards the right of η_o in agreement with the equation (2. 3. 4), since $\alpha(\rho u^2 - 1)_{\eta_o}$ is a positive quantity for $\alpha = - 0.18$.

Figure 35 shows $S(\rho)/\rho$ which has a maximum at η_o as expressed by the equation (2. 3. 5). With this curve, and making use of the measured mean density, the turbulent mass diffusion $\overline{\rho' v'}/\rho_1 U_1$ is calculated; this profile has its maximum shifted towards the nitrogen side which is where the rms density fluctuations are higher (Fig. 25).

Knowing these profiles, we can estimate the eddy viscosity and eddy diffusivity and consequently the turbulent Schmidt number for the flow.

From their definitions, we have

$$\nu_t = - \frac{\overline{\rho u'v'}}{\rho \frac{\partial U}{\partial y}}$$

$$\mathfrak{D}_t = - \frac{\overline{\rho' v'}}{(\frac{\partial \rho}{\partial y})}$$

and hence

$$\frac{\nu_t}{\Delta U(x - x_o)} = - \frac{U_1}{\Delta U} \frac{(\frac{\overline{\rho u'v'}}{\rho_1 U_1^2})}{(\frac{\rho}{\rho_1}) \frac{d(U/U_1)}{d\xi}} \qquad (8.1.1)$$

$$\frac{\mathfrak{D}_t}{\Delta U(x - x_o)} = - \frac{U_1}{\Delta U} \frac{(\frac{\overline{\rho' v'}}{\rho_1 U_1})}{\frac{d(\rho/\rho_1)}{d\xi}} \qquad (8.1.2)$$

$$Sc_t = \frac{\nu_t}{\mathfrak{D}_t}$$

Their distributions across the mixing layer are shown in figure 36. It should be taken into account that these computations are only reliable at the center of the mixing layer because of the difficulty of measuring slopes at the edges of the profiles, especially in the low speed side of the velocity distribution. The turbulent Schmidt number of this equilibrium flow is smaller than 1, very likely between 0.3 and 0.4, but increasing towards the outside of the shear layer. From the comparison of the numerical solutions and the experimental profiles (Sec. IX) we will have another estimate of the values of Sc_t and ν_t.

8.2 Zero Pressure Gradient Experiment

With the similarity properties of the mixing layer in an adverse pressure gradient known, we repeated the above experiments in a free shear layer with no pressure gradient in the streamwise direction*. Thus, by comparing the two flows we expected to draw some conclusions on the effects of an adverse pressure gradient upon a turbulent mixing layer between two different gases.

To perform this experiments the slats were replaced by a solid wall on the helium side and a slotted one on the nitrogen side, and their positions were adjusted in order to remove any pressure gradient from the test section.

The maximum velocity was about 1000cm/sec (Table I), and the experiment was performed at an ambient tank pressure of 4 atm. Four downstream stations were studied for the density and total head measurements, with two traverses per location for the dynamic pressure data.

8.2a Dynamic Pressure and Density Profiles

With the definition of characteristic lengths the same as for the adverse pressure gradient case, we found the virtual origin by extrapolating a straight line through the thicknesses determined at each station from the smoothed total head and density profiles. It was located 0.20" upstream of the splitter plate edge. Figure 37 shows the variation of this thickness with the streamwise coordinate

* Brown and Roshko results were not used for the reasons already stated in section 5.3.

x; the black dots were obtained from the total head traverses and the triangles from the averaged density data.

The similarity profiles for the mean quantities are plotted in figures 38 and 39. The data from location x = 1" have been left out in figure 38 because similarity has not yet been reached at that station. It should be noted that the total width of the layer, as indicated by these profiles, is approximately 0.25 which is in excellent agreement with our photographic study (see Sec. 6.3). According to this the mixing layer between helium and nitrogen spreads 60% faster for an adverse pressure gradient of $\alpha = -0.18$ than for $\alpha = 0$. A more pronounced and broad minimum in the dynamic pressure profile is clearly noticeable in the case with pressure gradient (Fig. 22).

The self-preserving form of the rms density fluctuations is shown in figure 40. The form of the profile does not seem to be affected by the adverse pressure gradient and, as before, the maximum fluctuations are approximately 20% of $(\rho_2 - \rho_1)$, occurring very near the nitrogen side of the shear layer.

8.2b Calculation of Turbulent Terms

From the ρu^2 and ρ profiles we deduced the velocity distribution across the mixing layer (Fig. 41). The dividing streamline was found from equation (2.3.8) after putting $\alpha = 0$; the same location of η_o was given by equation (2.3.11); its position corresponded to a density ratio ρ/ρ_1 of about 1.78 and a dynamic pressure ratio $\rho U^2/\rho_1 U_1^2$ of 0.87.

Replacing $\alpha = 0$ in equations (2.3.2) and (2.3.3) we can

compute the shear stress and turbulent mass diffusion (Figs. 42 and 43). τ_{max} is about 0.012, and it is located at the dividing streamline. Therefore, the adverse pressure gradient produced an increase of approximately 70% in the maximum shearing stress; while its effect on the turbulent mass diffusion was to make it only 20% higher.

Again the turbulent mass diffusion distribution has a maximum near the nitrogen side; where the rms density fluctuations are higher.

The turbulent Schmidt number was found to be very low, around 0.2, at the middle of the layer (Fig. 44).

A summary of the essential parameters for the two flows is presented in table III.

IX. DISCUSSION AND CONCLUSION

9.1 Comparison with Numerical Solutions

The numerical solutions of the equations obtained by using an eddy viscosity and eddy diffusivity model were plotted for several turbulent Schmidt numbers, and compared with the experimental results.

Figure 45 shows this comparison for the dynamic pressure profile through the mixing layer in an adverse pressure gradient of $\alpha = -0.18$. The best agreement occurs for a turbulent Schmidt number of about 0.30 and a value of $\beta \doteq 1/18.5$. The virtual kinematic viscosity becomes

$$\frac{\nu_t}{\Delta U\, x} \doteq 0.0033$$

as compared with 0.0040 for the experiment.

A similar comparison is shown in figure 46 for the zero pressure gradient case. The turbulent Schmidt number for the best fit is very close to 0.20. The resulting β is approximately $\beta \doteq 1/28.5$. The eddy viscosity becomes for this case

$$\frac{\nu_t}{\Delta U\, x} \doteq 0.0014$$

as compared with 0.0016 for the experiment.

The disagreement of the comparisons on the nitrogen side (low speed side) is probably due to our very simple approach of constant exchange coefficients.

Improved numerical solutions could be obtained by introducing

better assumptions into the modeling of the turbulent terms*; e. g. , taking intermittency into account as done by Wygnanski and Fiedler (Ref. 5) in their numerical solutions of jets and wakes in tailored pressure gradients.

As indicated above, turbulent Schmidt numbers are found to be very low, e. g. , 0. 2 for $\alpha = 0$ and 0. 3 for $\alpha = -0.18$; which agrees fairly well with our results in section VIII. This was somewhat surprising since most people use $Sc_t = 0.8$ or 1. 0 for their numerical solutions, which is not a good assumption at least for the plane, turbulent mixing layer between two gas streams of nitrogen and helium.

9. 2 Discussion of the Results

The results indicate that the adverse pressure gradient produces a faster spreading rate and a large increase in the eddy viscosity and turbulent shear stress, but the turbulent mass diffusion and eddy diffusivity only increase moderately.

Since a detailed account of the effect of density on the turbulent mixing layer is given in reference 1, we will discuss our results for the zero pressure gradient very briefly, and only as a background for the understanding of the role of an adverse pressure gradient on a turbulent mixing layer between two streams of different gases.

---

* References 11 through 22 mentioned at the beginning of section III make use of different turbulent models. See also other papers presented at the Langley Working Conference on Free Turbulent Shear Flows, July 1972.

9.2a Effect of Density on Spreading Rate and Eddy Viscosity

Comparing our experimental results for $\alpha = 0$ with those of other investigators for homogeneous flow, it can be seen that the effect of variable density, when the light gas (helium) is moving faster, is that of increasing slightly the spreading rate of the velocity profile.

From our experimental data for $\alpha = 0$ and $\frac{U_2}{U_1} = 0.378$, i.e., $\rho_1 U_1^2 = \rho_2 U_2^2$

$$h \simeq 0.105 \frac{\Delta U}{\overline{U}}$$

where

$$h = \frac{\left(\frac{\Delta U}{U_1}\right)}{\left(\frac{d(U/U_1)}{d(y/x-x_o)}\right)_{\text{maximum}}} \qquad (9.2.1)$$

and

$$\overline{U} = \frac{U_1 + U_2}{2}$$

From Spencer's (Ref. 26) velocity profile for $\frac{U_2}{U_1} = 0.3$

$$h \simeq 0.085 \frac{\Delta U}{\overline{U}}$$

A comparison of the eddy viscosity coefficients is presented in table IV below*.

TABLE IV

Comparison of eddy viscosity coefficients

	$\frac{\nu_t}{\Delta U(x - x_o)}$
Miles and Shih	
$\frac{U_2}{U_1} = 0.47$	0.0010
Spencer and Jones	
$\frac{U_2}{U_1} = 0.30$	0.00114
Present experiment	
$\alpha = 0$	
$\rho_1 U_1^2 = \rho_2 U_2^2$	0.0016
$\frac{U_2}{U_1} = 0.378$	

Again, the bigger eddy viscosity indicates a faster spreading for the variable density case, but not greatly so.

On the other hand, the value of $\frac{\nu_t}{\Delta U(x-x_o)} = 0.0040$ for $\alpha = -0.18$ comes from the fact that the adverse pressure gradient stretches the velocity profile and substantially increases the shear stress across the layer (cf. Eq. 8.1.1)

---

* Our value $\frac{\nu_t}{\Delta U(x - x_o)}$ has been calculated from equation (8.1.1)

9.2b Density Profiles and Large Structure Model

With respect to the profiles of density and rms density fluctuations it is interesting to note the completely different behavior on the nitrogen and on the helium sides (Figs. 24 and 25). On the low speed side the density rapidly drops to lower values and the rms density fluctuations have a large peak to peak amplitude, approximately 40% of the overall density difference, whereas on the high speed side the average density is fairly uniform and the amplitude of the fluctuations is not larger than 10%. This would seem to suggest that the gases are more thoroughly mixed in the low density side of the mixing layer.

A possible explanation can be found if we regard the large structure as a rolled up vortex sheet which is separating the two gases at all times except for the molecular diffusion occurring across it.

An aspirating probe placed at any point in this type of shear layer would see large fluctuations of density distributed in a bimodal fashion, in contrast to a narrow gaussian distribution for a well diffused mixture at that point.

We suggest the existence of an instability phenomenon combined and interacting with the rolled, diffused vortex sheet, which by extrapolation of Davey's (Ref. 29) findings to turbulent flows would result in a more sharp and stable interface on the nitrogen side as compared tothe helium part of the layer, where light gas going at high speed and heavy gas at low form an unstable situation; in consequence a less sharp and more diffused separation between the two gases will develop (see illustration below and cf. Fig. 13).

The density probability function for this model would be somewhere in between the bimodal and gaussian distributions. Figures 47 and 48 show a complete density traverse for the $\alpha = 0$ case.

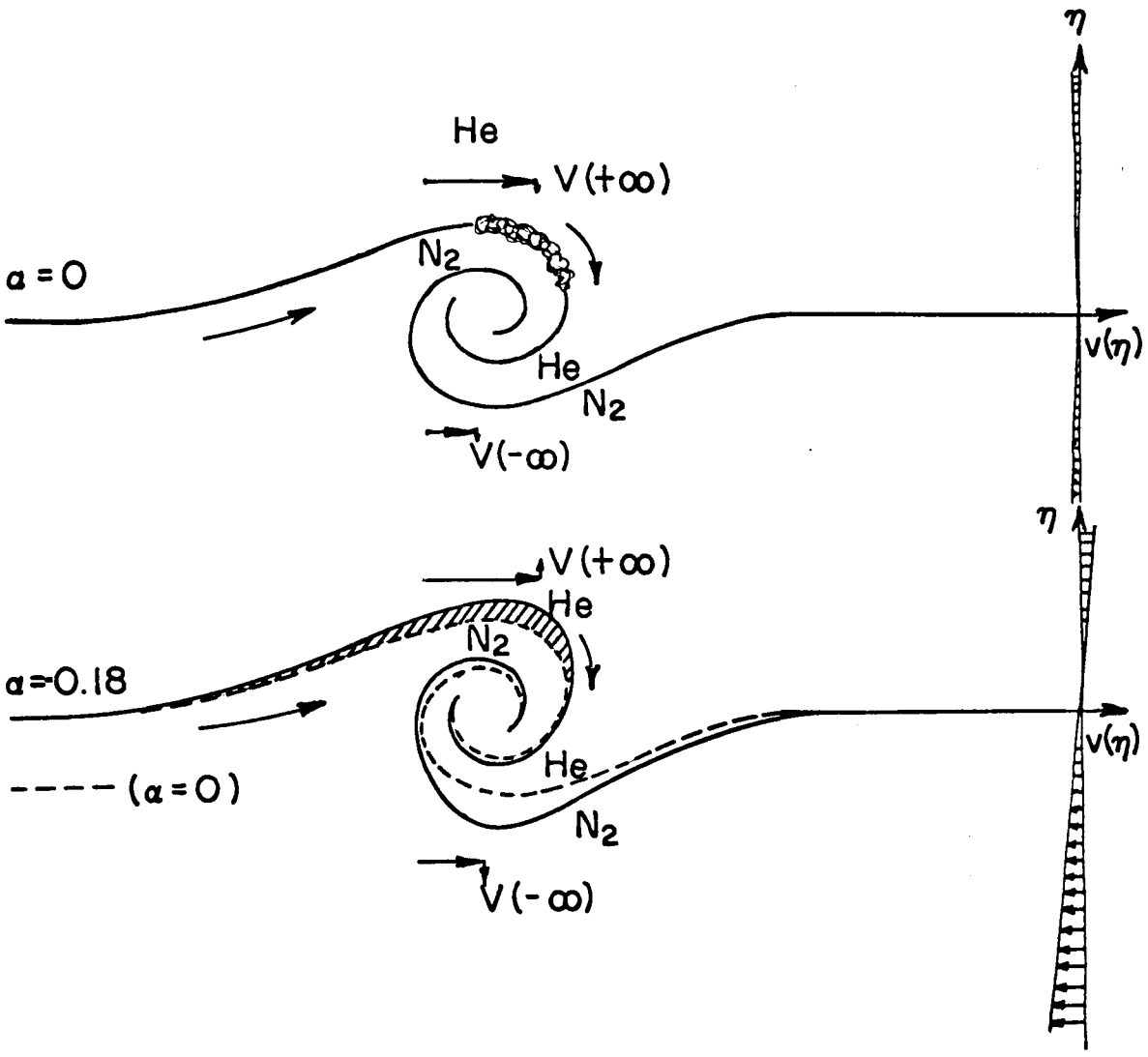

9.2c Effect of Adverse Pressure Gradient on the Large Structure

A possible understanding of the effect of an adverse pressure gradient on the above large structure model can be found by calculating the velocity outflow from equations (2.3.12) and (2.3.13).

For $\alpha = 0$, $\rho_1 U_1^2 = \rho_2 U_2^2$

$$\left.\begin{aligned} \frac{V(+\infty)}{U_1} &\simeq -0.025 \\ \frac{V(-\infty)}{U_2} &\simeq -0.056 \end{aligned}\right\}^{*}$$

The minus sign comes from the fact that the high velocity (low density) side has the lowest value of ρU across the layer, so that $\rho_1 U_1 - \rho U < 0$ throughout.

For the adverse pressure gradient we have a divergent V velocity field superposed on the constant entrainment velocity (see Sec. 2.3b). It should be noted that this divergent velocity field is produced by the adverse pressure gradient through the terms $-\alpha \int_0^{\infty} \rho u \, dx$ and $-\alpha \int_0^{-\infty} \rho u \, dx$ in equations (2.3.12) and (2.3.13).

By putting $\xi_o = 0$ in our experimental profiles, and considering that $\xi = 0.165$ and $\xi = -0.26$ roughly correspond to the outer edges of the shear layer we get:

$$\frac{V(+\infty)}{U_1} \simeq 0.0097 - \alpha(\xi - 0.165) \text{ for } \xi > 0.165$$

$$\frac{V(-\infty)}{U_1} \simeq 0.14 - \alpha(\xi + 0.26) \text{ for } \xi < -0.26$$

---

* As compared with Miles and Shih (Ref. 27) values for a homogeneous mixing layer with $U_2/U_1 = 0.47$; i.e., $V(+\infty)/U_1 = 0.005$, $V(-\infty)/U_2 = 0.014$.

Consequently, the lateral velocity on the low speed side could be as high as 16% of the longitudinal velocity*.

We believe that this divergent and strong lateral velocity field, produced by the adverse pressure gradient, stretches the vortices in the vertical direction and squeezes them in the streamwise direction (see illustration above and cf. Fig. 13).

Probably, the process mentioned above increases the fluctuation level in the velocity field, but the straining of the interface between the two gases produces no significant modification on the characteristics of the concentration profile or in the density fluctuations, except for a scale factor and perhaps minor alterations on the helium side, where the interface is more diffused and we would expect stronger coupling between the velocity and density fields.

This reasoning can be illustrated by plotting, for both flows, $\alpha = -0.18$ and $\alpha = 0$, the rms density fluctuations at any point across the layer against the average density corresponding to that point (Fig. 49). This figure shows that for a certain value of the average density the rms density fluctuations are almost the same for the zero and adverse pressure gradients, except for the low densities, where slightly higher values of the fluctuations are found for the adverse pressure gradient case.

---

* Note that $U_2/U_1 \simeq 0.38$ and $U_{min}/U_1 \simeq 0.34$

9.3 Conclusion

We have shown analytically that turbulent mixing layers between two streams of different gases in pressure gradients can have equilibrium structure provided $\rho_1 U_1^2 = \rho_2 U_2^2$ and $\alpha = \frac{x}{U_1}\frac{dU_1}{dx} = \text{const.}$ In this case, $\delta \sim x$, i.e., the spreading is linear in x. Such an equilibrium flow has been set up experimentally in our turbulent mixing apparatus and its properties for $\alpha = -0.18$ and $\alpha = 0$ have been measured. The similarity properties have been established from mean profiles of dynamic pressure and density. The profiles of rms density fluctuations have also been shown to be self-preserving.

It has been found that for an adverse pressure gradient of $\alpha = -0.18$ the turbulent mixing layer spreads about 60% faster than for $\alpha = 0$ (zero pressure gradient).

Maximum shear stress is about 70% higher while the turbulent mass diffusion is only 20% higher; on the other hand, rms density fluctuations are nearly the same, and approximately 20% of the overall density difference, in both flows.

It seems fairly reasonable to conclude that the adverse pressure gradient primarily effects the fluctuating velocity field and hence the transport of momentum.

Turbulent Schmidt numbers are very low; e.g., 0.2 for $\alpha = 0$ and 0.3 for $\alpha = -0.18$. As a result, a large deficiency of dynamic pressure is found on the low speed (high density) side of the layer, possibly resulting in flow reversal for higher values of α (stronger adverse pressure gradient).

APPENDIX A

ASYMPTOTIC BEHAVIOR OF NUMERICAL SOLUTION

Having in mind equations (3. 1. 3) through (3. 1. 8) we shall assume that:

$$A(\eta) = A_o + A_{11} + \ldots\ldots$$

$$u(\eta) = 1 + u_{11} + \ldots\ldots$$

$$\rho = 1 + \rho_{11} + \ldots\ldots$$

$$X = 0 + X_{11} + \ldots\ldots$$

as $\eta \to +\infty$

where $u_{11} << 1$, $\rho_{11} << 1$, $A_{11} << A_o \ldots$

For the sake of abbreviation we shall call

$$\frac{C_\mu}{\beta}\frac{\Delta U}{U_1} = \gamma$$

Integrating the diffusion equation and knowing that $A(\eta_o = 0) = 0$, it can be seen that as $\eta \to +\infty$

$$A_o(\eta) \simeq -(1 + \alpha)\eta$$

Equations (3. 1. 3) and (3. 1. 5) are reduced to

$$-(1 + \alpha)\eta X_{11} + A'_{11} + (1 + \alpha)u_{11} = 0$$

$$A'_{11} + (1 + \alpha)u_{11} = -\frac{\gamma}{Sc_t} X'_{11}$$

Eliminating $A'_{11} + (1 + \alpha)u_{11}$ between these two equations and considering that $X_{11} < 0$, for all η

$$X_{11} = -|a|\, e^{-\frac{Sc_t}{\gamma}\frac{(1+\alpha)}{2}\eta^2}$$

where $|a| > 0$ is a constant.

From the definitions of X and Y we get

$$Y = u_{11}' + \text{H.O.T.}$$

$$X_{11} = \rho_{11}' + \text{H.O.T.}$$

Consequently

$$\rho_{11} \simeq |a| \int_{\eta}^{\infty} e^{-\frac{Sc_t}{\gamma} \frac{(1+\alpha)}{2} \chi^2} d\chi \quad \text{as } \eta \to +\infty .$$

The momentum equation becomes

$$\gamma u_{11}'' + (1 + \alpha)\, \eta\, u_{11}' - 2\alpha u_{11} = b \frac{e^{-\frac{Sc_t}{2} \zeta^2}}{\zeta}$$

where $\zeta = \sqrt{\frac{1 + \alpha}{\gamma}}\, \eta$

$$b = \frac{|a|\, \alpha\, \gamma^{\frac{1}{2}}}{Sc_t\, (1+\alpha)^{3/2}}$$

and ρ has been expanded in $\frac{1}{\eta}$ as $\eta \to +\infty$.

Now let $u_{11} = e^{-\sigma\zeta^2} w$, and we will have for $\sigma = \frac{1}{4}$

$$\ddot{w} - [\frac{1}{4} \zeta^2 + (\frac{1}{2} + \frac{2\alpha}{1 + \alpha})] w = \frac{b\, e^{-(\frac{1}{2} - Sc_t) \frac{\zeta^2}{2}}}{\zeta}$$

This equation with the right hand side equal to zero belongs to the class of parabolic cylinder functions and its solution can be found in Abramowitz "Handbook of Mathematical Functions", Sec. 19.

There are two independent solutions

$$w_1 \simeq e^{-\frac{1}{4}\zeta^2}\, \zeta^{-(1+\frac{2\alpha}{1+\alpha})} \left[1 + 0\left(\frac{1}{\zeta^2}\right)\right]$$

$$w_2 \simeq e^{\frac{1}{4}\zeta^2}\, \zeta^{\frac{2\alpha}{1+\alpha}} \left[1 + 0\left(\frac{1}{\zeta^2}\right)\right]$$

as $\zeta \to +\infty$.

Using the Green's function for the forced solution, and assuming that $u_{11} \to 0$ as $\eta \to +\infty$ and $Sc_t < 1$ we get

$$u_{11} \simeq \frac{-|a|\,\alpha\,(\frac{U_1+U_2}{2U_1})^{\frac{1}{2}}}{(1+\alpha)^{3/2} Sc_t^{\,2}(1-Sc_t)}\, \frac{e}{\eta^3}^{-Sc_t(\frac{U_1}{U_1+U_2})\,(1+\alpha)\,\eta^2} \left\{1 + 0\left(\frac{1}{\eta^2}\right)\right\}$$

if

$$\rho_{11} \simeq \frac{|a|\,(\frac{U_1+U_2}{2U_1})}{Sc_t\,(1+\alpha)}\, \frac{e}{\eta}^{-Sc_t(\frac{U_1}{U_1+U_2})\,(1+\alpha)\,\eta^2} \left\{1 + 0\left(\frac{1}{\eta^2}\right)\right\}$$

where $\gamma = \frac{1}{2}\,\frac{U_1+U_2}{U_1}$ has been substituted*.

Hence for $-1 < \alpha < 0$ and $\eta \to +\infty$, $\rho_{11} > 0$, and $u_{11} > 0$, the velocity profile will therefore approach the free stream value from above (overshoot).

---

* See our definition of β in section 3.2.

To study the asymptotic behavior as $\eta \to -\infty$ we assume

$$A(\eta) = A_o + A_{12} + \cdots\cdots$$

$$u(\eta) = \left(\frac{\rho_1}{\rho_2}\right)^{\frac{1}{2}} + u_{12} + \cdots\cdots$$

$$\rho = \left(\frac{\rho_2}{\rho_1}\right) + \rho_{12} + \cdots\cdots$$

$$X = X_{12} + \cdots\cdots$$

and following the same pattern we have used before we find that

$$u_{12} \simeq \frac{-|a_2|\,\left(\frac{U_1+U_2}{2U_1}\right)^{\frac{1}{2}}\left(\frac{\rho_1}{\rho_2}\right)^{5/4}\alpha}{Sc_t^{\,2}(1-Sc_t)\,(1+\alpha)^{3/2}}\,\frac{e}{\eta^2} - Sc_t\left(\frac{U_1}{U_1+U_2}\right)(1+\alpha)\left(\frac{\rho_1}{\rho_2}\right)^{\frac{1}{2}}\eta^2 \left\{1 + 0\left(\frac{1}{\eta^2}\right)\right\}$$

if

$$\rho_{12} \simeq \frac{|a_2|\,\left(\frac{U_1+U_2}{2U_1}\right)}{Sc_t\,(1+\alpha)\left(\frac{\rho_1}{\rho_2}\right)^{\frac{1}{2}}}\,\frac{e}{\eta} - Sc_t\left(\frac{U_1}{U_1+U_2}\right)(1+\alpha)\left(\frac{\rho_1}{\rho_2}\right)^{\frac{1}{2}}\eta^2 \left\{1 + 0\left(\frac{1}{\eta^2}\right)\right\}$$

as $\eta \to -\infty$.

Hence if $-1 < \alpha < 0$ and $\eta \to -\infty$ and $\rho_{12} < 0$ and $u_{12} < 0$, that is to say, the velocity will tend towards its free stream value from below (undershoot).

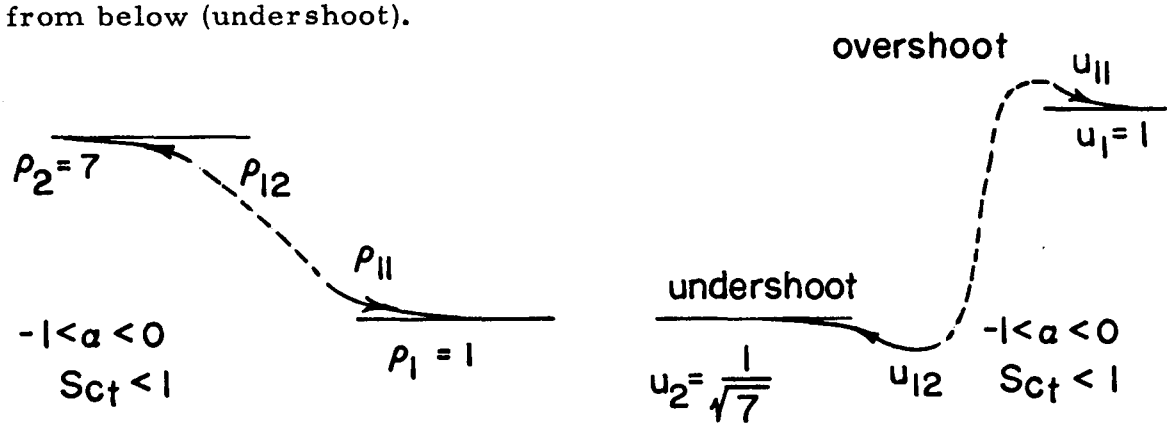

Reprinted from AIAA JOURNAL, Vol. 10, No. 5, May 1972, pp. 649-652

APPENDIX B

A Small, Fast-Response Probe to Measure Composition of a Binary Gas Mixture

G. L. BROWN* AND M. R. REBOLLO†
California Institute of Technology, Pasadena, Calif.

A probe to measure the concentration of the components in a binary mixture of gases is described. The probe is simple to construct and quite rugged. It samples from a very small volume, has a fast time response and can very easily detect 1% of helium in nitrogen. The explanation of the principle of operation is a good example of the power of dimensional analysis when applied to what may seem to be quite a complicated and unfamiliar problem. The analysis suggests several experiments which in turn lead to a more detailed understanding of the probe and improvements in its design.

Nomenclature

a = velocity of sound
c_p, c_v = specific heats
d = hot wire diameter
k = thermal conductivity
Kn_∞ = Knudsen number = $(\lambda_\infty/d) = (\gamma\pi/2)^{1/2}(M_\infty/Re_\infty)$
M = Mach number
MW = molecular weight
Nu_o = Nusselt number = $[q/T_w - T_r]d/k_o$
p = pressure
p_d = downstream pressure
q = convective heat-transfer rate
Q = additional power required to keep wire at T_w when probe is placed in a gas
R = gas constant
R_w = hot wire resistance at T_w
Re_o = Reynolds number = $\rho_\infty u_\infty d/\mu_o$
T = temperature
T_w = temperature of the wire
T_r = recovery temperature of the wire
u = velocity
U = sampled gas velocity relative to the probe
V = bridge voltage
V_o = bridge voltage for probe in vacuum
α = energy accommodation coefficient
γ = specific heat ratio = c_p/c_v
ρ = density
λ = molecular mean free path
μ = viscosity

Subscripts and Superscripts

$( )_o$ = stagnation conditions
$( )_\infty$ = freestream conditions
$( )^*$ = sonic conditions

Introduction

THIS work was stimulated by a need to measure the local composition in a plane turbulent mixing layer between two different gas streams. In our experiments these gases are usually nitrogen and helium. A small sampling volume, an output independent of the velocity of the fluid relative to the probe, and a response time of milliseconds or less were essential requirements to be met. The probe which was developed has some features in common with the "heat flux probe for high temperature gases" of Blackshear and Lingerson,[1] and the aspirating probe used by D'Souza, Montealegre and Weinstein.[2]

Received September 9, 1971; revision received December 22, 1971. The authors gratefully acknowledge many profitable discussions with A. Roshko and J. E. Broadwell. We are indebted to the Department of the Navy, Office of Naval Research, who supported this work.

Index categories: Research Facilities and Instrumentation; Multiphase Flows.

* Senior Research Fellow, Graduate Aeronautical Laboratories.

† Graduate Student and Research Assistant, Graduate Aeronautical Laboratories.

1. Description

The probe is sketched in Fig. 1. Its construction is simple, particularly with the assistance of a glass-blower. The tip is 2 mm glass tubing drawn to a point and then polished to expose a fine hole. In our case the effective diameter of this hole is 0.001 in., determined from the measurements described in Sec. 5. Two holes approximately 0.010 in. in diam and as near as practicable to the tip were made opposite each other in the walls of the tubing with a hot tungsten wire. Bared copper leads were then glued to the outside of the tubing and an unetched Wollaston wire poked through the holes in the tubing walls and soldered at each end to the copper leads. The soldered joints and the holes were then covered with epoxy, care being taken to prevent the epoxy running along the Wollaston wire. When the glue was well cured, nitric acid was sucked into the tube and allowed to etch the wire up to the epoxy and expose the thin (0.0005 in.) platinum wire. The tubing was then slipped into a brass holder and sealed in place with shrinkable tubing.

2. Principle of Operation

The probe is attached to a vacuum pump and the platinum wire maintained at some fixed temperature T_w (i.e., resistance R_w) above its surroundings with the usual feedback bridge. If the probe is placed in a vacuum some electrical power V_o^2/R_w is required to maintain the wire at the temperature T_w because of heat conduction losses. The additional power $Q = (V^2 - V_o^2)/R_w$ required to keep the wire at this temperature when the probe is placed in a gas (or gas mixture) is then a function of the following variables

$$Q = f(p_o, \rho_o, T_o, R, C_p, \mu_o, k_o, d, T_w, p_d) \quad (1)$$

where R is the gas constant, p_d the downstream vacuum

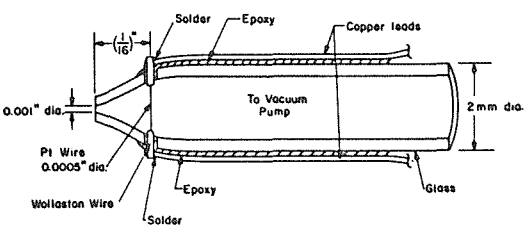

Fig. 1 Sketch of the probe.

pressure, d a characteristic dimension of geometrically similar probes (e.g., wire diameter) and the other symbols have their usual meanings. (The o subscript refers to stagnation conditions in the gas being sampled.) Dimensional analysis then requires that

$$\frac{Q}{kT_o d} = f\left(\frac{p_o}{\rho_o RT_o}, \frac{\rho_o (RT_o)^{1/2} d}{\mu_o}, \frac{\mu_o c_p}{k_o}, \frac{c_p}{R}, \frac{T_w}{T_o}, \frac{p_d}{p_o}\right) \quad (2)$$

Ideally the parameter p_d/p_o can be made arbitrarily small and negligible with a vacuum pump of sufficient capacity, in which case the output Q depends only on stagnation variables. If the sampled gas moves relative to the probe with a velocity U then, to order $(U/a_o)^2$ (a_o is the stagnation velocity of sound), all of the above parameters have the same value if evaluated at static conditions as they do at stagnation conditions. That is, for the same static temperature in the gas being sampled, the output of the probe depends on the gas and not on the velocity of the gas relative to the probe if $U \ll a_o$. The experiment described in the following sections makes it possible to state this a little more precisely. It should be noted that for perfect gases having the same Prandtl number Eq. (2) may be reduced to

$$\frac{Q}{k(T_w - T_o)d} = f\left(\gamma, \frac{\rho_o a_o d}{\mu_o}, \frac{T_w - T_o}{T_o}\right) \quad (3)$$

or, if T_o is constant

$$\frac{Q}{k(T_w - T_o)d} = f\left(\gamma, \frac{p_o a_o d}{\mu_o}\right) \quad (4)$$

For a given flow at the wire and small values of $(T_w - T_r)/T_r$ (where T_r is the recovery temperature of the unheated wire) one expects the equation for the additional temperature field (due to the heating of the wire) to be linear, that is for Q to be proportional to $(T_w - T_r)$. Since the recovery temperature is very nearly the stagnation temperature for circular cylinders, over a very large Reynolds number and Mach number range (Baldwin, Sandborn, Laurence[3]), T_r is approximately T_o (assuming adiabatic flow up to the wire) so that one expects Eq. (4) to apply even if there are small variations in T_o.

3. Calibration and an Experiment

The probe was placed in various gases and gas mixtures contained in a 500 cubic in. volume.

In the case of mixtures, the order in which the gases were added was varied and measurements recorded when the results were independent of this order. The volume was filled to about 105 psia and then bled slowly, measurements being made at various pressures down to $\frac{1}{2}$ psia. During this process, the temperature of the gas mixture in the volume did not differ perceptibly from room temperature. It is worth noting that at any one pressure the voltmeter reading was steady within about 1 millivolt (cf. Fig. 2). A cross plot of bridge output in volts against molar concentration of helium in nitrogen for various pressures is shown in Fig. 2.

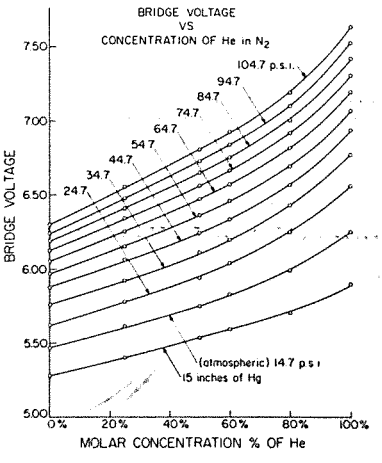

Fig. 2 Bridge voltage vs concentration of He in N_2.

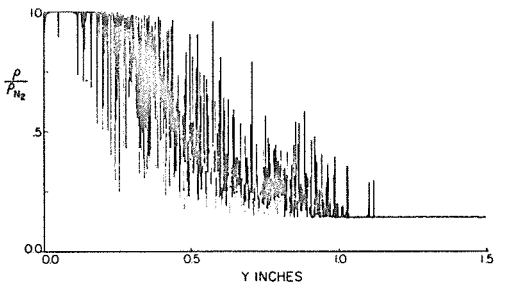

Fig. 3 Density traverse across the layer.

An example of a measurement which made use of these calibration curves is shown in Fig. 3; it is an illustration of the success with which the probe meets the requirements listed in the Introduction. The measurement consisted of traversing the probe across a plane turbulent mixing layer between nitrogen and helium (at room temperature, a pressure of 7 atm and very low Mach number) and measuring the concentration every one thousandth of an inch. The traverse was at a rate of 2 sec/in. so that a sample was obtained every 2 msec. The probe output, after A/D conversion and reduction to values of concentration is shown in Fig. 3. This computer plot draws a continuous line between individual data points, so the latter are not clearly distinguishable. Nevertheless it may be seen that the probe responds to very large changes of concentration in less than 2 msec. The ripple at each end of the traverse corresponds to changes in the least significant bit of the A/D converter. It is noted that at no point is the computed density greater than the density of N_2 or less than that of He; if there were any such points, a sensitivity to velocity would be implied. A more complete account of the experiment is given in Ref. 8.

4. Accommodation Effects

Although the calibration curves (Fig. 2) were sufficient for using the probe to measure concentration, they defied correlation in terms of Eq. (4) and we were prompted to look particularly at gases having the same γ.

Again by varying the pressure in the volume, results for He, Ar, and Kr were obtained (Fig. 4). It is clear from this figure that Eq. (4) does not correlate the measurements and it is shown in Sec. 6 that the parameter p_d/p_o, assumed insignificant, was sufficiently small for its variation to be unimportant. Evidently variables which are significant have been ignored in the dimensional analysis. Those most likely overlooked would seem to be those needed to describe accommodation effects at the wire surface, particularly the properties of the surface itself since the atomic cross section of the gas (and therefore the Knudsen number) is not an independent variable but is determined by ρ_o, a_o, and μ_o. Such effects have been observed previously with hot wires in helium (Aihara, Kassoy, Libby[4]).

If the energy accommodation coefficient at the wire surface is α, then it is expected[5] that a plot of Nu_o/α against $\rho_o a_o d/\mu_o$ should correlate the data. Values of α were chosen to give the best collapse of the data for argon and helium (shaded points in Fig. 4) onto the data for krypton. In effect, this means choosing a ratio for the accommodation coefficients of helium and krypton and a ratio for those of argon and krypton. These ratios are 0.43 for helium and 0.87 for argon. The absolute value of α for krypton is expected to be near unity. Although

the accommodation coefficients of inert gases depend strongly on surface conditions[9] and surface temperature, these values for the ratios are not atypical.

5. Mass Flow in the Probe

The Reynolds number at the orifice, assuming sonic conditions, is quite large (150 to 3000) but downstream of the tip as the cross-sectional area increases it becomes correspondingly much smaller and it is perhaps not obvious that the flow is in fact choked at the tip. The following experiment answered this question and also led to conclusions about the flow conditions at the wire.

A volume was filled with gas to 105 psia and then bled through the probe orifice to approximately 40 psia. The temperature in the volume remained essentially constant. Measurements were made of the decay in gas pressure as a function of time and the results for argon and helium are plotted in Fig. 5. Evidently the rate of pressure decay is directly proportional to gas pressure (i.e., pressure is an exponential function of time) down to pressures in helium of, say, 25 psig. Above this pressure the mass flow rate (proportional to dp/dt for constant temperature in the volume) is therefore proportional to gas density and in fact the ratio of the proportionality constant for these two gases is the same as the ratio of their sound velocities. Assuming choked conditions the calculated effective orifice diameter (0.0011 in) was as near the physical diameter as we could determine with a microscope. The flow was therefore choked at the tip and the mass flow rate independent of viscosity for throat Reynolds numbers greater than, say, 300.

6. Flow Conditions at the Wire

Although it is not required for using the calibrated probe, it is of interest to try to understand flow conditions at the wire. This is not simple to determine theoretically; although viscosity has no effect on the mass flow, it will have a considerable effect on the flow up to the wire, which is in a section of the channel of much larger area. There exists the possibility of expansion to supersonic velocities, the existence of diffuser shock waves, the possibility of reaching rarefied flow conditions, etc., all of these dependent on area ratio, pressure ratio and effects of viscosity.

Knowing the mass flow, the heat-transfer rate and wire temperature, we can estimate a Nusselt number and a wire Reynolds number ($\rho ud/\mu_o$) by assuming an effective length for the wire. (It is also assumed that this length is the effective diameter of the mass flow.) Given a plot of Nu against Re for various Mach numbers (Refs. 7 and 3), an iteration leads to an estimate of the Mach number. For the probe described previously this was found to be a low value, about 0.1 with Reynolds number varying with pressure from about 1.0 to 10.

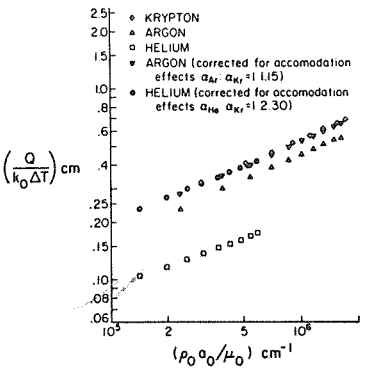

Fig. 4 $(Q/k_o \Delta T)$ cm vs $(\rho_o a_o/\mu_o)$ cm^{-1}.

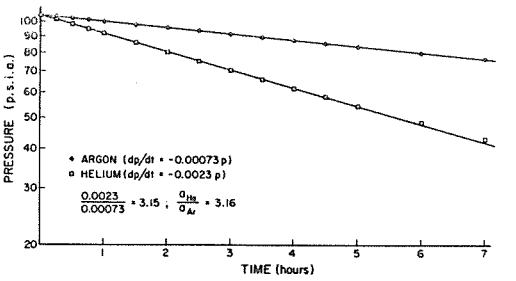

Fig. 5 Pressure vs time for Ar and He.

In this range, the slope of the Nu-Re curve on a log-log plot is closer to $\frac{1}{2}$ than 1, as indeed we observe (Fig. 4).

That the flow at the wire was evidently subsonic raised the question of whether or not the output of the wire was independent of the vacuum pump and plumbing (expressed simply by the parameter p_d/p_o). The iteration described leads to an estimate for the pressure at the wire, namely 50 mm Hg, typically. The measured pressure at the pump in this case was 15 μHg which agreed well with the manufacturer's claim of 20 μHg for the measured mass flow. Changing the pressure at the pump from 15 μHg to 3.5 mmHg produced no change in probe output. It appears then that from the tip to the pump there may be a number of sonic throats before which there is viscous compressible flow and an acceleration from subsonic to sonic velocity. This conclusion was further supported by measurements of the pressure downstream of the wire (pressure typically 1 mmHg). The ratio of this pressure to the stagnation pressure was the same for the same throat Reynolds number in helium and argon (quite different stagnation pressures), as dimensional analysis demands if p_d/p_o is negligible.

The estimated Knudsen number at the wire is less than 0.1. It is interesting that accommodation effects occur even at these low values, as has indeed been observed by other investigators.

7. Sensitivity to Velocity

To test the probe sensitivity to velocity we placed it in a uniform stream of helium at three different velocities (270 cm/sec, 1000 cm/sec and 1770 cm/sec). The output was unaffected by velocity; the relative error in bridge output voltage was smaller than $\frac{1}{2}$% at the highest velocity.

With the information that we have, one can estimate the error made if one determines the concentration of a moving gas with a probe that has been calibrated in stationary mixtures, the static temperatures being the same in both cases. If the Mach number of the moving gas (i.e., U/a) is M then the

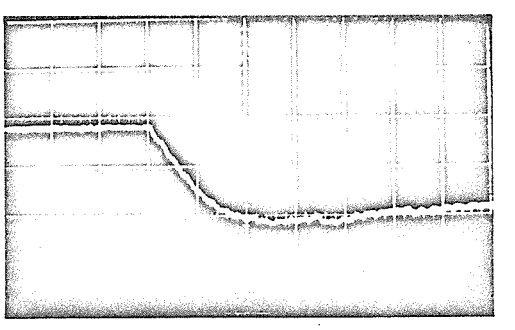

Fig. 6 Rise time output: Oscilloscope photo of response of probe to passage of shock wave; horizontal scale: 100 μsec/div; vertical scale: 0.05 v/div.

relative error in the determined apparent molecular weight MW is, roughly, for small Mach number

$$\Delta(MW)/MW \simeq [T_w/(T_w - T_o) - 2]M^2 \quad (5)$$

or less, if γ and α vary with concentration.

8. Time Response

As the distance from the orifice in the tip to the wire is small and the gas velocity is of the order of the speed of sound a time response of μsec might be expected, unless the size of the hot wire and the electronics limit it to a longer time.

A new probe with a smaller wire diameter (0.0001 in.) and a less rapid area expansion (based on the findings in Sec. 6) was constructed and placed in the end wall of a shock tube. The gas in the tube was nitrogen, initially at atmospheric pressure. A shock wave passing by the probe produced an instantaneous change in the stagnation conditions of the sampled gas and the corresponding change in probe output was photographed (Fig. 6), (time scale = 100 μsec/cm, vertical scale = 0.05 v/cm). The response time is evidently about 200 μsec. The experiment was repeated using helium instead of nitrogen and, as expected, the rise time was faster. It is noted that a much longer time response is associated with the warming up of the glass.

References

[1] Blackshear, Perry L. and Lingerson, Leroy, "Rapid-Response Heat Flux Probe for High Temperature Gases," *ARS Journal*, Vol. 32, No. 1, Nov. 1962, pp. 1709–1715.

[2] D'Souza, Gerard J., Montealegre, Anthony, and Weinstein, Herbert, "Measurement of Turbulent Correlations in a Coaxial Flow of Dissimilar Fluids," CR-970, Jan. 1968, NASA.

[3] Baldwin, L. V., Sandborn, V. A., and Laurence, J. C., "Heat-Transfer from Transverse and Yawed Cylinders in Continuum, Slip and Free Molecule Air Flows," *Journal of Heat Transfer*, Vol. 82, No. 1, May 1960, pp. 77–86.

[4] Aihara, Y., Kassoy, D. R., and Libby, Paul A., "Heat Transfer from Circular Cylinders at Low Reynolds Numbers," *The Physics of Fluids*, Vol. 10, No. 1, May 1967, pp. 947–952.

[5] Loeb, Leonard B., "The Laws of Rarefied Gases and Surface Phenomena," *The Kinetic Theory of Gases*, 3rd ed., Dover, 1961, pp. 278–364.

[6] Faust, J. W., "Accommodation Coefficient of Inert Gases on Al and Pt and Their Dependence on Surface Condition," Ph.D. thesis, 1954, Univ. of Missouri, Columbia, Mo.

[7] Dewey, C. Forbes, Jr., "A Correlation of Convective Heat Transfer and Recovery Temperature Data for Cylinders in Compressible Flow," *International Journal of Heat and Mass Transfer*, Vol. 8, No. 1, Feb. 1965, pp. 245–252.

[8] Brown, G. L., and Roshko, Anatol, "The Effect of Density Differences on the Turbulent Mixing Layer," AGARD Conference Proceedings Turbulent Shear Flows, Nov. 1971, to be published.

APPENDIX C

An Estimate of the Error in the Measurements of Dynamic Pressure

The impact or pitot tube responds to the time-averaged total head as given by*:

$$(P_T)_{measured} \simeq P_{static} + \frac{1}{2}\overline{(\bar{\rho} + \rho')\,(U + u')^2}$$

The static pressure, P_{static}, was monitored inside the shear layer by mounting the static pressure tube side by side with the pitot tube. Hence for the method employed to measure profiles,

$$(\Delta p)_{measured} \simeq \frac{1}{2}\overline{(\bar{\rho} + \rho')\,(U + u')^2} + P_{static} - P_{static} \quad **$$

$$(\Delta p)_{measured} \simeq \frac{1}{2}\left\{\bar{\rho}U^2 + \overline{\rho u'^2} + 2\,U\overline{\rho' u'}\right\}$$

Therefore,

$$\frac{(\Delta p)_{measured}}{\frac{1}{2}\bar{\rho}\,U^2} \simeq 1 + \frac{\overline{\rho u'^2}}{\bar{\rho}U^2} + 2\,\frac{\overline{\rho' u'}}{\bar{\rho}\,U}$$

For a physical situation as illustrated below

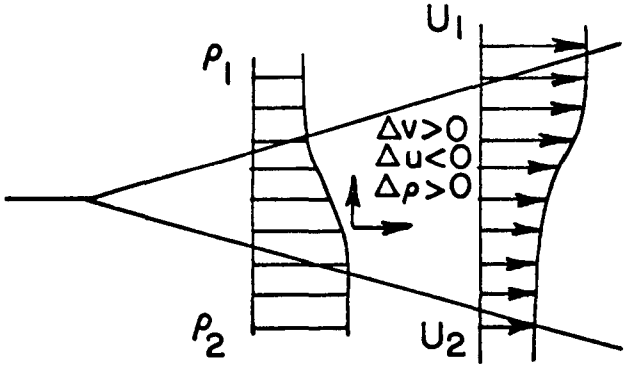

(e.g., $\rho_1 U_1^2 = \rho_2 U_2^2$)

$\overline{\rho' u'} < 0$ negatively correlated

$\overline{\rho' v'} > 0$ positively correlated

---

* Assuming yaw angles smaller than $\simeq 15^{\circ}$.

** If the static part were remote, there would be a residual static fluctuation.

$$\overline{\rho' u'} \qquad |k_1| \sqrt{\overline{\rho'^2}} \sqrt{\overline{u'^2}}$$

$$\overline{\rho' v'} = k_2 \sqrt{\overline{\rho'^2}} \sqrt{\overline{v'^2}}$$

where - $|k_1|$ is the correlation coefficient between $\sqrt{\overline{\rho'^2}}$ and $\sqrt{\overline{u'^2}}$ and k_2 is the correlation coefficient between $\sqrt{\overline{\rho'^2}}$ and $\sqrt{\overline{v'^2}}$.

Assuming that $\sqrt{\overline{u'^2}} \sim \sqrt{\overline{v'^2}}$

$$|\overline{\rho' u'}| \leq \overline{\rho' v'}$$

since you would expect $\sqrt{\overline{\rho'^2}}$ and $\sqrt{\overline{v'^2}}$ to be more highly correlated than $\sqrt{\overline{\rho'^2}}$ and $\sqrt{\overline{u'^2}}$, i.e., $k_2 \geq |k_1|$.

From our distribution of turbulent mass diffusion we found that $\left(\frac{\overline{\rho' v'}}{\rho_1 U_1}\right)_{\text{maximum}} \simeq 0.07$; consequently,

$$2\left(\frac{\overline{\rho' u'}}{\bar{\rho} U}\right) \simeq -2 \frac{|k_1|}{k_2} \left(\frac{\overline{\rho' v'}}{\rho_1 U_1}\right) \left(\frac{\rho_1 U_1}{\bar{\rho} U}\right)$$

$$\simeq -\frac{|k_1|}{k_2} \, 0.07$$

where $\frac{|k_1|}{k_2} \leq 1$

The maximum value of $\overline{u'^2}/U_1^2$ in a turbulent mixing layer is from 0.15 to 0.20 (Refs. 25 and 26); therefore,

$$\frac{\overline{\rho u'^2}}{\bar{\rho} U^2} \simeq 0.03$$

We estimate that we are introducing an error which will not be larger than approximately 4 or 5%

$$\frac{(\Delta p)_{measured}}{\frac{1}{2}\bar{\rho}\,U^2} \simeq 1 + \underbrace{\left(\frac{\overline{\rho u'^2}}{\bar{\rho}\,U^2}\right)}_{3\%} + \underbrace{\left(\frac{2\,\overline{\rho' u'}}{\bar{\rho}\,U}\right)}_{-7\%}$$

We should mention that (neglecting potential fluctuations) had we been monitoring the static pressure in the free stream, the error would have been of the order of 10% instead of 4%, since

$$(\Delta p)_{measured} \simeq \frac{1}{2}\,\overline{(\rho + \rho')(U + u')^2} + P_{static} - (P_{static})_\infty$$

But from the y-momentum equation we know that

$$P_{static} \simeq (P_{static})_\infty - \overline{\rho v'^2}$$

Hence

$$\frac{(\Delta p)_{measured}}{\frac{1}{2}\bar{\rho}\,U^2} \simeq 1 + \underbrace{\left(\frac{\overline{\rho u'^2}}{\bar{\rho}\,U^2}\right)}_{+3\%} + \underbrace{\left(\frac{\overline{\rho' u'}}{\bar{\rho}\,U}\right)}_{-7\%} - \underbrace{\left(2\,\frac{\overline{\rho v'^2}}{\bar{\rho}\,U}\right)}_{-6\%}$$

Assuming that $\overline{\rho u'^2} \sim \overline{\rho v'^2}$ (you would expect triple correlations to be small compared to double correlations); we could have had about 10% error.

On the other hand, for a physical situation where $\overline{\rho' u'} > 0$, it would be advantageous to measure $(P_{static})_\infty$ instead of P_{static}.

It is clear that direct measurements of the velocity would be more satisfying. Such measurements could be made using some type of laser doppler system, although some difficulties are being experienced in applying these systems to turbulent flow in gases.

REFERENCES

1. Brown, G. L., and Roshko, A., The Effect of Density Difference on the Turbulent Mixing Layer, AGARD Conference Proceedings Turbulent Shear Flows, (1971).

2. Hartree, D. R., On an Equation Occurring in Falkner and Skan's Approximate Treatment of the Equations of the Boundary Layer, Proceedings Cambridge Philosophical Society, 33, Part II, pp. 223-239, (1937).

3. Clauser, F. H., Turbulent Boundary Layers in Adverse Pressure Gradients, Journal of the Aeronautical Sciences, 21, pp. 91-108, (1954).

4. Townsend, A. A., The Structure of Turbulent Shear Flow, Cambridge University Press, London, (1956).

5. Wygnanski, I., and Fiedler, H. E., Jets and Wakes in Tailored Pressure Gradient, The Physics of Fluids, 11, pp. 2512-2523, (1968).

6. Gartshore, I. S., and Newman, B. G., Small Perturbation Jets and Wakes Which Are Approximately Self-Preserving in a Pressure Gradient, C.A.S.I. Transactions, 2, pp. 101-104, (1969).

7. Gartshore, I. S., Two-Dimensional Turbulent Wakes, Journal of Fluid Mechanics, 30, pp. 547-560, (1967).

8. Fekete, G. I., Two-Dimensional, Self-Preserving Turbulent Jets in Streaming Flow, McGill University, Report No. 70-11, (1970).

9. Sabin, C. M., An Analytical and Experimental Study of the Plane, Incompressible, Turbulent Free-Shear Layer With Arbitrary Velocity Ratio and Pressure Gradient, Journal of Basic Engineering, Transactions of the ASME, pp. 421-428, (1965).

10. Brown, G. L., and Rebollo, M. R., A Small, Fast-Response Probe to Measure Composition of a Binary Gas Mixture, AIAA Journal, 10, pp. 649-652, (1972).

11. Schetz, J. A., Free Turbulent Mixing in a Co-Flowing Stream, NASA Langley Working Conference on Free Turbulent Shear Flows, (1972).

12. Clauser, F. H., The Turbulent Boundary Layer, Advances in Applied Mechanics, 4, (1956).

REFERENCES (cont'd.)

13. Zakkay, V., Sinha, R., and Nomura, S., Prediction and Evaluation of Eddy Viscosity Models for Free Mixing, NASA Langley Working Conference on Free Turbulent Shear Flows, (1972).

14. Rudy, D. H., and Bushnell, D. M., Use of Prandtl's Mixing Length Model in Free Turbulent Flow Calculations: A Rational Approach, NASA Langley Working Conference on Free Turbulent Shear Flows, (1972).

15. Morgenthaler, J. H., and Zelazny, S. W., Predictions of Axisymmetric Free Turbulent Shear Flows Using a Generalized Eddy Viscosity Approach, NASA Langley Working Conference on Free Turbulent Shear Flows, (1972).

16. Launder, B. E., Morse, A., Rodi, W., and Spalding, D. B., The Prediction of Free Shear Flows - A Comparison of the Performance of Six Turbulence Models, NASA Langley Working Conference on Free Turbulent Shear Flows, (1972).

17. Peters, C. E., and Phares, W. J., An Integral Turbulent Kinetic Energy Analysis of Free Shear Flows, NASA Langley Working Conference on Free Turbulent Shear Flows, (1972).

18. Bradshaw, P., Ferriss, D., and Atwell, N., Calculation of Boundary Layer Development Using the Turbulent Energy Equation, Journal of Fluid Mechanics, 28, pp. 593-616, (1967).

19. Harsha, P. T., Prediction of Free Turbulent Mixing Using a Turbulent Kinetic Energy Method, NASA Langley Working Conference on Free Turbulent Shear Flows, (1972).

20. Morel, T., Torda, T. Paul, and Bradshaw, P., Turbulent Kinetic Energy Equation and Free Mixing, NASA Langley Working Conference on Free Turbulent Shear Flows (1972).

21. Patankov, S. V., and Spalding, D. B., A Finite-Difference Procedure for Solving the Equations of the Two-Dimensional Boundary Layer,International Journal of Heat and Mass Transfer, 10, pp. 1389-1411, (1967).

22. Ortwerth, P. J., Mechanism of Mixing of Two Nonreacting Gases, AIAA Paper, No. 71-725, (1971).

23. Görtler, H., Berechnung von Aufgaben der freien Turbulenz auf Grund eines neuen Näherungsausatzes, ZAMM, 22, pp. 244-254, (1942).

REFERENCES (cont'd.)

24. Way, J., and Libby, P. A., Application of Hot-Wire Anemometry and Digital Techniques to Measurements in a Turbulent Helium Jet, AIAA Journal, 9, pp. 1567-1573, (1971).

25. Liepmann, H. W., and Laufer, J., Investigation of Free Turbulent Mixing, NACA Technical Note 1257, (1949).

26. Spencer, B. W., and Jones, B. G., Statistical Investigation of Pressure and Velocity Fields in the Turbulent Two-Streams Mixing Layer, AIAA Paper, No. 71-613, (1971).

27. Miles, J. B., and Shih, J., Similarity Parameter for Two-Stream Turbulent Jet-Mixing Region, AIAA Journal, 6, pp. 1429-1430, (1968).

28. Landau, L. D., and Lifshitz, E. M., Fluid Mechanics, Pergamon Press, pp. 102-144, (1959).

29. Davey, R. F., An Experimental Investigation of the Effects of a Density Gradient on Shear Layer Instability, Ph. D. Thesis, California Institute of Technoloyg, (1971).

	$\alpha < 0$ ρU^2 traverse	$\alpha < 0$ ρ traverse	$\rho_1 U_1^2 = \rho_2 U_2^2$ $\alpha = 0$ ρU^2 traverse	$\rho_1 U_1^2 = \rho_2 U_2^2$ $\alpha = 0$ ρ traverse	
U_{20}	408 cm/sec	379 cm/sec	383 cm/sec	376 cm/sec	Tank pressure 4 atm
U_{10}	1080 cm/sec	1000 cm/sec	1010 cm/sec	995 cm/sec	
U_{20}	392 cm/sec	393 cm/sec	- - - -	- - - -	Tank pressure 7 atm
U_{10}	1040 cm/sec	1040 cm/sec	- - - -	- - - -	
U_{20}	376 cm/sec	370 cm/sec	- - - -	- - - -	Tank pressure 2 atm
U_{10}	1000 cm/sec	975 cm/sec	- - - -	- - - -	

$$\mathrm{Re}^* \ \mathrm{cm}^{-1} = \frac{\rho U}{\mu}$$

Tank pressure 7 atm $\begin{cases} \mathrm{Re}^*_{He} = 6 \times 10^3 \ \mathrm{cm}^{-1} \\ \mathrm{Re}^*_{N_2} = 2 \times 10^4 \ \mathrm{cm}^{-1} \end{cases}$

Table I. Summary of flow conditions for experiments
U_{10} Helium velocity at the exit of the nozzle
U_{20} Nitrogen velocity at the exit of the nozzle

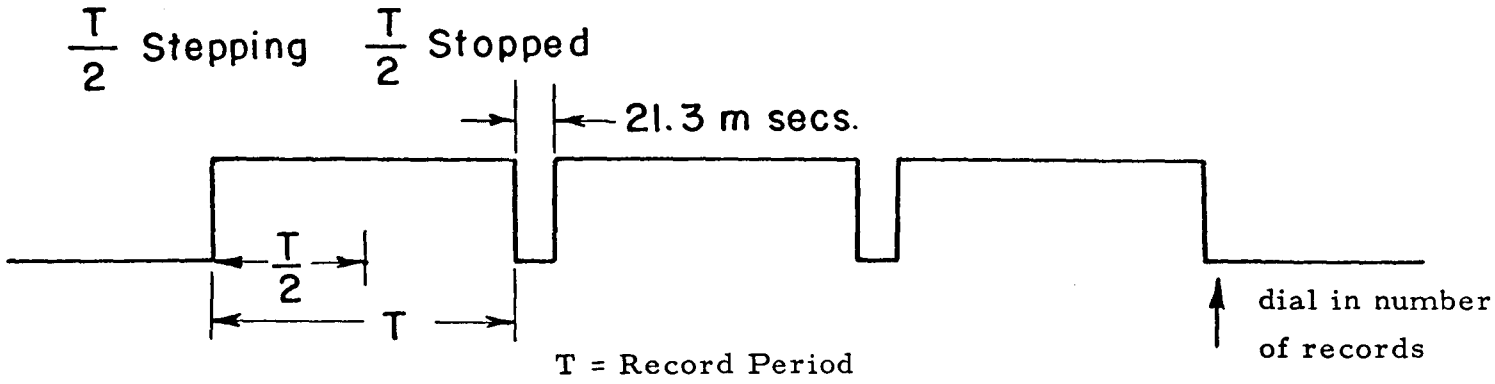

30,000 bytes/second (1 byte/word)

Samples per data point	Words/Record		÷ 64	Half of Column 4 pulses	No. of data points or No. of records	Distance traveled in T/2 seconds	Record time	Total time seconds	Total Distance
512	1K	1024	16	8	125	.008"	.034	4.250	1.000"
1024	2K	2048	32	16	62	.016"	.069	4.278	.992"
2048	4K	4096	64	32	31	.032"	.141	4.371	.992"
4096	8K	8192	128	64	16	.064"	.273	4.368	1.024"
8192	16K	16384	256	128	8	.128"	.546	4.368	1.024"
16384	32K	32768	512	256	4	.256"	1.092	4.368	1.024"

Table II. Aspirating probe traverse; different possibilities with the Data Slicer

$$\alpha = \frac{x}{U_1}\frac{dU_1}{dx}$$

		$\alpha = 0$	$\alpha = -0.18$
	$\frac{\delta_1}{(x - x_o)}$	.10	.16
$\frac{\delta}{(x - x_o)}$	Exp. Data	.25	.40
	Photos	.24	.39
	$\left(\frac{U}{U_1}\right)_{\eta_o}$	.70	.59
	$\left(\frac{\rho U^2}{\rho_1 U_1^2}\right)_{\eta_o}$	.87	.60
	$\left(\frac{\rho}{\rho_1}\right)_{\eta_o}$	1.78	1.70
	$\left(\frac{\rho U^2}{\rho_1 U_1^2}\right)_{min}$	.52	.32
	$\left(\frac{\rho U^2}{\rho_1 U_1^2}\right)_{max}$	1.22	1.20
	$\left(\frac{\sqrt{\overline{\rho'^2}}}{(\rho_2 - \rho_1)}\right)_{max}$	.19	.20
	$\left(\frac{\overline{\rho u' v'}}{\rho_1 U_1^2}\right)_{max}$	.012	.0205
	$\left(\frac{\overline{\rho' v'}}{\rho_1 U_1}\right)_{max}$	.068	.082
	$\frac{\nu_t}{\Delta U(x - x_o)}$	.0016	.0040
	$\frac{\mathfrak{D}_t}{\Delta U(x - x_o)}$	.010	.012
	Sc_t	.16	.33

Table III. Effect of adverse pressure gradient on shear layer parameters

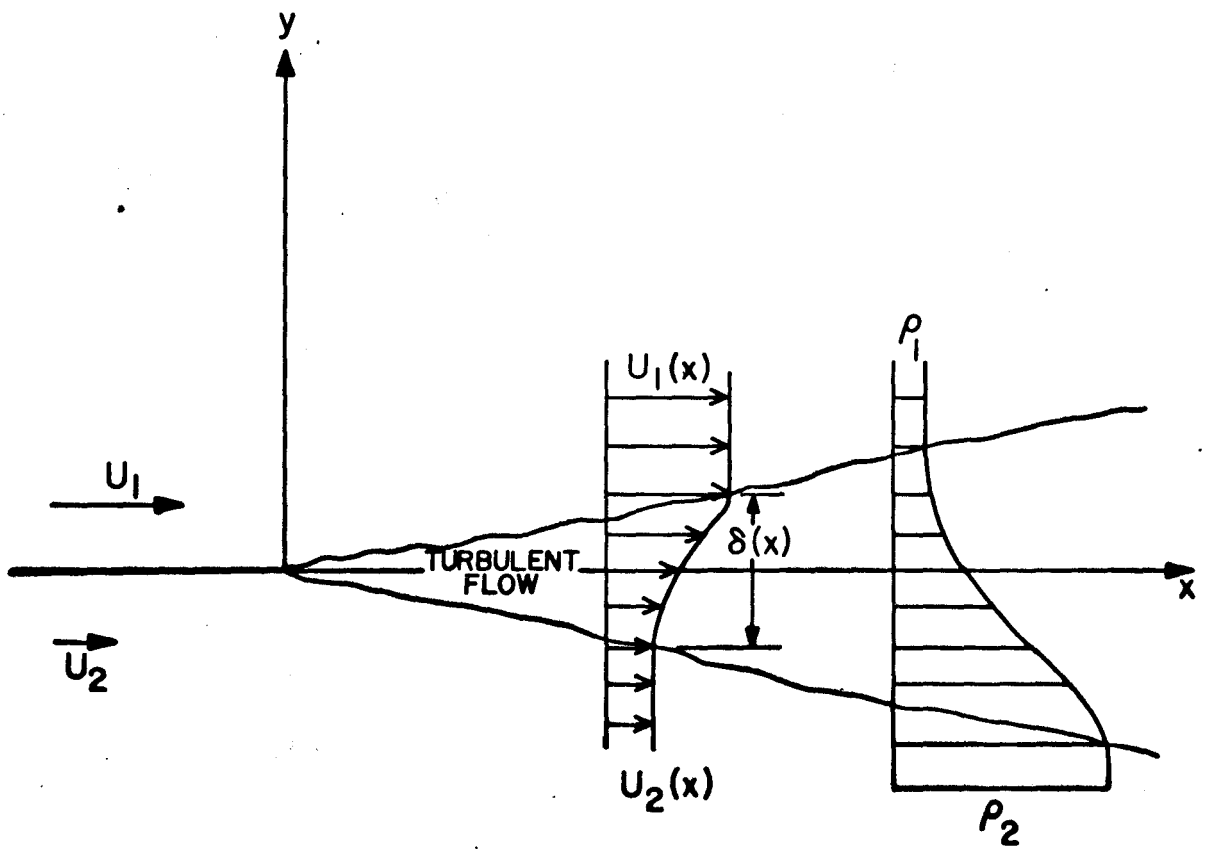

Figure 1. Mixing layer model.

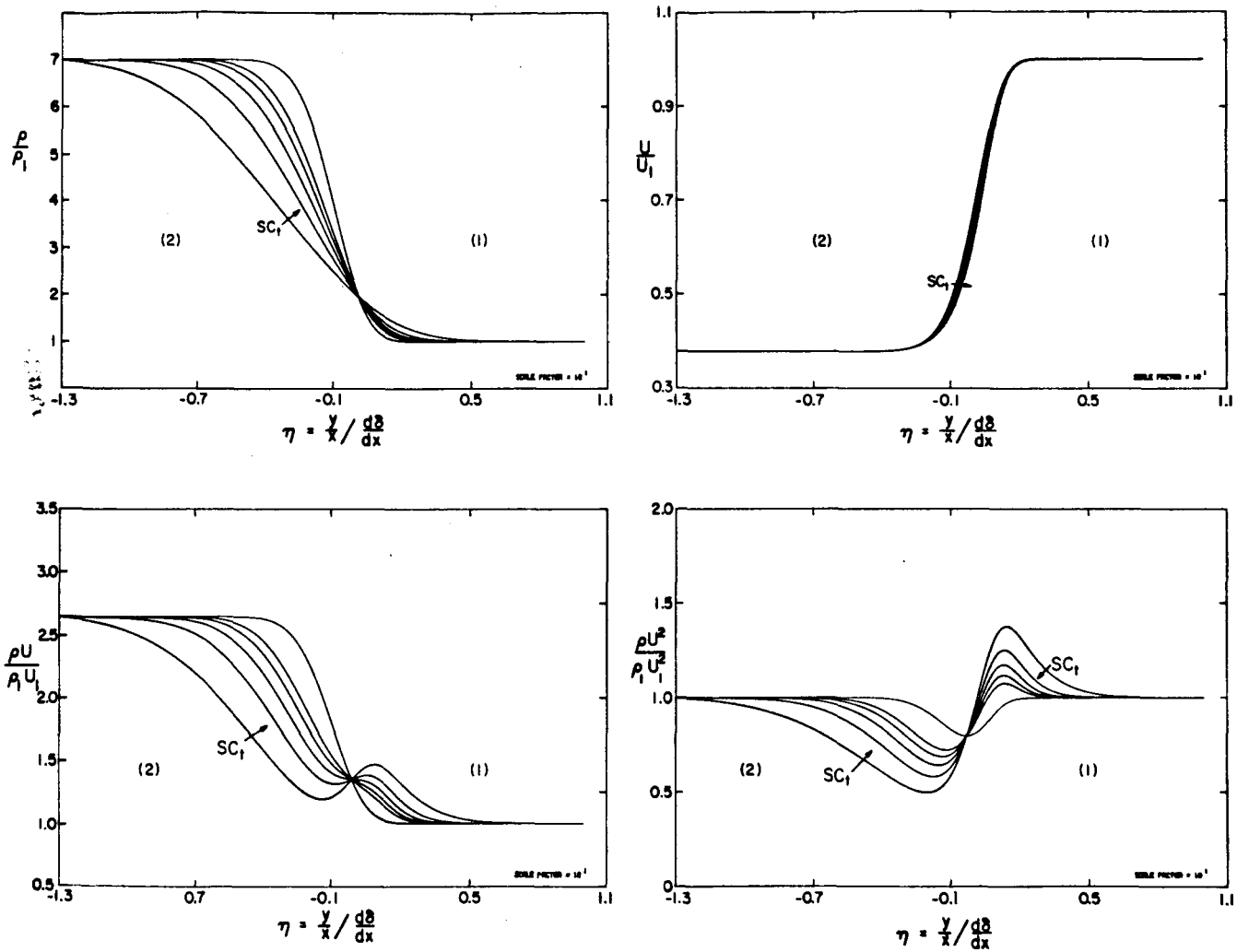

Figure 2. Numerical solution for $\alpha = 0$ ($\rho_1 U_1^2 = \rho_2 U_2^2$ case) $Sc_t = 0.1, 0.2, 0.3, 0.4, 0.5, 1.0$.

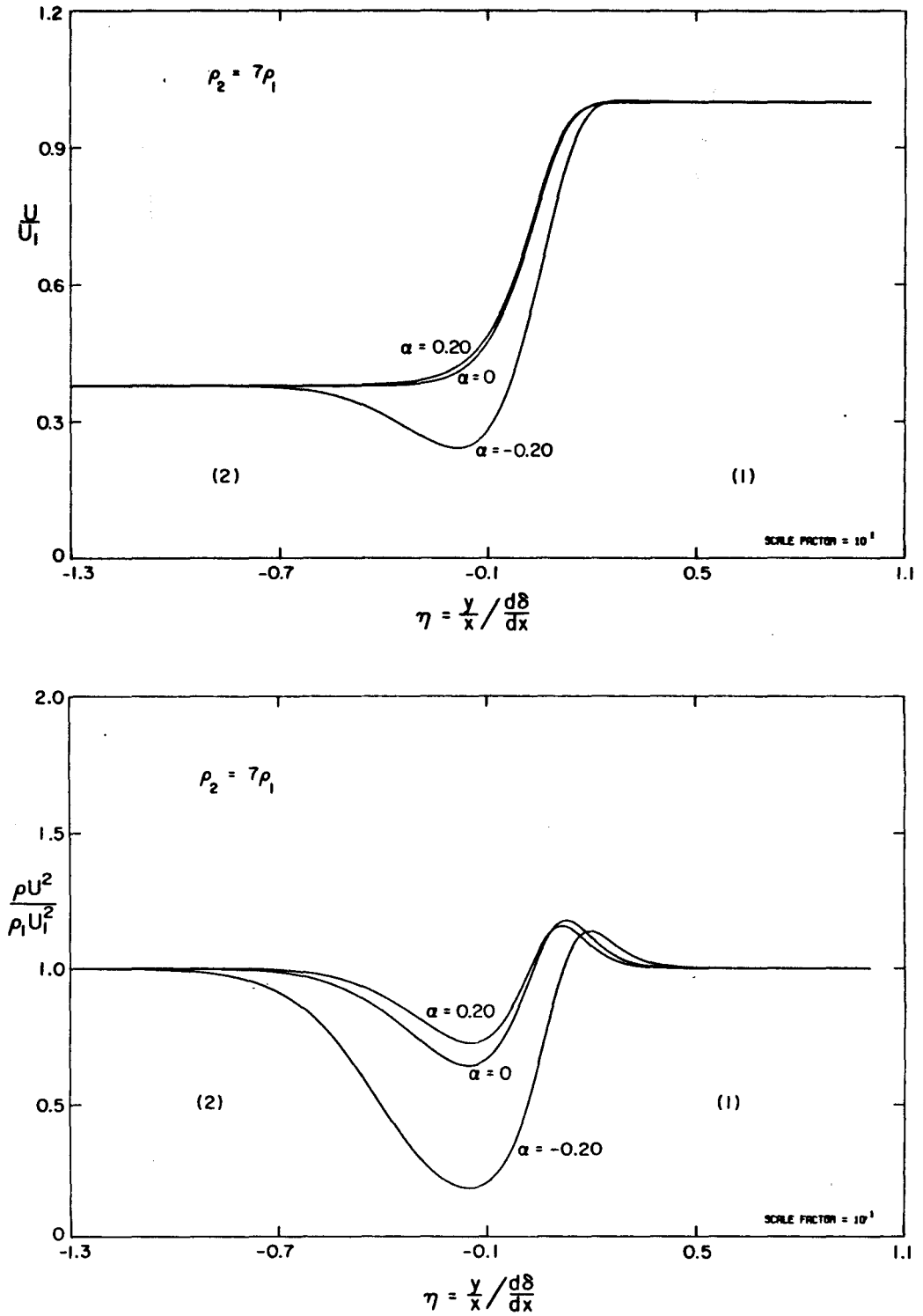

Figure 3. Comparison of numerical solutions for favorable and adverse pressure gradients for $Sc_t = 0.30$.

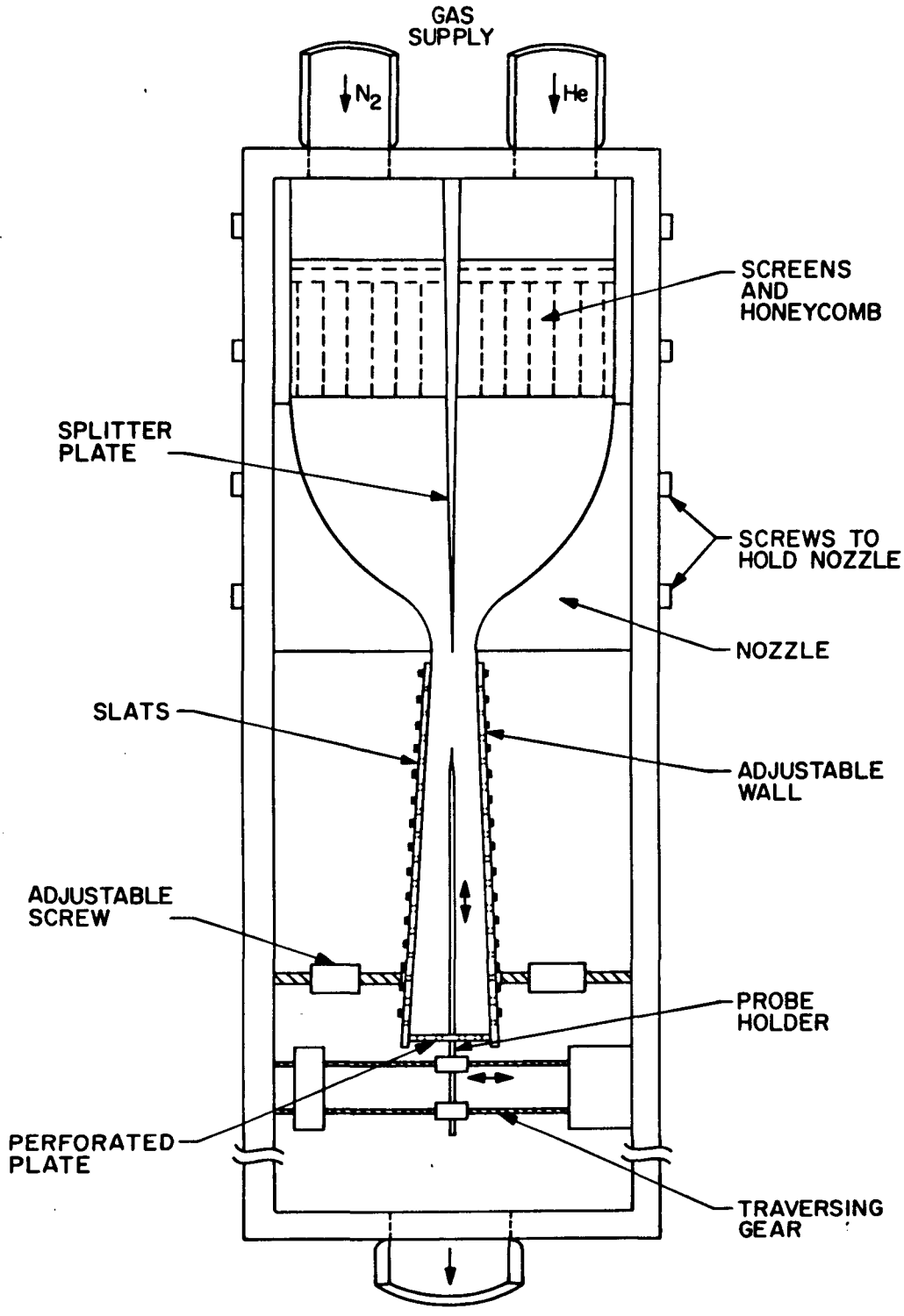

Figure 4. Sketch of the test section.

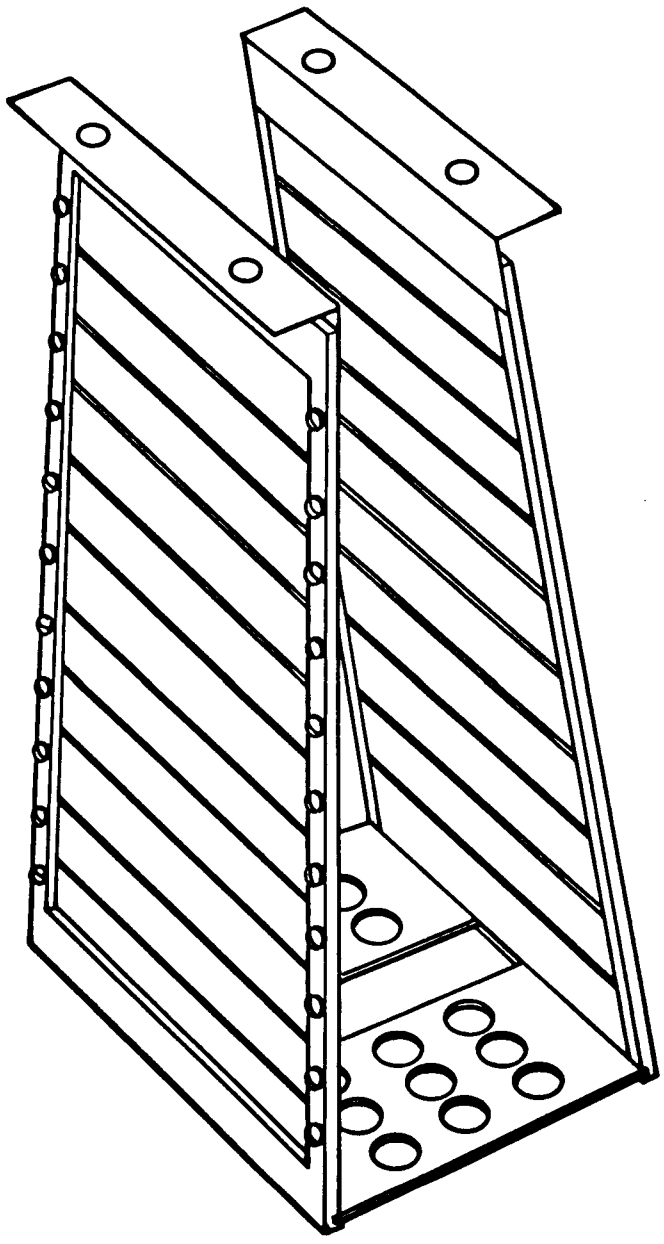

Figure 5. Adjustable slats and perforated plate.

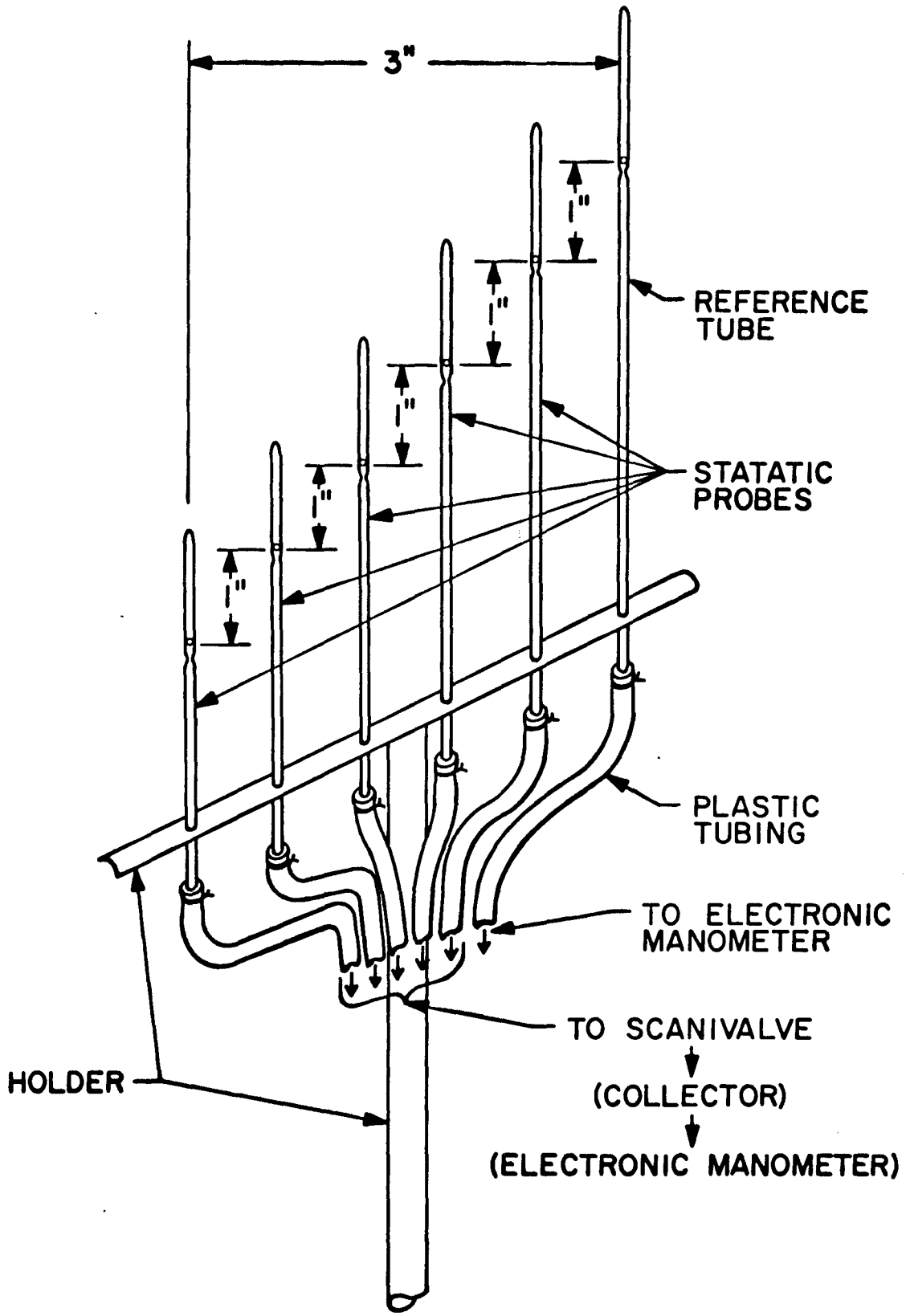

Figure 6. Array of static pressure tubes.

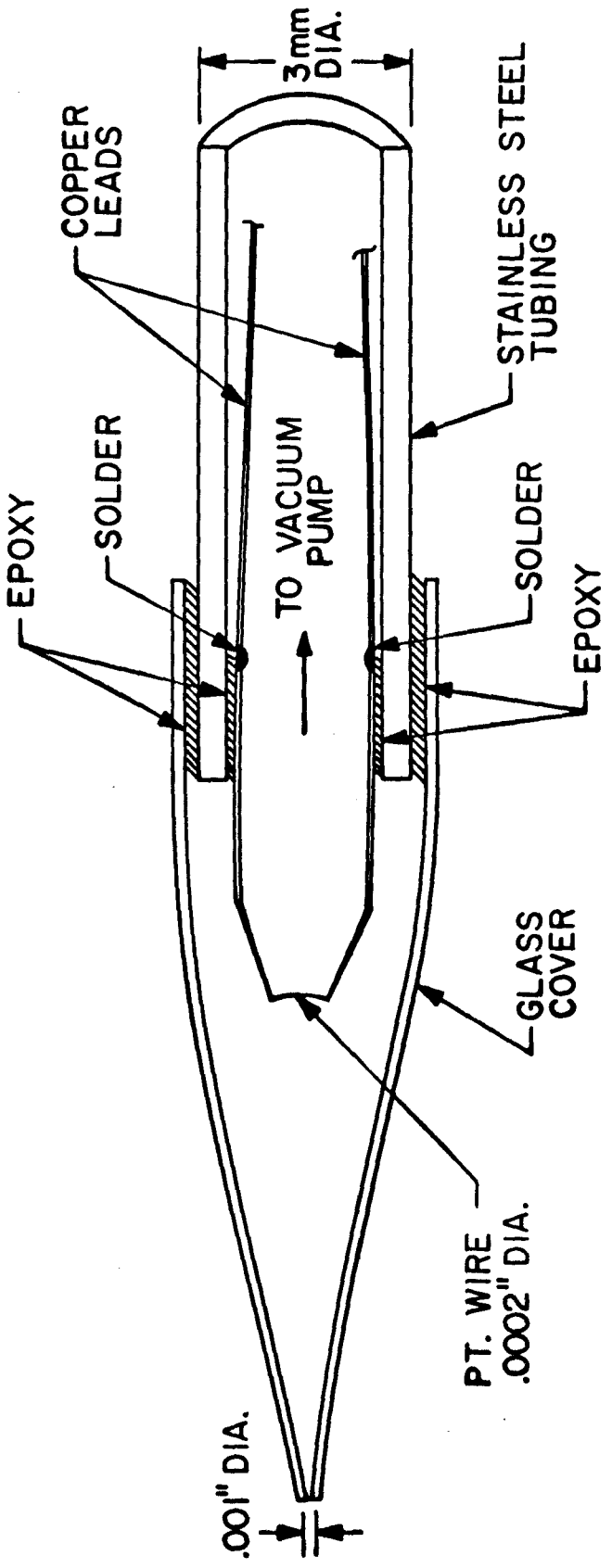

Figure 7. Sketch of the new probe.

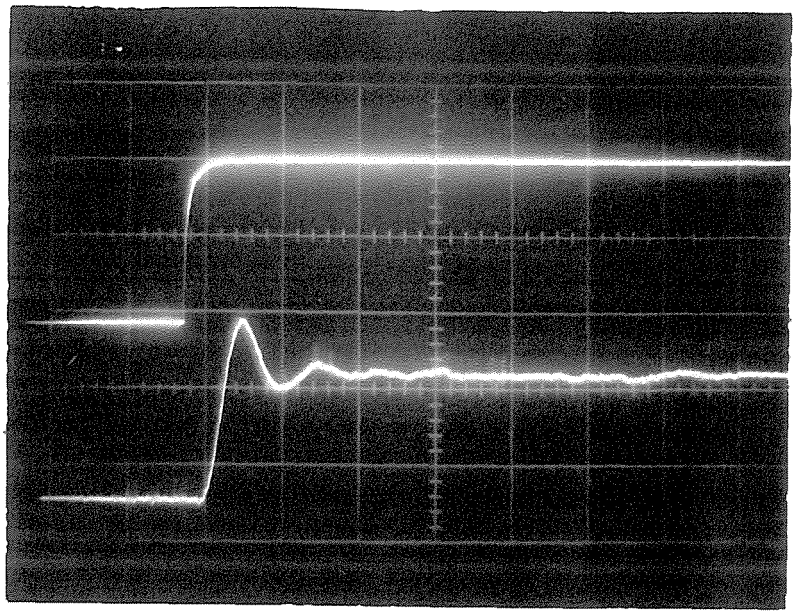

Figure 8. Apparatus rise time: oscilloscope photo of the response of a hot wire and pitot tube to starting process. Horizontal scale: 100 msec/div; Vertical scale 1 volt/div. Tank pressure = 7 atm.

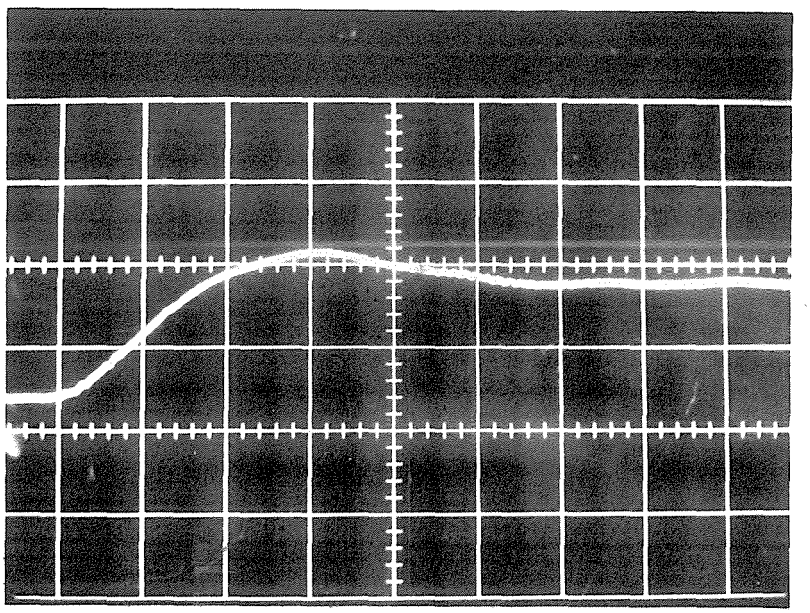

Figure 9. Time response of the pitot tube and Scanivalve. Horizontal scale: 20 msec/div; Vertical scale: .5 volt/div. Tank pressure = 6 atm.

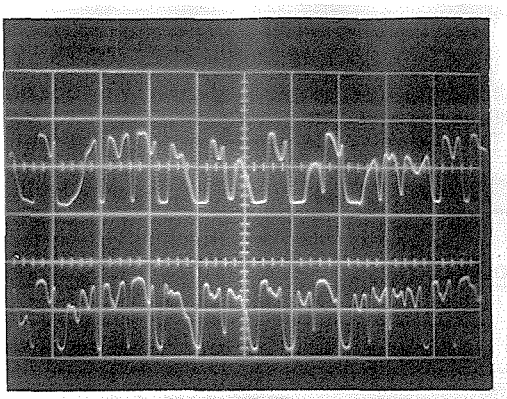

HORIZONTAL SCALE : 5 MSEC/DIV.
VERTICAL SCALE : 1 VOLT/DIV.
X = 1.35 IN.

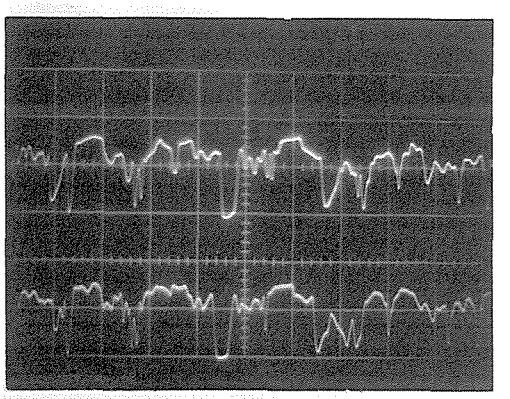

HORIZONTAL SCALE : 5 MSEC/DIV.
VERTICAL SCALE : 1 VOLT/DIV.
X = 3.00 IN.

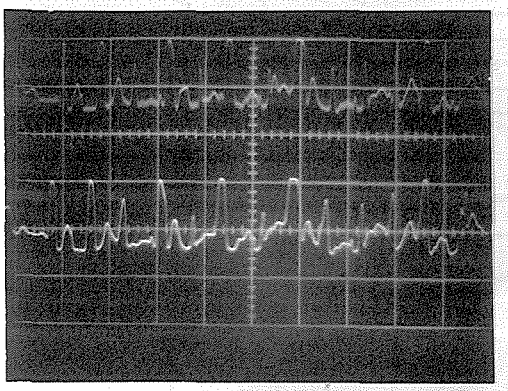

HORIZONTAL SCALE : 5 MSEC/DIV.
VERTICAL SCALE : 1 VOLT/DIV.
X = 2.00 IN.

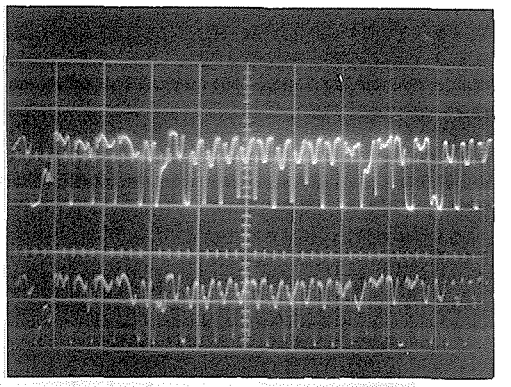

HORIZONTAL SCALE : 10 MSEC/DIV.
VERTICAL SCALE : 1 VOLT/DIV.
X = 2.00 IN.

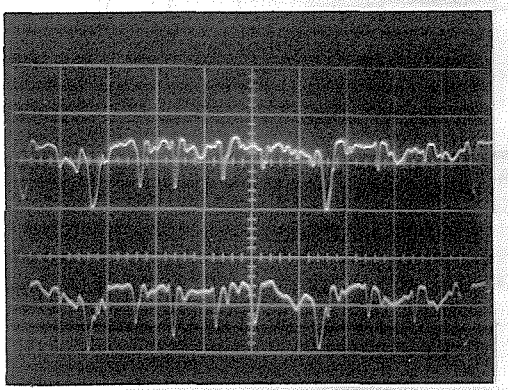

HORIZONTAL SCALE : 5 MSEC/DIV.
VERTICAL SCALE : 1 VOLT/DIV.
X = 4.00 IN.

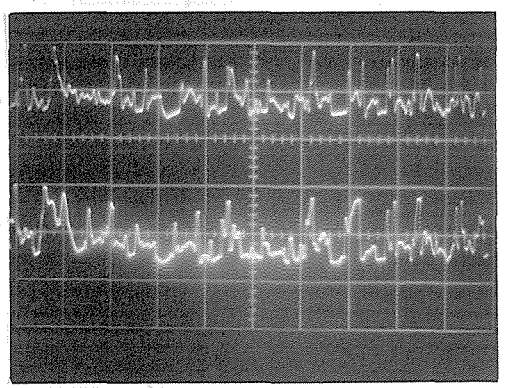

HORIZONTAL SCALE : 10 MSEC/DIV.
VERTICAL SCALE : 1 VOLT/DIV.
X = 4.00 IN.

Figure 10. Two-dimensionality test: oscilloscope photos of the response of two hot wires 2" apart aligned spanwise at several downstream locations. Tank pressure = 3 atm.

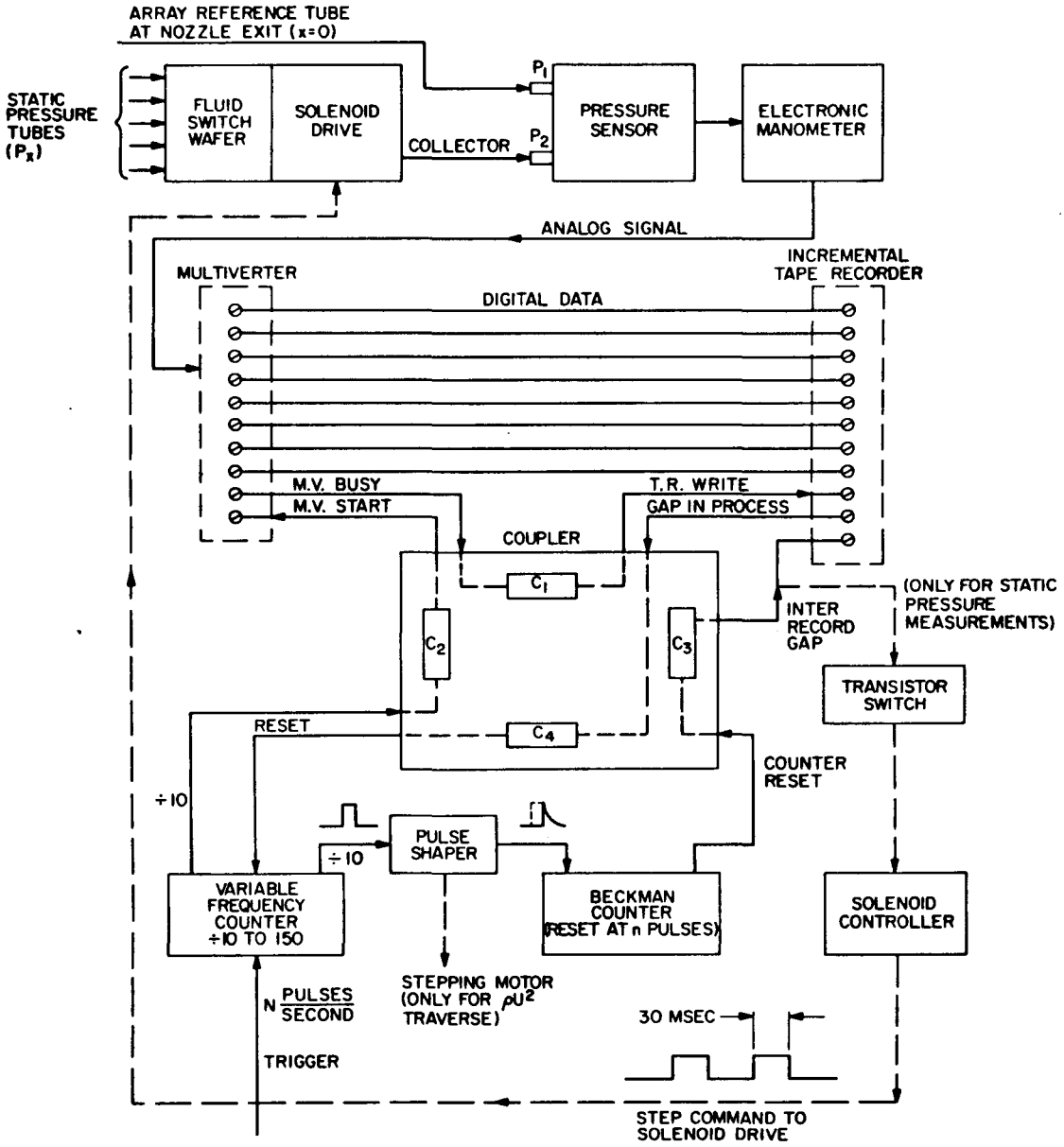

Figure 11. Block diagram of the set up to write pressure data on tape.

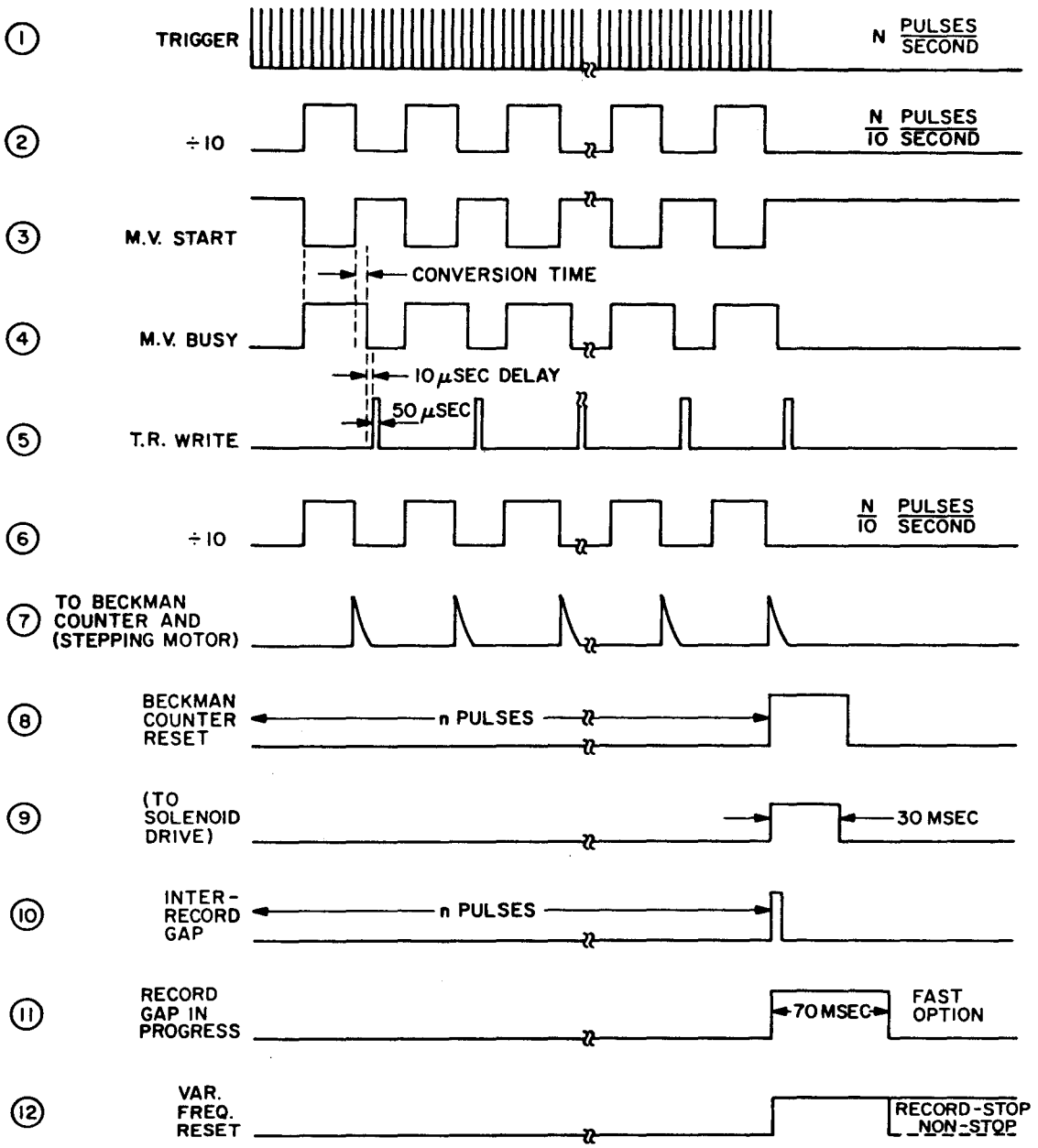

Figure 12. Timing of operation to write pressure data on tape.

Figure 13. Photographic comparison of mixing layers for $\alpha < 0$ and $\alpha = 0$. Lower (U_{20} = 393 cm/sec) stream is N_2; upper (U_{10} = 1040 cm/sec) stream is He. Tank pressure = 4 atm.

See figure on next page

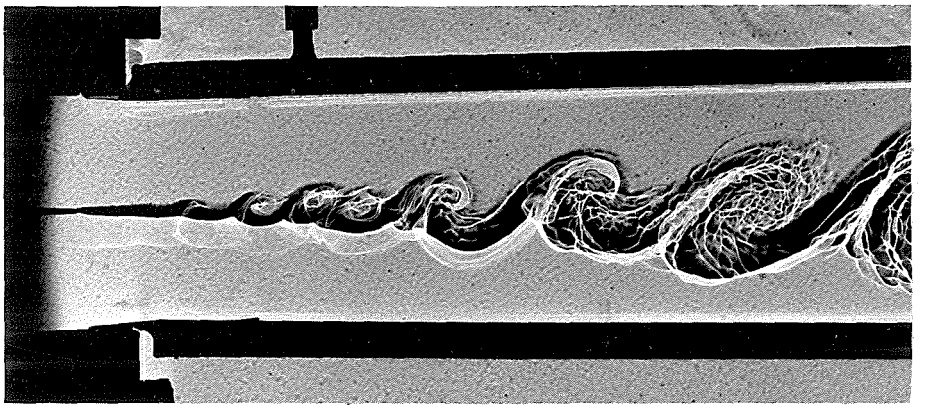

$\alpha = 0$

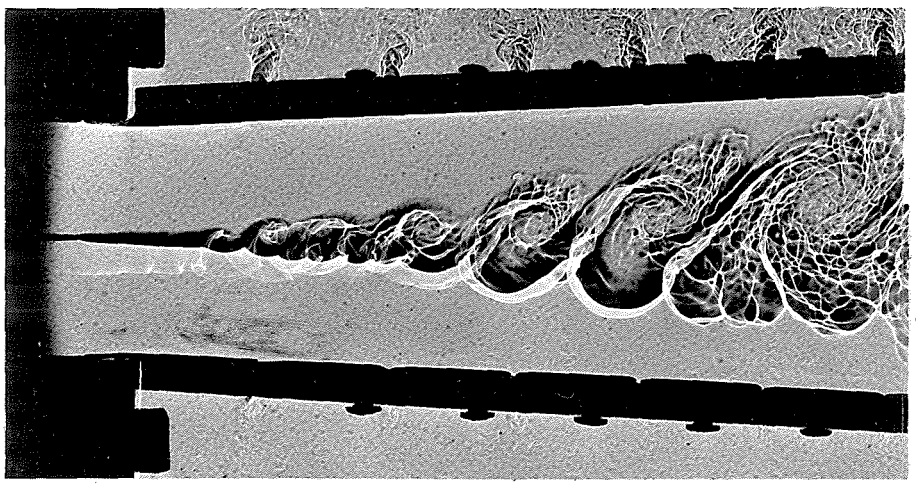

$\alpha < 0$

Figure 14. Shadowgraphs of mixing layer for $\alpha = 0$ at different Reynolds numbers. ($\rho_1 U_1^2 = \rho_2 U_2^2$ case.) Lower (low speed) stream is N_2; upper (high speed) stream is He.

See figure on next page

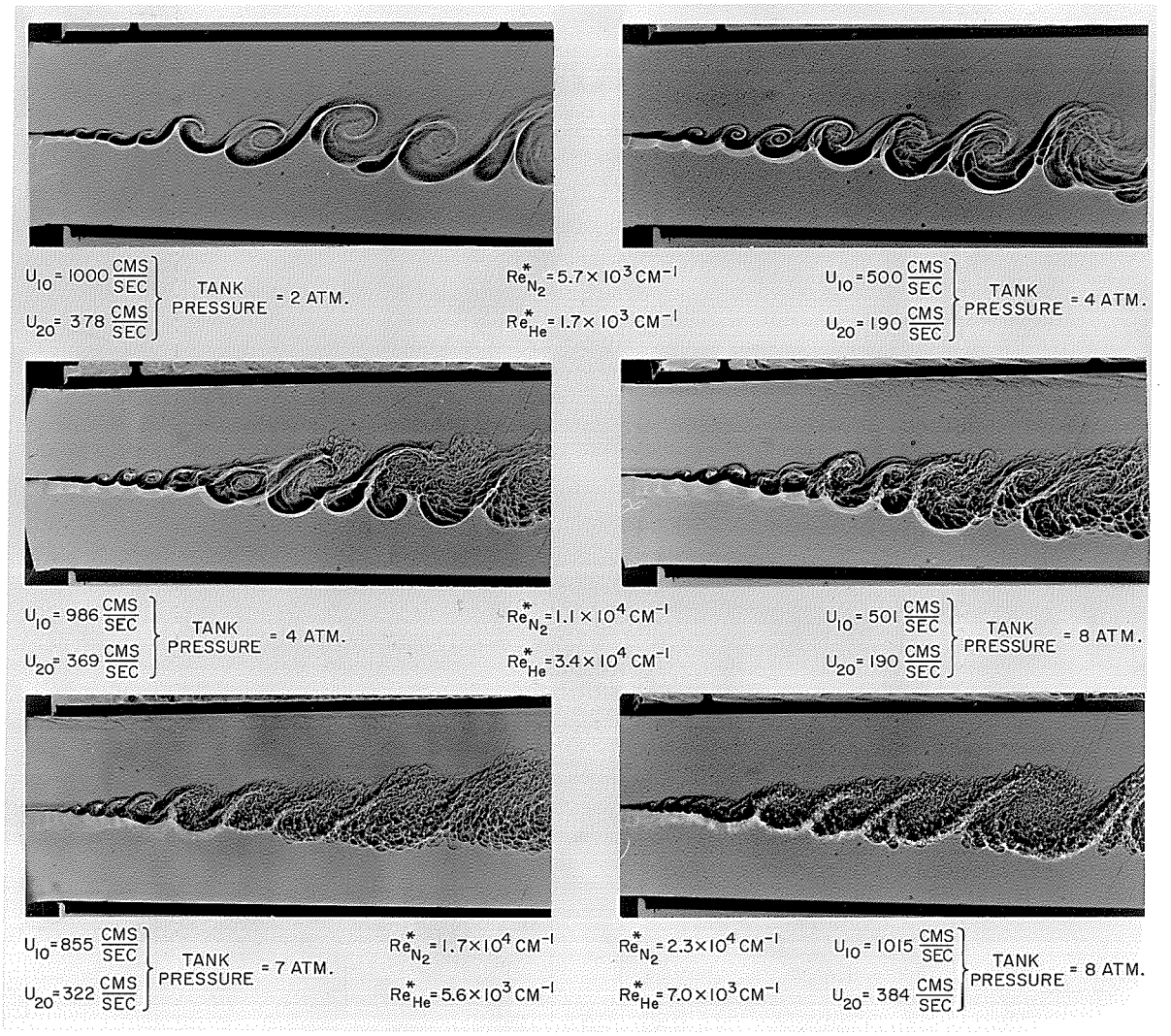
$U_{10} = 1000 \frac{CMS}{SEC}$
$U_{20} = 378 \frac{CMS}{SEC}$
TANK PRESSURE = 2 ATM.
$Re^*_{N_2} = 5.7 \times 10^3 CM^{-1}$
$Re^*_{He} = 1.7 \times 10^3 CM^{-1}$
$U_{10} = 500 \frac{CMS}{SEC}$
$U_{20} = 190 \frac{CMS}{SEC}$
TANK PRESSURE = 4 ATM.
$U_{10} = 986 \frac{CMS}{SEC}$
$U_{20} = 369 \frac{CMS}{SEC}$
TANK PRESSURE = 4 ATM.
$Re^*_{N_2} = 1.1 \times 10^4 CM^{-1}$
$Re^*_{He} = 3.4 \times 10^4 CM^{-1}$
$U_{10} = 501 \frac{CMS}{SEC}$
$U_{20} = 190 \frac{CMS}{SEC}$
TANK PRESSURE = 8 ATM.
$U_{10} = 855 \frac{CMS}{SEC}$
$U_{20} = 322 \frac{CMS}{SEC}$
TANK PRESSURE = 7 ATM.
$Re^*_{N_2} = 1.7 \times 10^4 CM^{-1}$
$Re^*_{He} = 5.6 \times 10^3 CM^{-1}$
$Re^*_{N_2} = 2.3 \times 10^4 CM^{-1}$
$Re^*_{He} = 7.0 \times 10^3 CM^{-1}$
$U_{10} = 1015 \frac{CMS}{SEC}$
$U_{20} = 384 \frac{CMS}{SEC}$
TANK PRESSURE = 8 ATM.

Figure 15. Shadowgraphs of mixing layer for $\alpha < 0$ at different Reynolds numbers. Lower (low speed) stream is N_2; upper (high speed) stream is He.

See figure next page

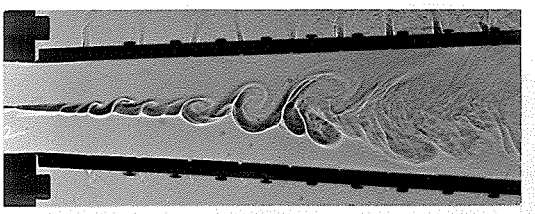

$U_{10} = 1000 \frac{CMS}{SEC}$
$U_{20} = 380 \frac{CMS}{SEC}$
TANK PRESSURE = 2 ATM.

$Re^*_{N_2} = 5.7 \times 10^3 CM^{-1}$
$Re^*_{He} = 1.7 \times 10^3 CM^{-1}$

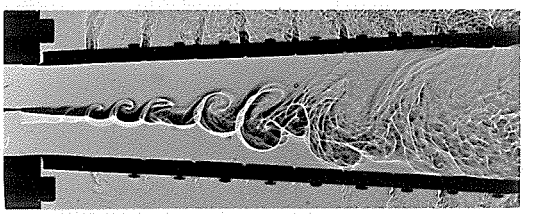

$U_{10} = 503 \frac{CMS}{SEC}$
$U_{20} = 187 \frac{CMS}{SEC}$
TANK PRESSURE = 4 ATM.

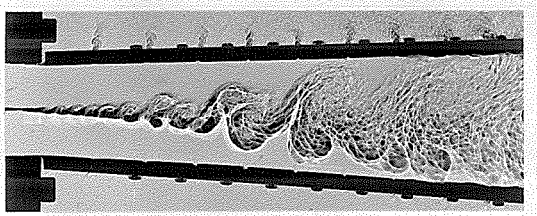

$U_{10} = 1000 \frac{CMS}{SEC}$
$U_{20} = 378 \frac{CMS}{SEC}$
TANK PRESSURE = 4 ATM.

$Re^*_{N_2} = 1.1 \times 10^4 CM^{-1}$
$Re^*_{He} = 3.4 \times 10^3 CM^{-1}$

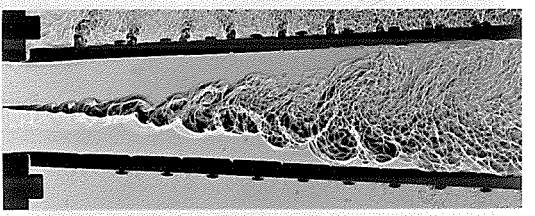

$U_{10} = 501 \frac{CMS}{SEC}$
$U_{20} = 190 \frac{CMS}{SEC}$
TANK PRESSURE = 8 ATM.

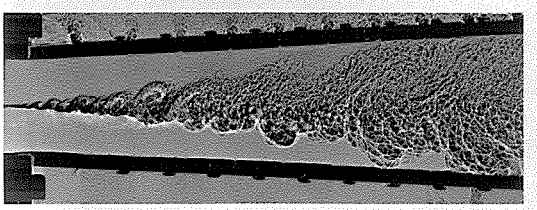

$U_{10} = 1170 \frac{CMS}{SEC}$
$U_{20} = 442 \frac{CMS}{SEC}$
TANK PRESSURE = 7 ATM.

$Re^*_{N_2} = 2.3 \times 10^4 CM^{-1}$
$Re^*_{He} = 7.0 \times 10^3 CM^{-1}$

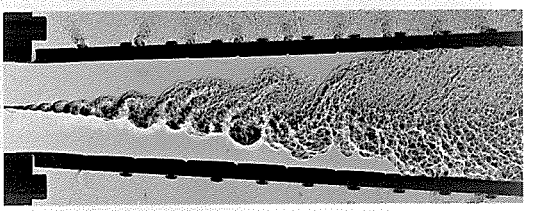

$U_{10} = 1005 \frac{CMS}{SEC}$
$U_{20} = 380 \frac{CMS}{SEC}$
TANK PRESSURE = 8 ATM.

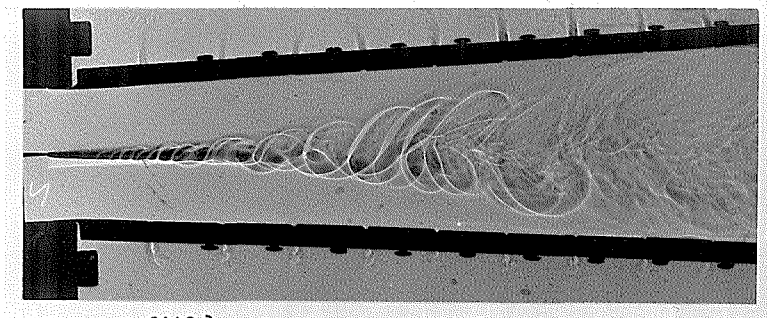

$U_{10} = 1000 \frac{CMS}{SEC}$
$U_{20} = 380 \frac{CMS}{SEC}$
TANK PRESSURE = 2 ATM.

$Re^*_{N_2} = 5.7 \times 10^3 CM^{-1}$
$Re^*_{He} = 1.7 \times 10^3 CM^{-1}$

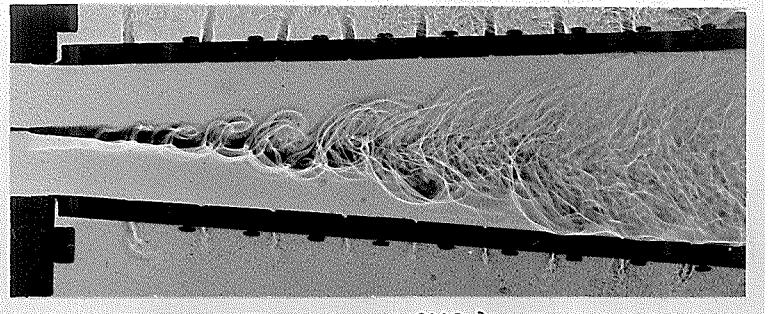

$U_{10} = 503 \frac{CMS}{SEC}$
$U_{20} = 187 \frac{CMS}{SEC}$
TANK PRESSURE = 4 ATM.

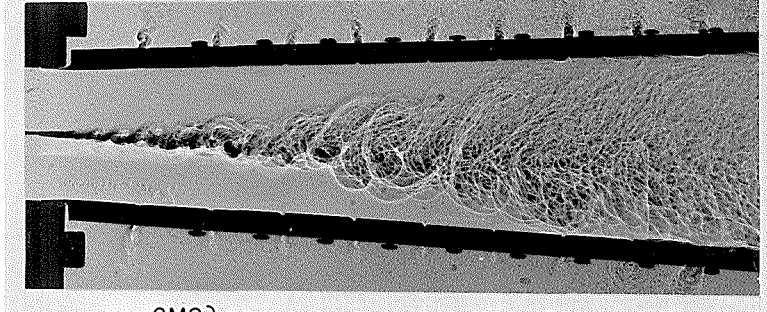

$U_{10} = 1000 \frac{CMS}{SEC}$
$U_{20} = 378 \frac{CMS}{SEC}$
TANK PRESSURE = 4 ATM.

$Re^*_{N_2} = 1.1 \times 10^4 CM^{-1}$
$Re^*_{He} = 3.4 \times 10^3 CM^{-1}$

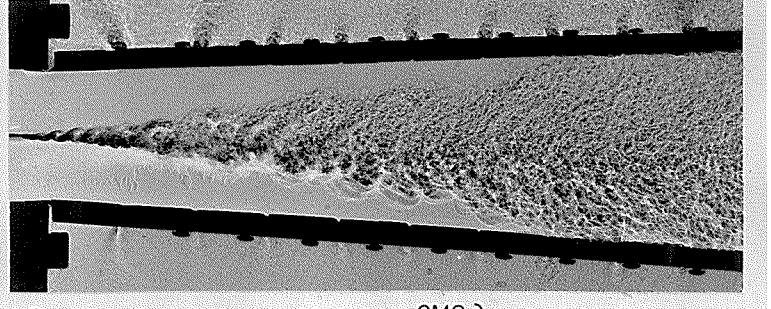

$Re^*_{N_2} = 2.3 \times 10^4 CM^{-1}$
$Re^*_{He} = 7.0 \times 10^3 CM^{-1}$

$U_{10} = 1005 \frac{CMS}{SEC}$
$U_{20} = 380 \frac{CMS}{SEC}$
TANK PRESSURE = 8 ATM.

Figure 16. Multiple exposure shadowgraphs of mixing layer for $\alpha < 0$ at different Reynolds numbers. Lower (low speed) stream is N_2; upper (high speed) stream is He.

see figure next page

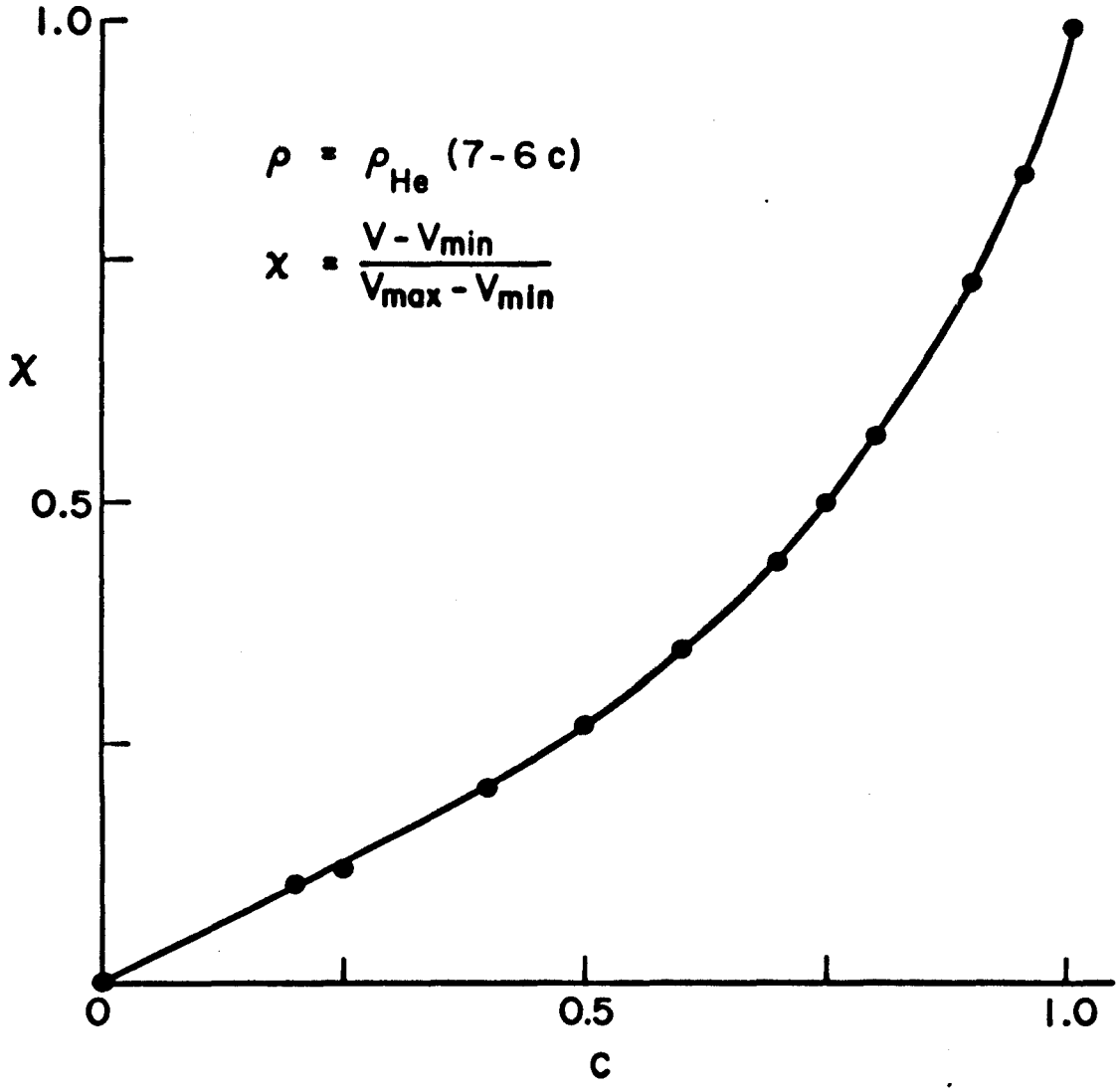

Figure 17. Aspirating probe calibration curve at 4 atm.

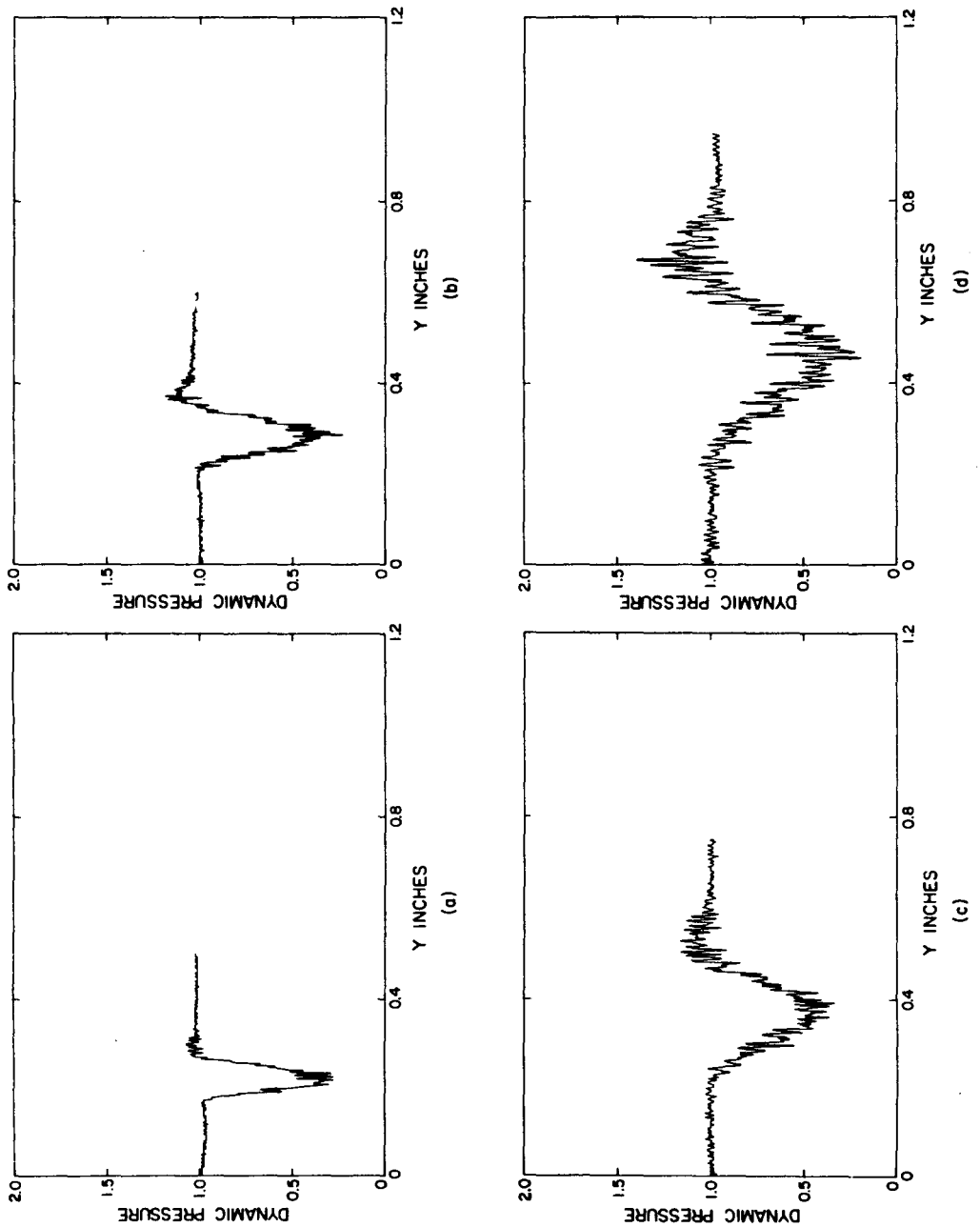

Figure 18. Dynamic pressure traverses at several stations. Tank pressure = 4 atm; $\alpha = -0.18$; (a) x = 0.75"; (b) x = 1.00"; (c) x = 1.50"; (d) x = 2.00".

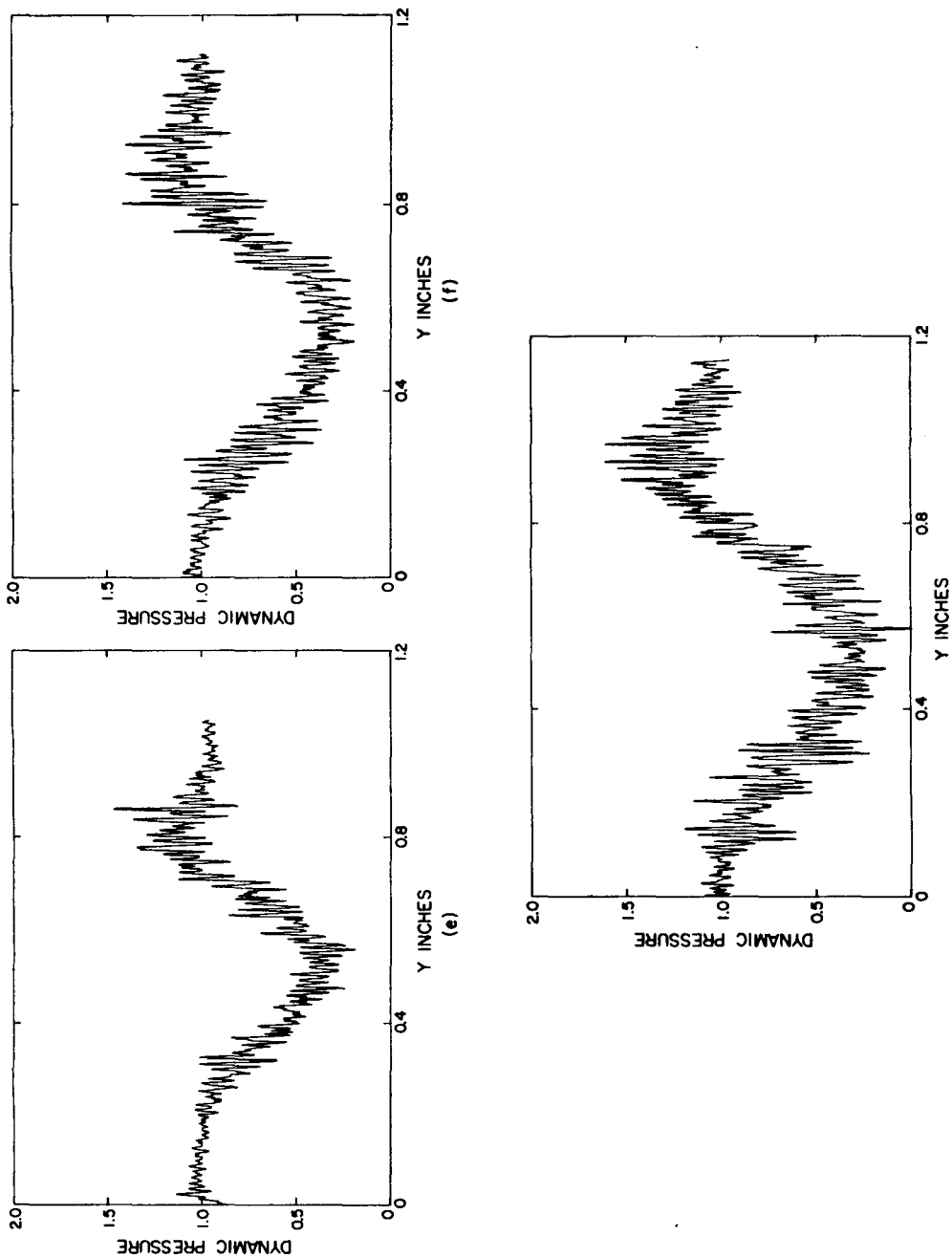

Figure 19. Dynamic pressure traverses at several downstream stations. Tank pressure = 4 atm; α = -0.18; (e) x = 2.50"; (f) x = 3.00"; (g) x = 3.25".

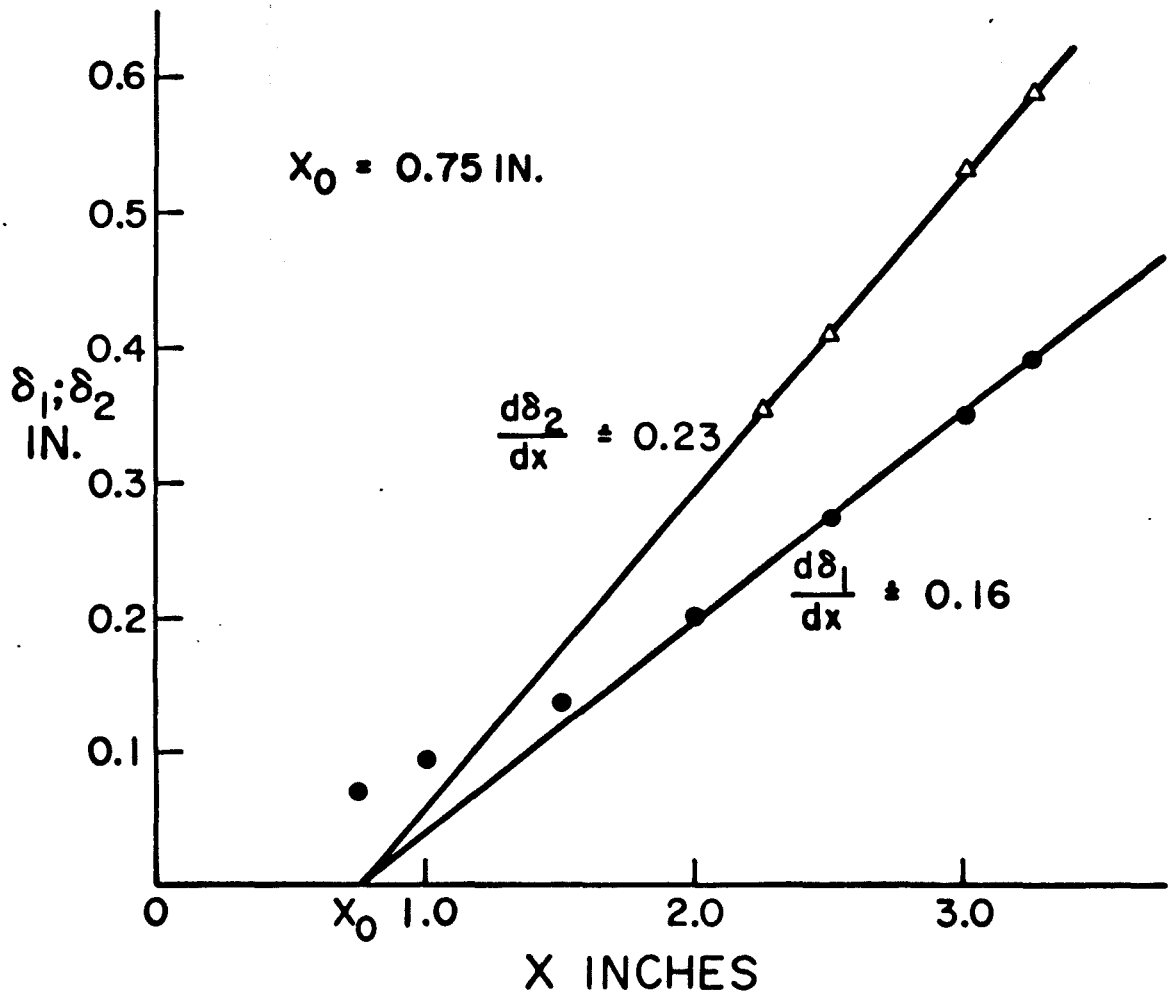

Figure 20. Variation of mixing layer thickness with x coordinate. Tank pressure = 4 atm; α = -0.18.

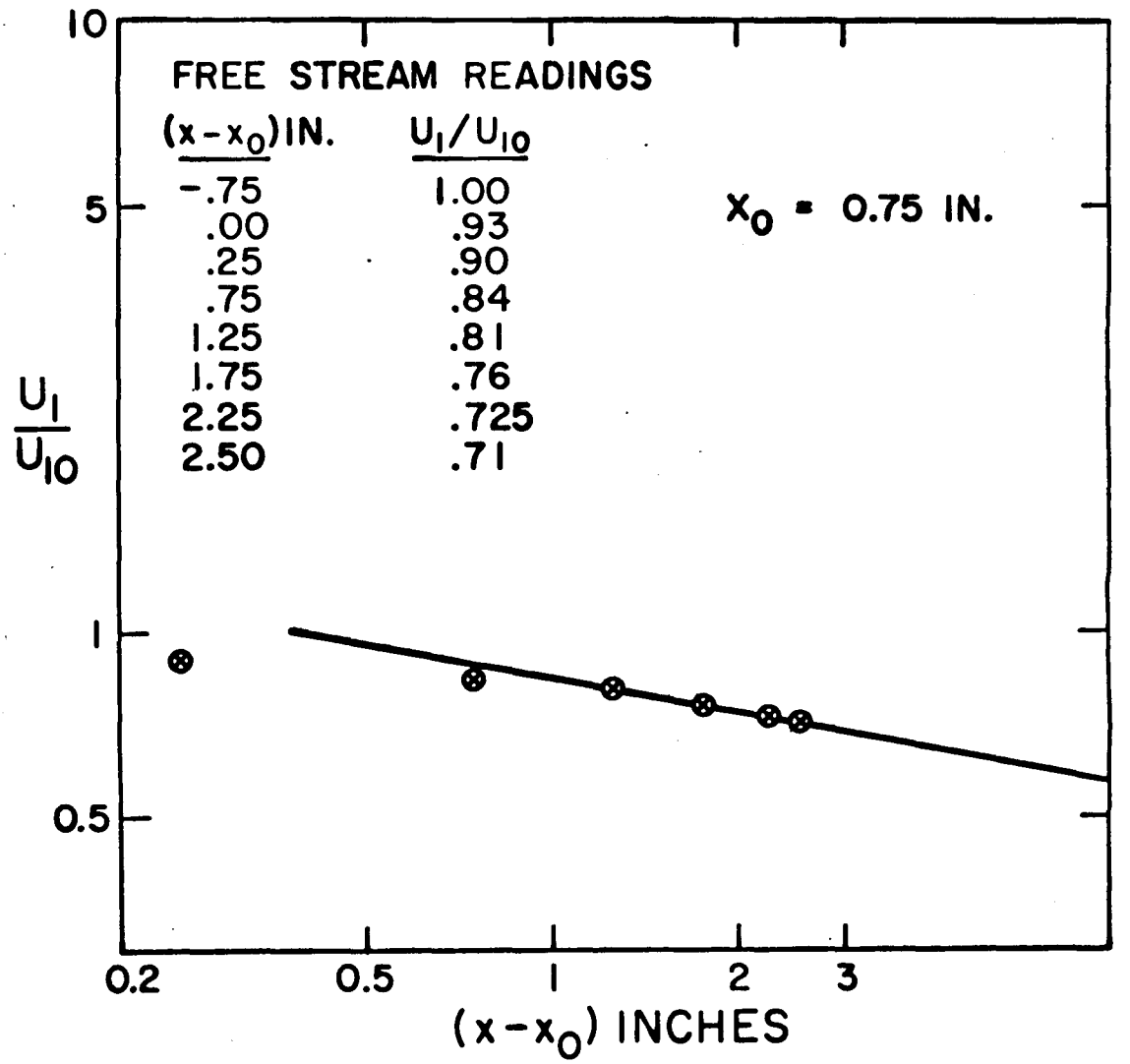

Figure 21. Free stream velocity decay as a function of downstream position. Tank pressure = 4 atm; $\alpha = -0.18$.

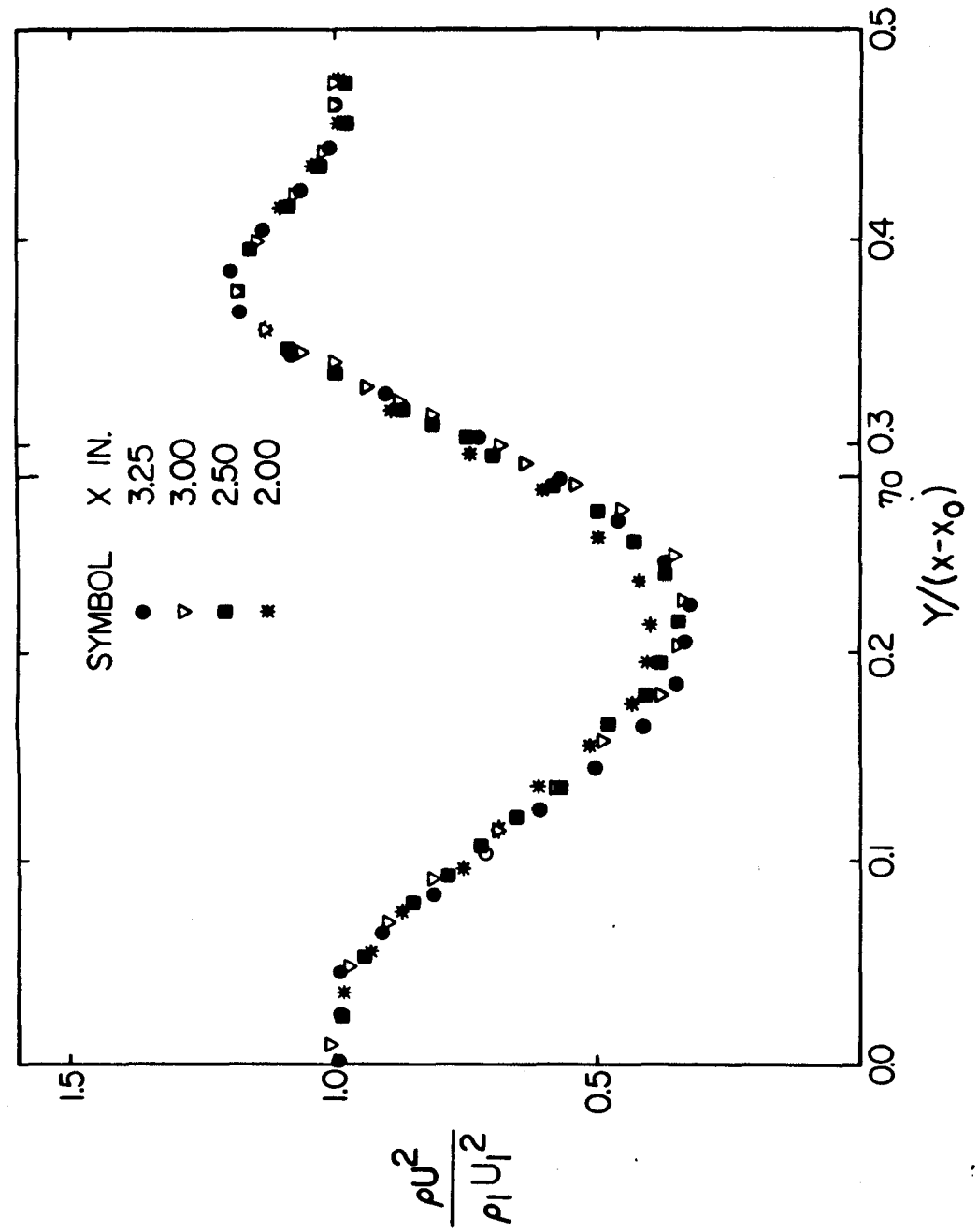

Figure 22. Similarity profile for dynamic pressure. Tank pressure = 4 atm; $\alpha = -0.18$; $x_o = 0.75''$.

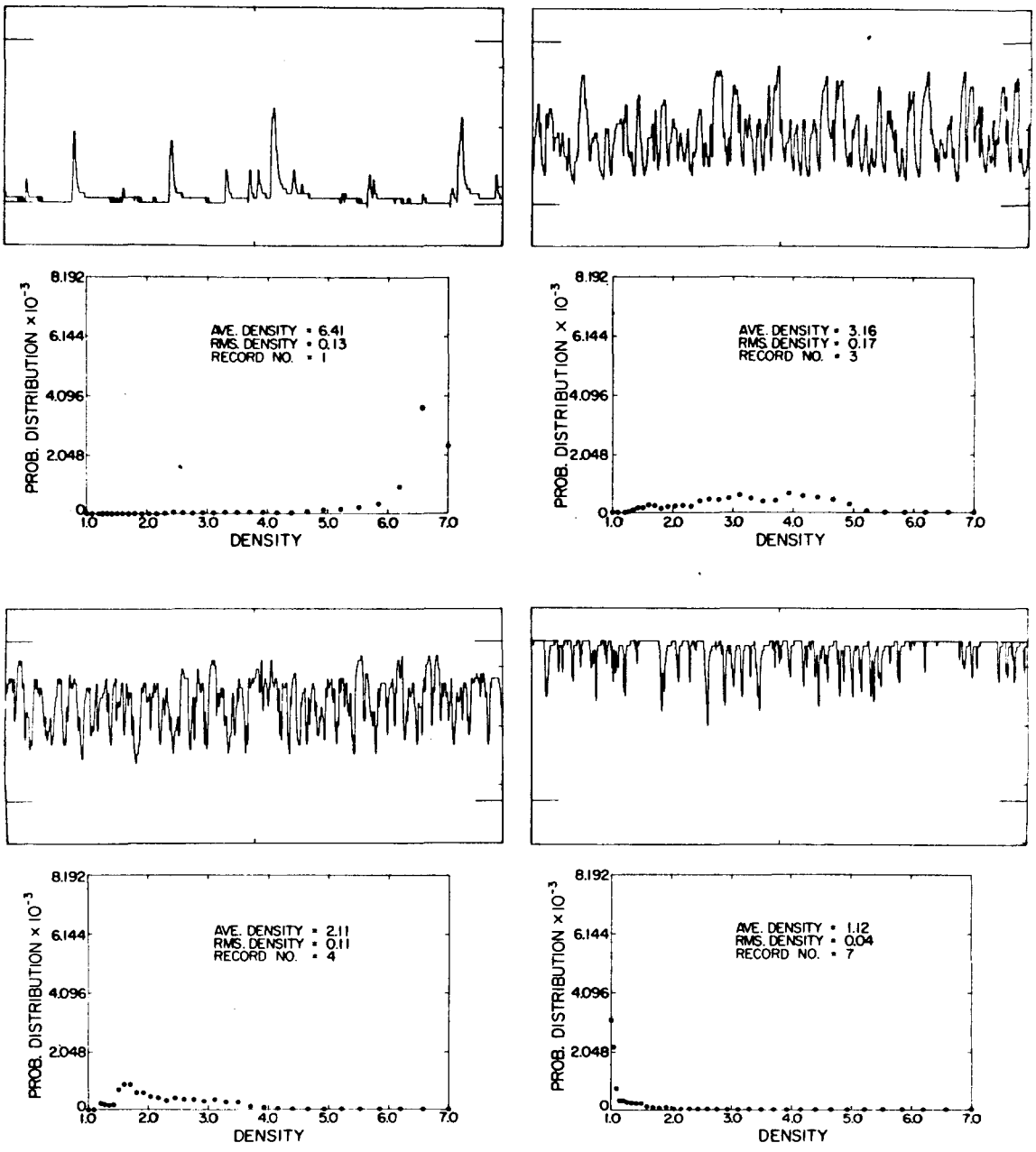

Figure 23. Density traverse; aspirating probe voltage as a function of time, and probability distribution at four data points. Tank pressure = 4 atm; α = -0.18; x = 3.00".

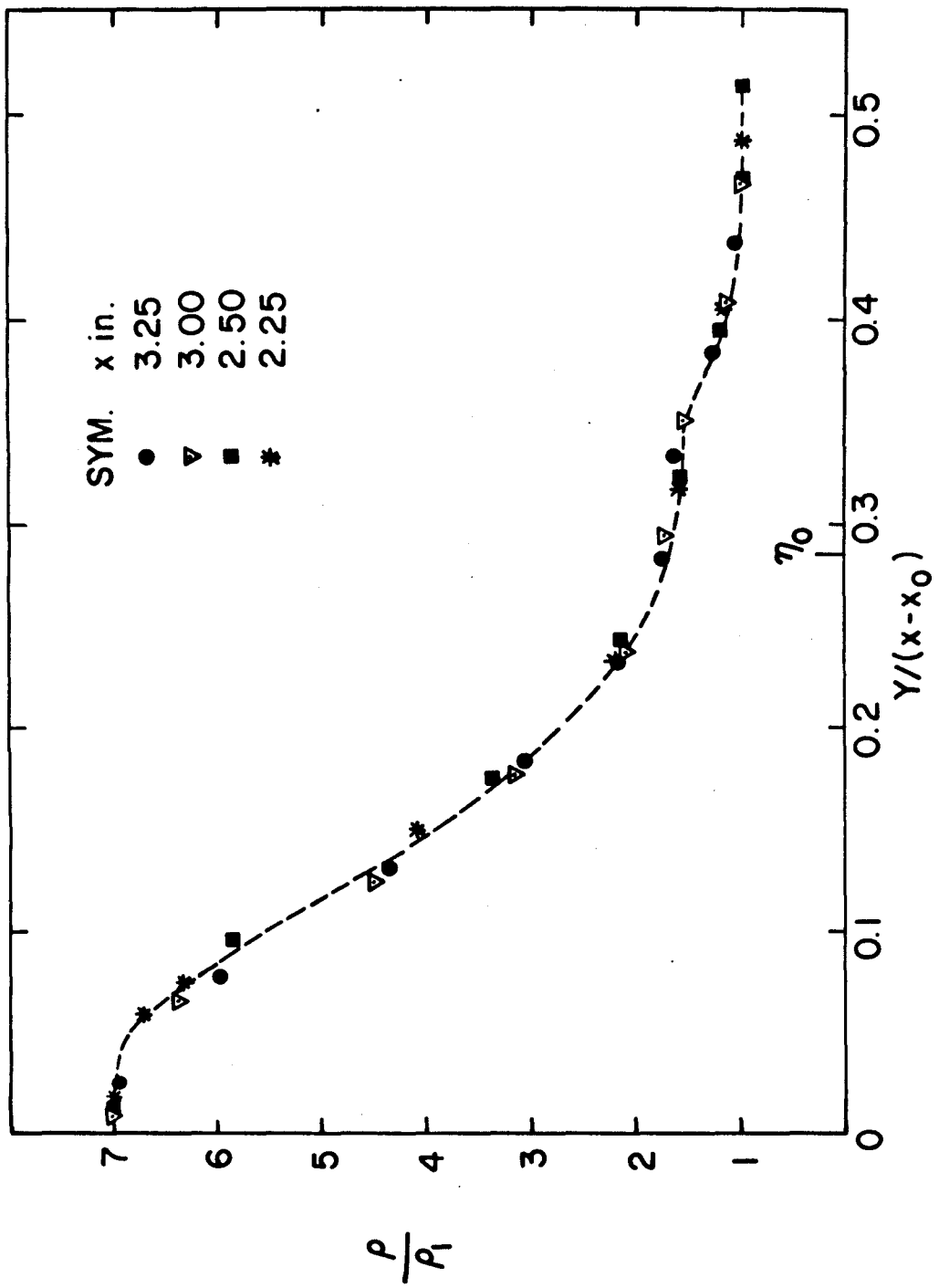

Figure 24. Similarity profile for density. Tank pressure = 4 atm; $\alpha = -0.18$; $x_o = 0.75$".

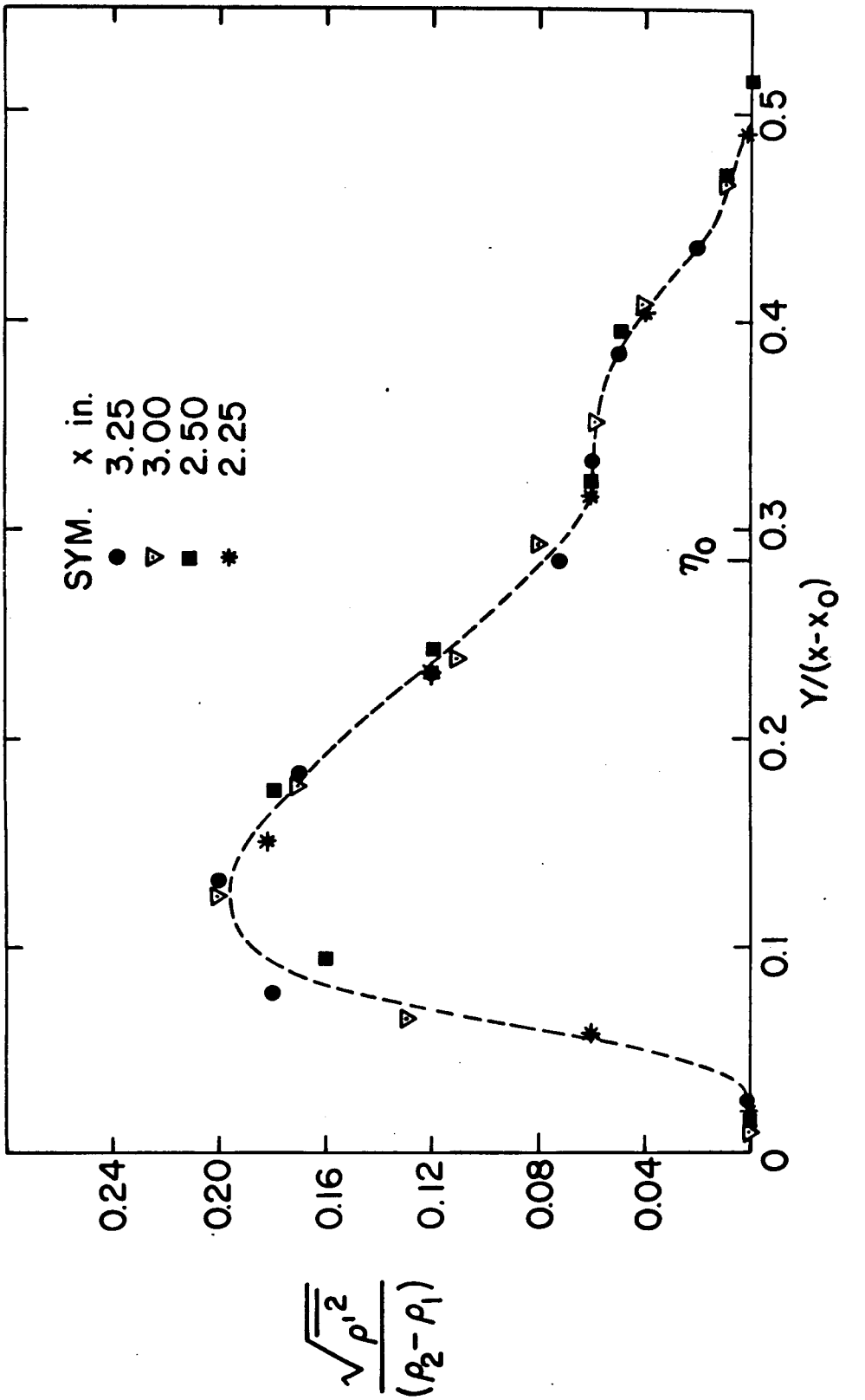

Figure 25. Self-preservation for rms density fluctuations. Tank pressure = 4 atm; $\alpha = -0.18$; $x_o = 0.75$".

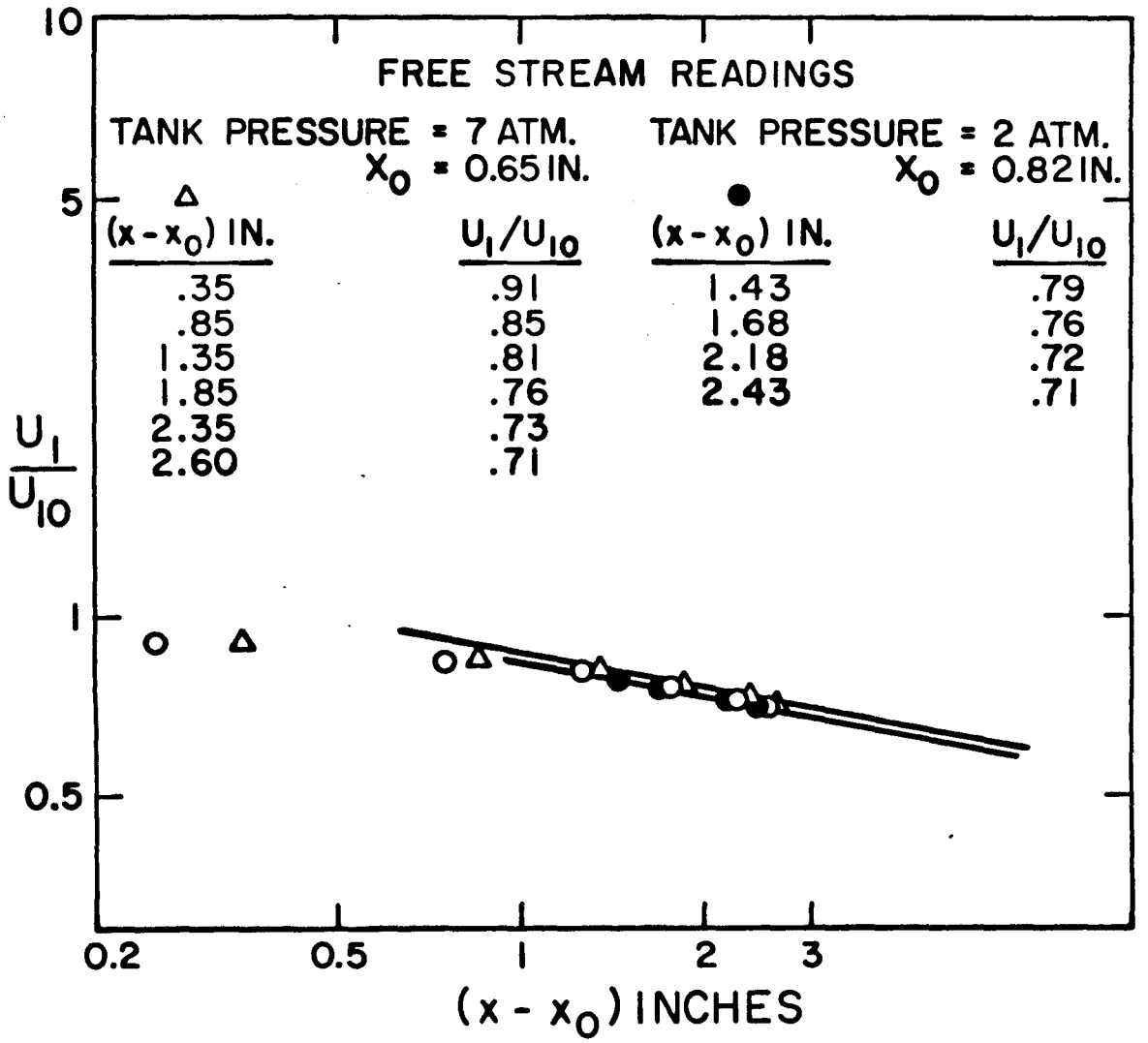

Figure 26. Free stream velocity decay as a function of downstream position. Tank pressure = 7 and 2 atm; α = -0.18.

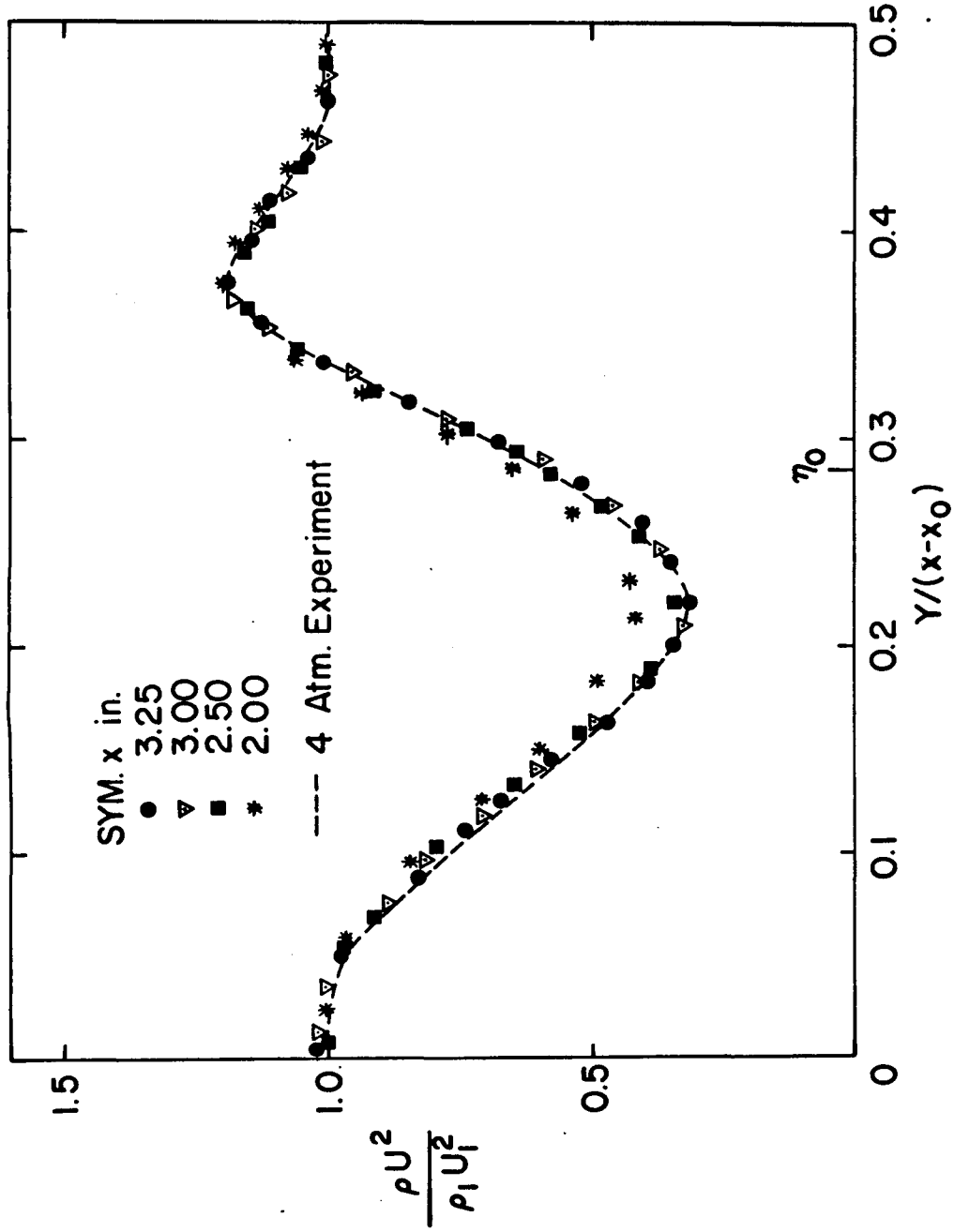

Figure 27. Similarity profile for dynamic pressure. Tank pressure = 7 atm; $\alpha = -0.18$; $x_o = 0.65$".

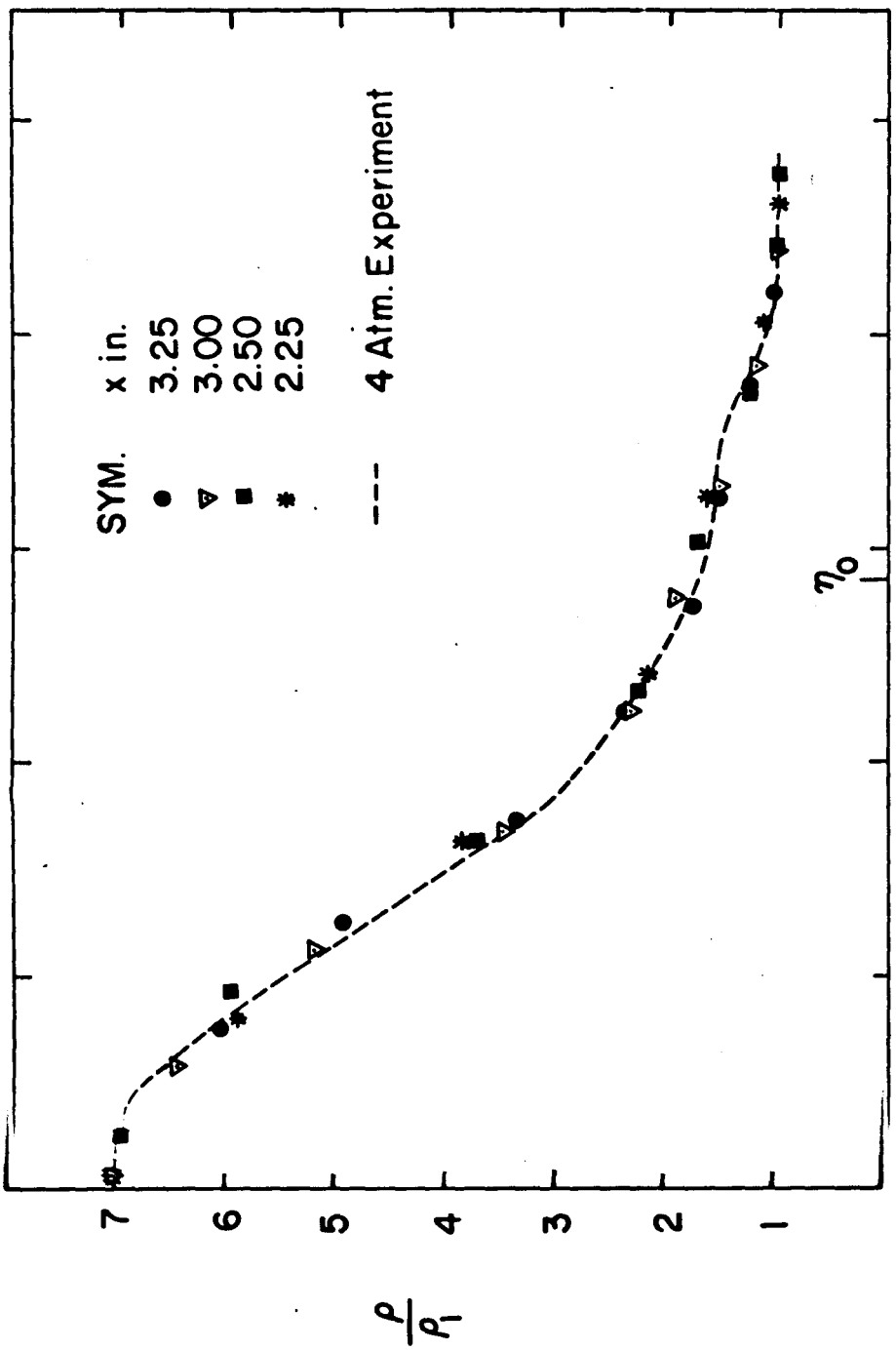

Figure 28. Similarity profile for density. Tank pressure = 7 atm; $\alpha = -0.18$; $x_o = 0.65$".

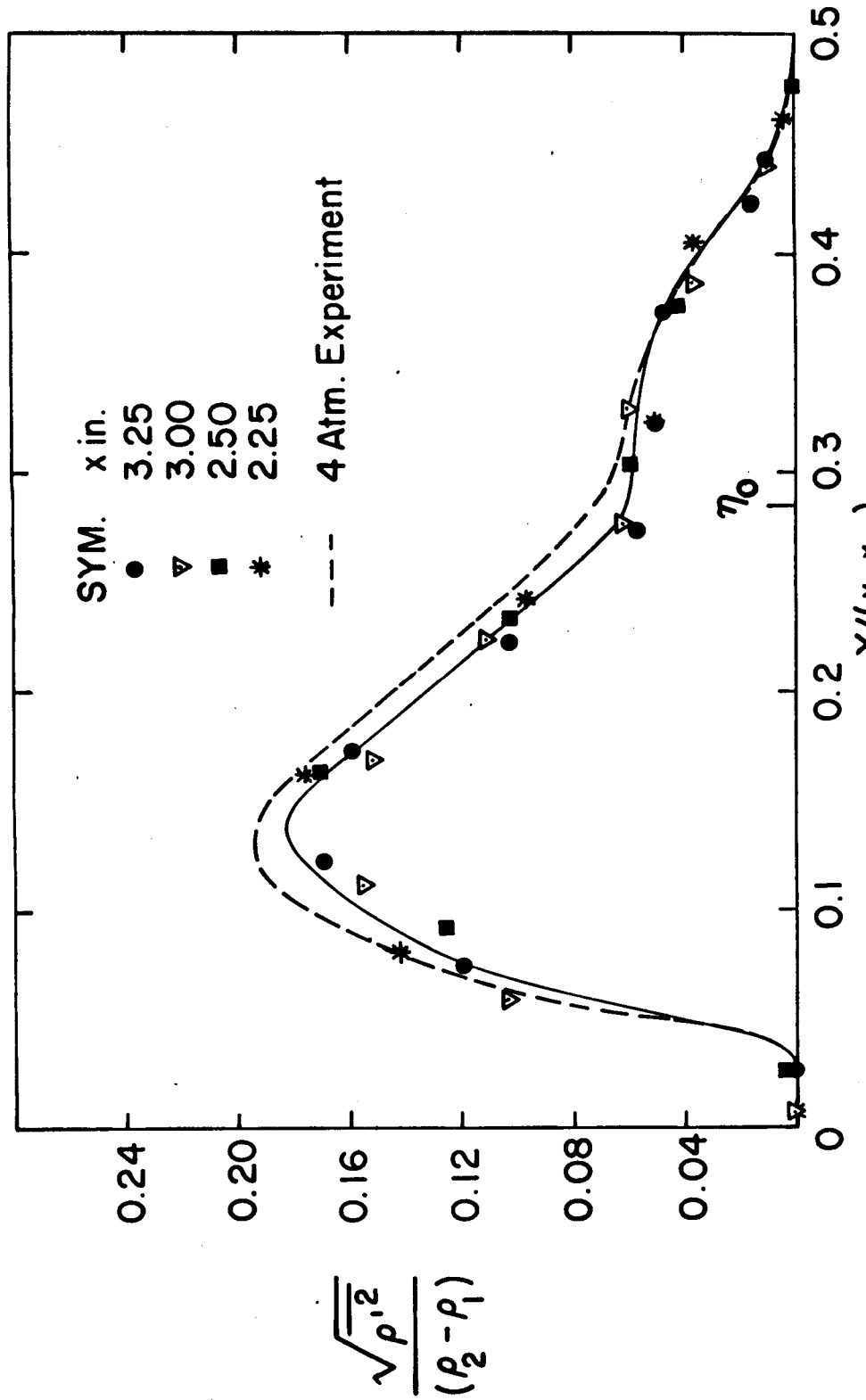

Figure 29. Self-preservation for rms density fluctuations. Tank pressure = 7 atm; $\alpha = -0.18$; $x_o = 0.65$".

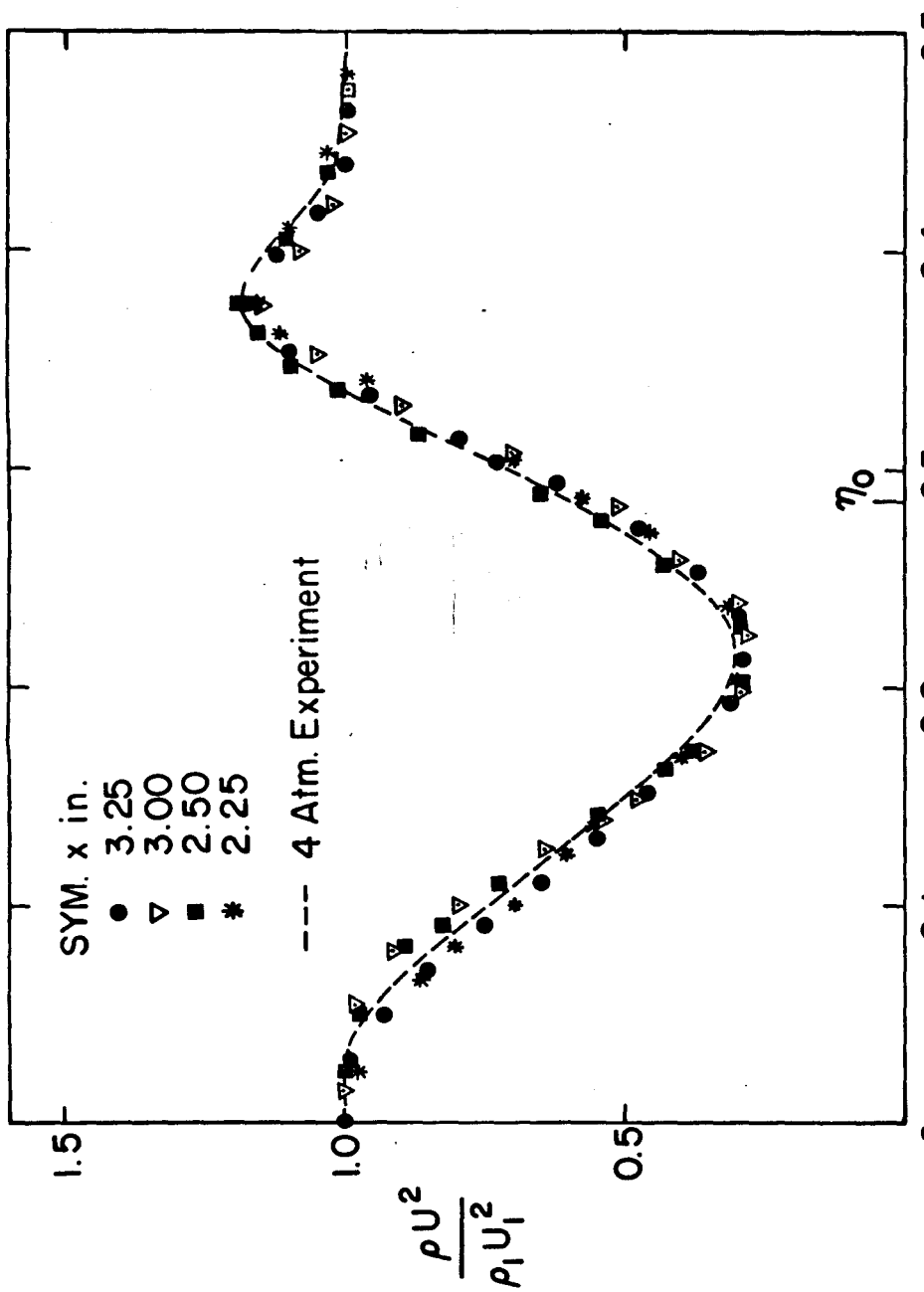

Figure 30. Similarity profile for dynamic pressure. Tank pressure = 2 atm; $\alpha = -0.18$; $x_o = 0.82$".

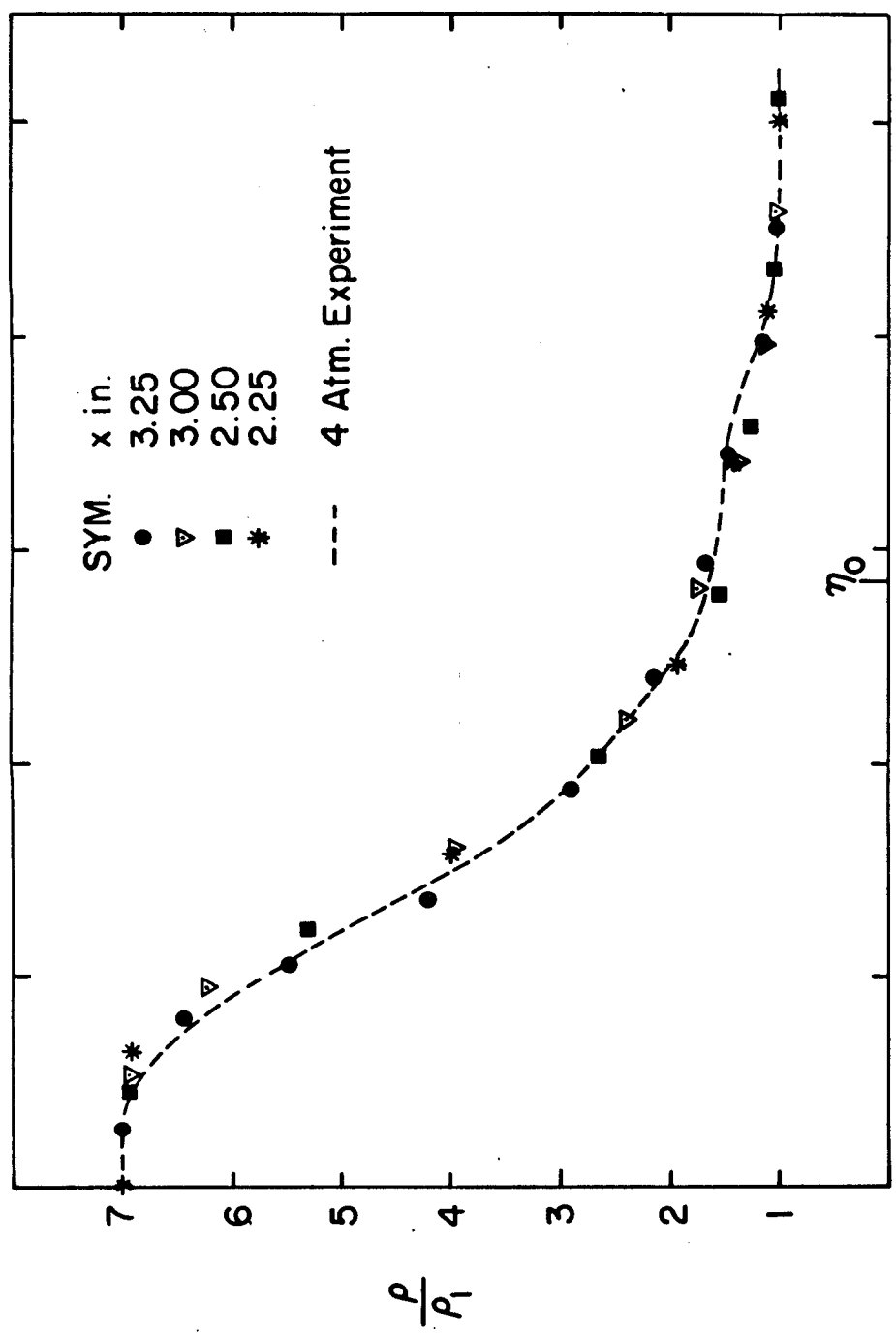

Figure 31. Similarity profile for density. Tank pressure = 2 atm; $\alpha = -0.18$; x_o 0.82".

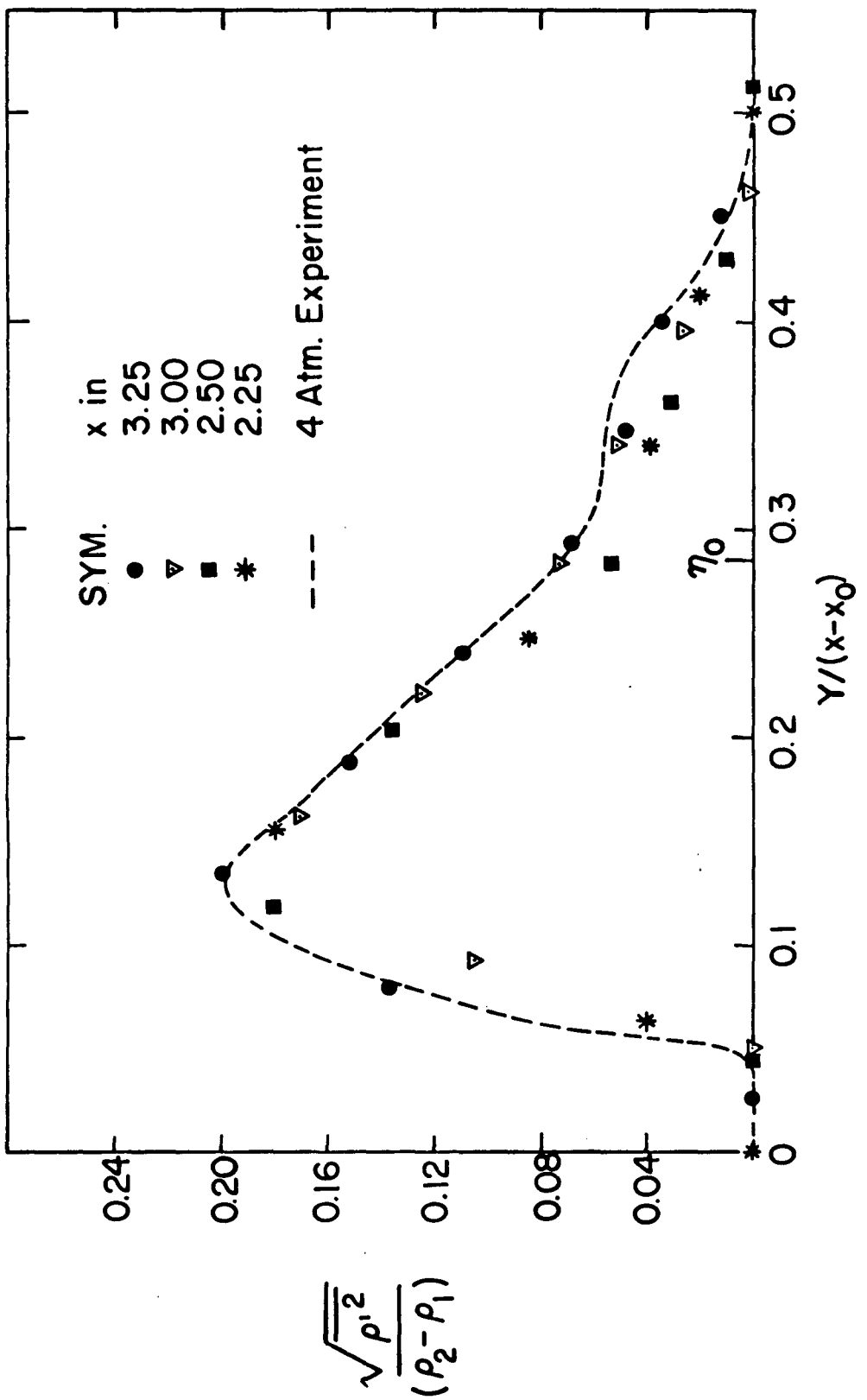

Figure 32. Self-preservation for rms density fluctuations. Tank pressure = 2 atm; α = -0.18; x_o = 0.82".

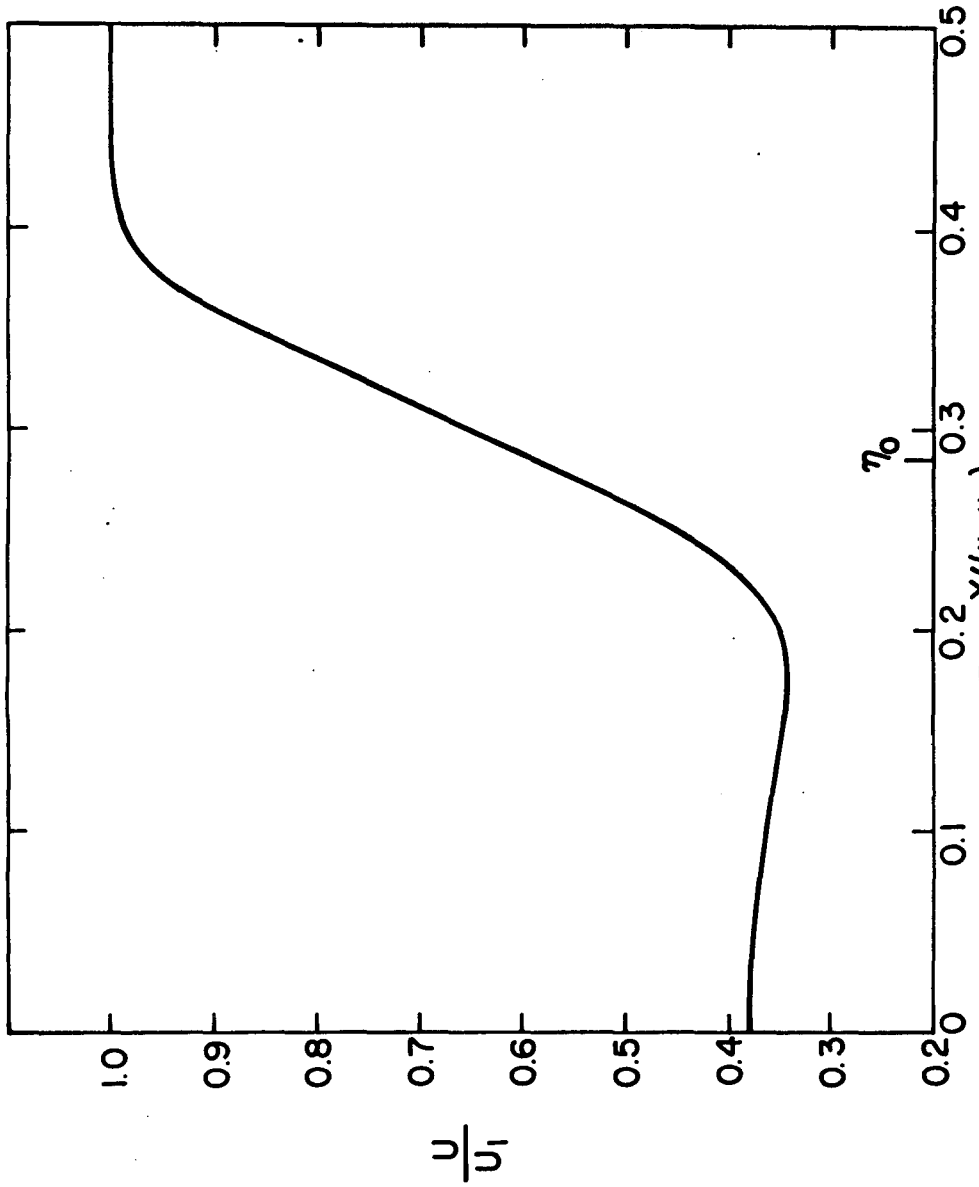

Figure 33. Velocity profile; $\alpha = -0.18$.

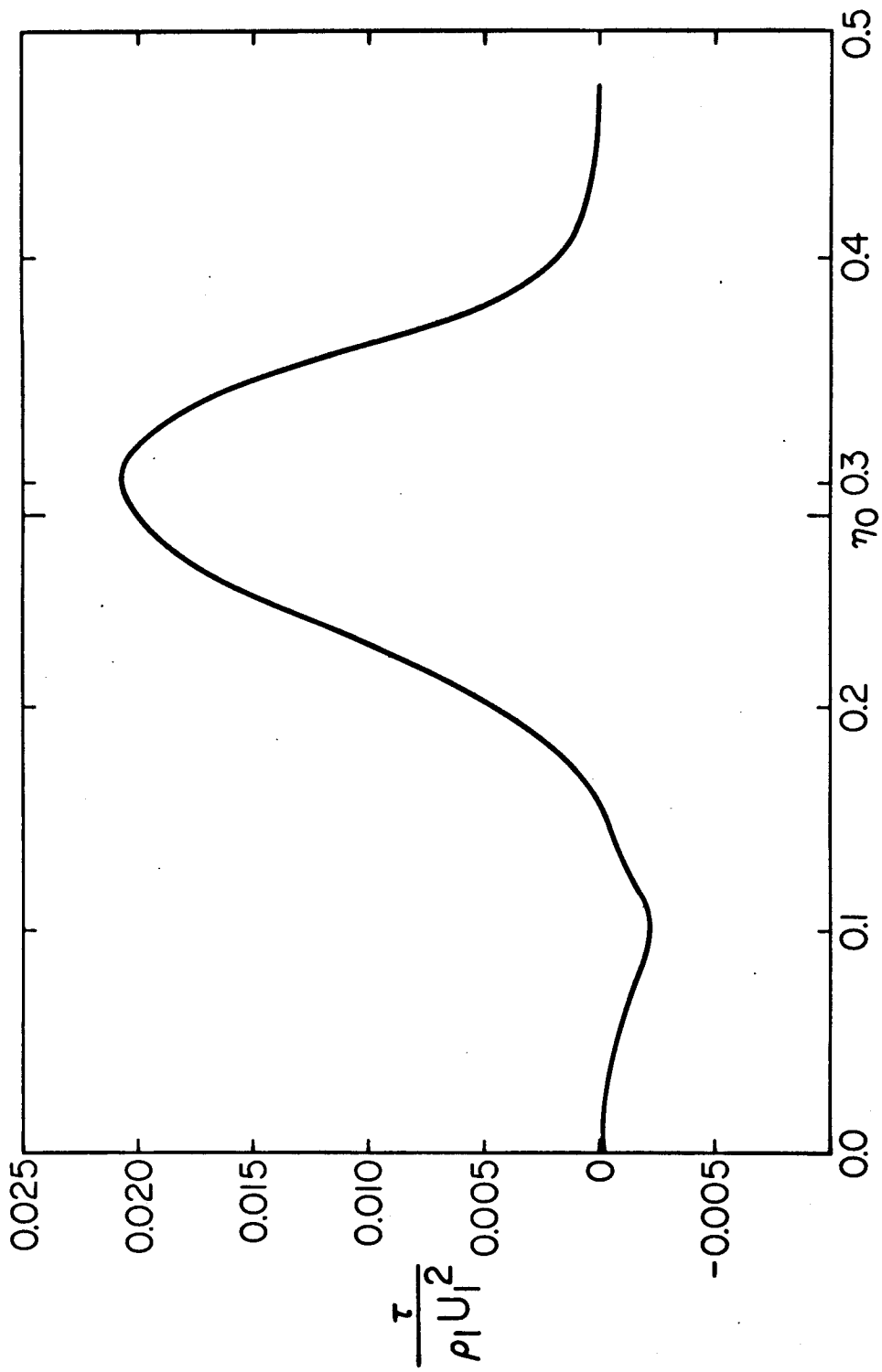

Figure 34. Shear Stress distribution; $\alpha = -0.18$.

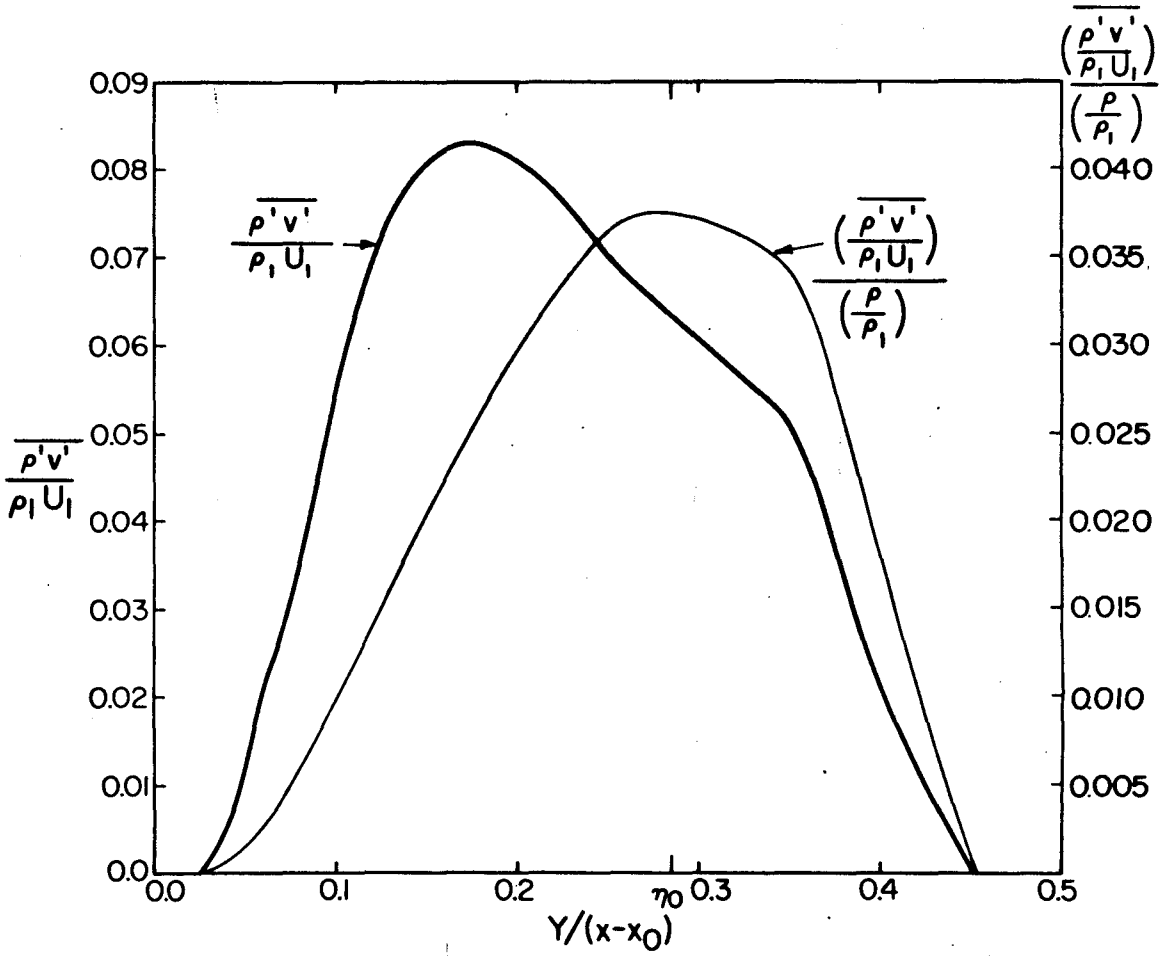

Figure 35. Turbulent mass diffusion distribution; $\alpha = -0.18$.

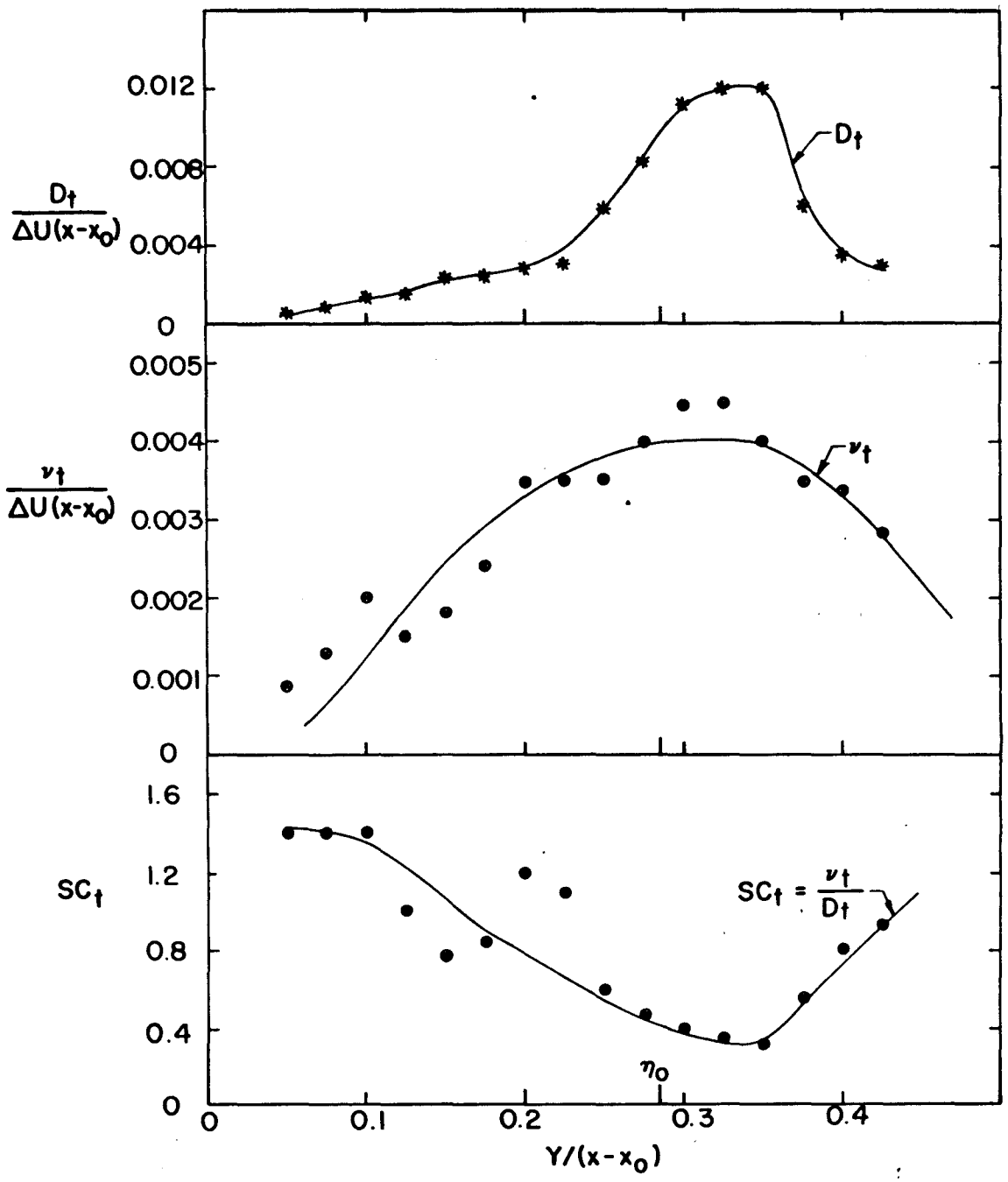

Figure 36. Eddy diffusivity, eddy viscosity, and Schmidt number distributions across the mixing layer; $\alpha = -0.18$.

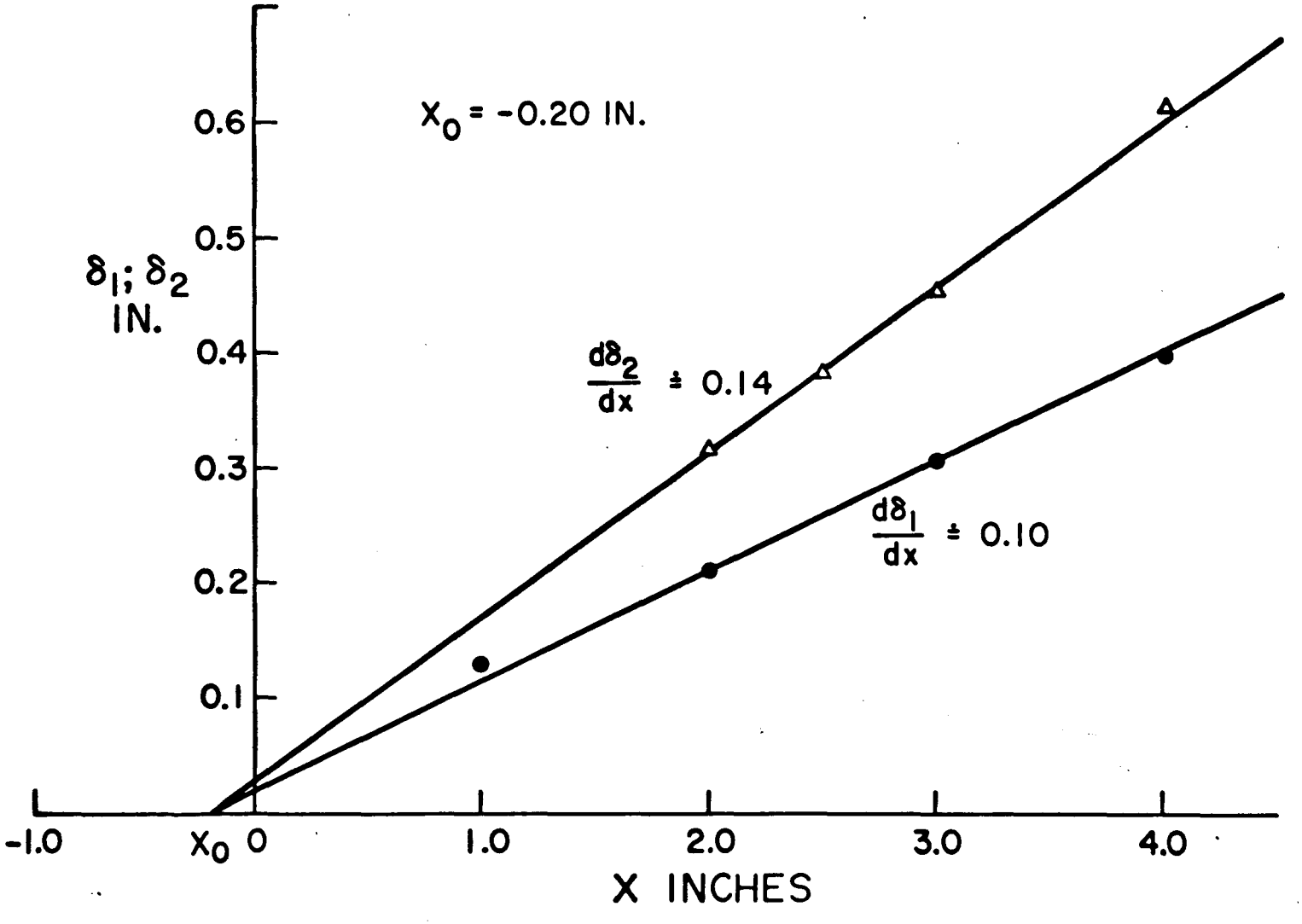

Figure 37. Variation of mixing layer thickness with x coordinate; Tank pressure = 4 atm; α = 0.

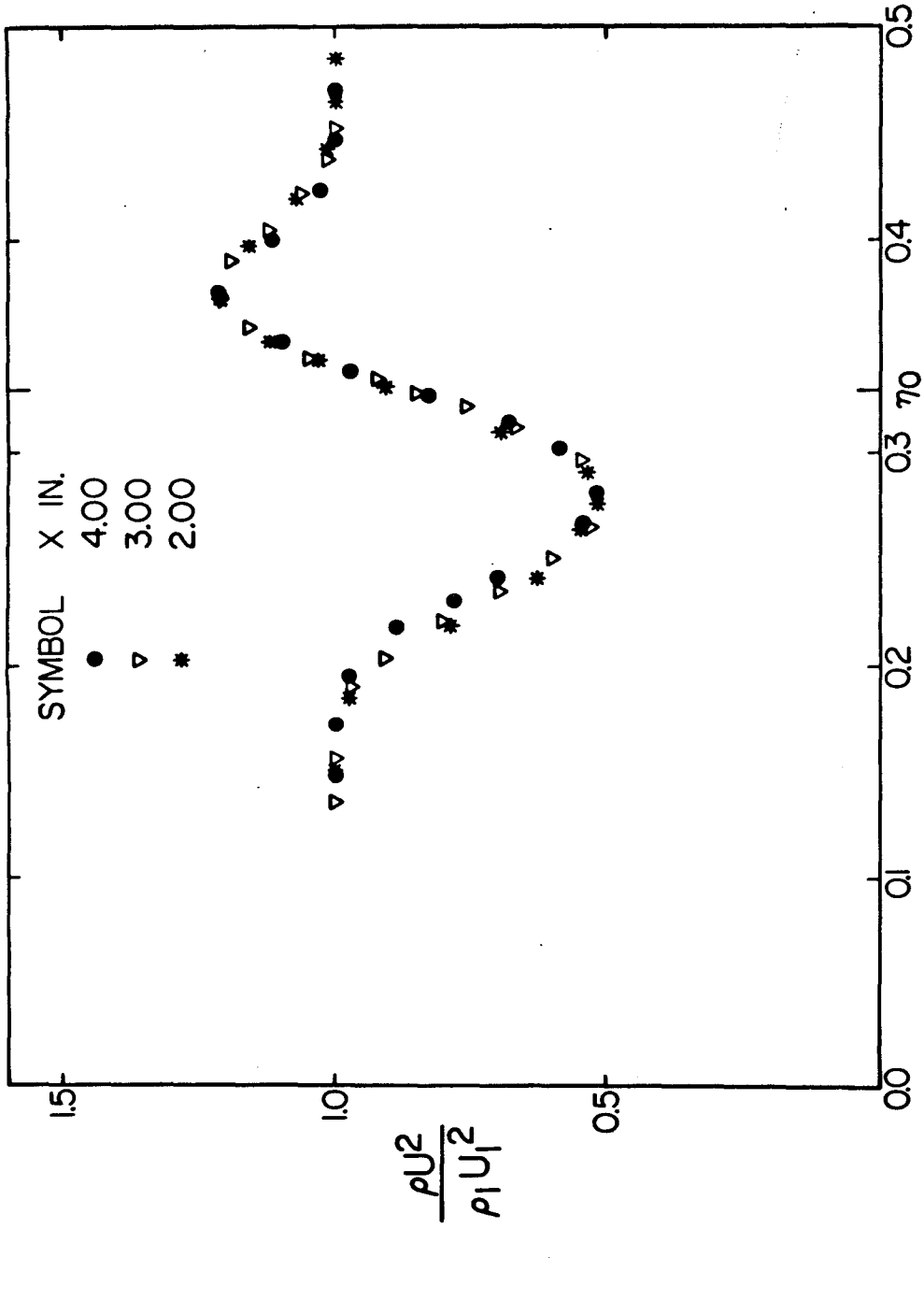

Figure 38. Similarity profile for dynamic pressure. Tank pressure = 4 atm; $\alpha = 0$; $x_o = -0.20''$.

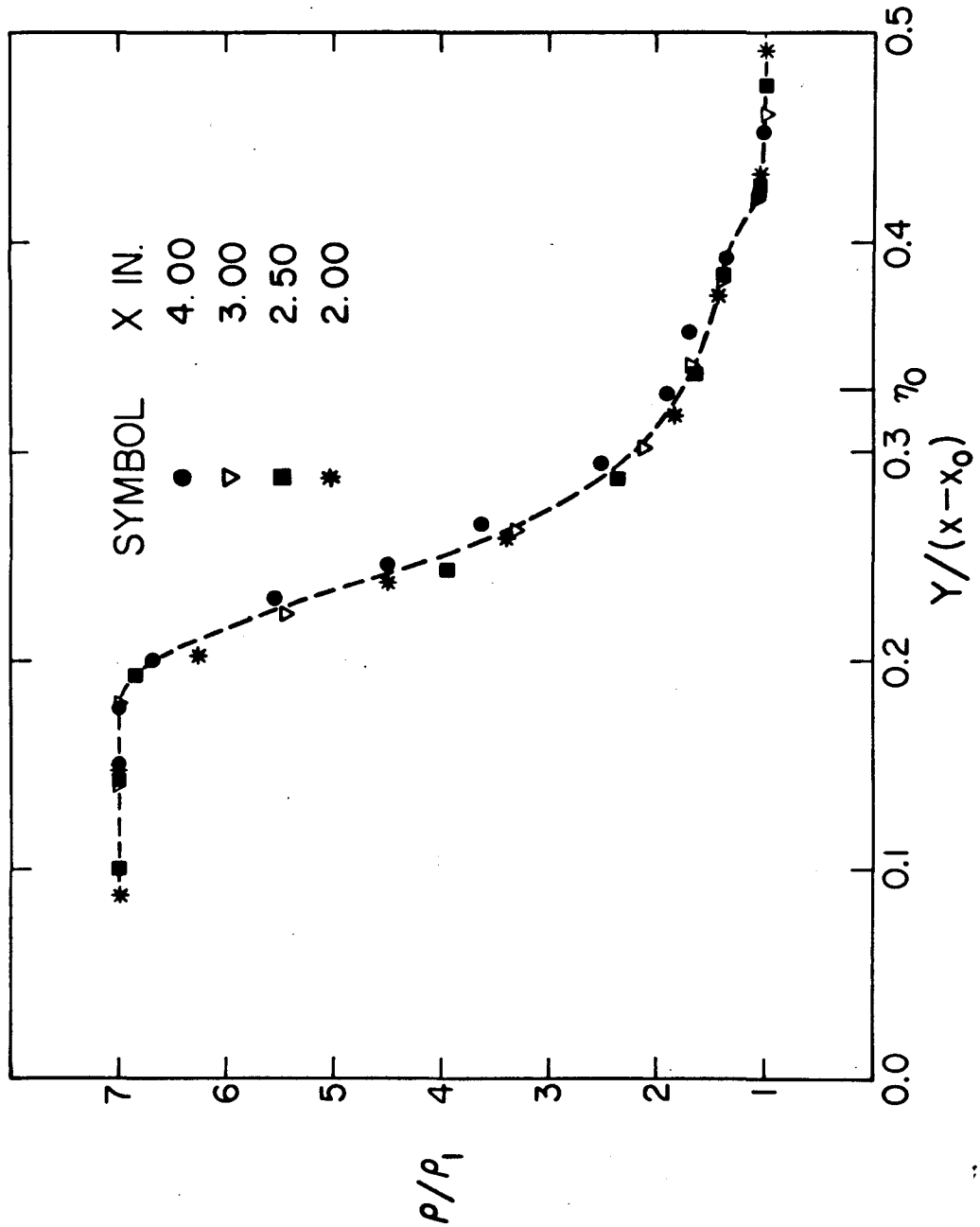

Figure 39. Similarity profile for density. Tank pressure = 4 atm; $\alpha = 0$; $x_o = -0.20''$.

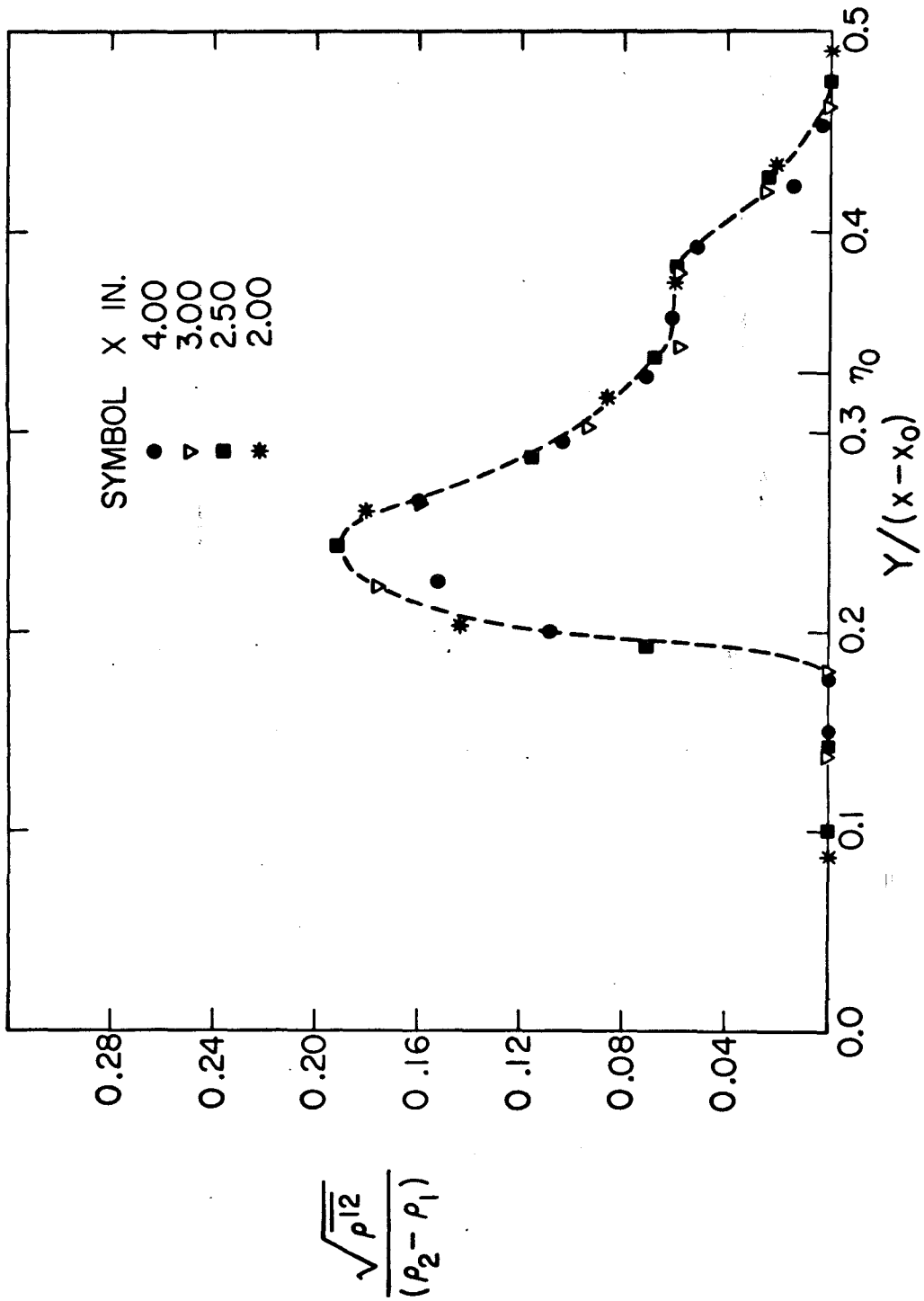

Figure 40. Self-preservation for rms density fluctuations. Tank pressure = 4 atm; $\alpha = 0$; $x_o = -0.20''$.

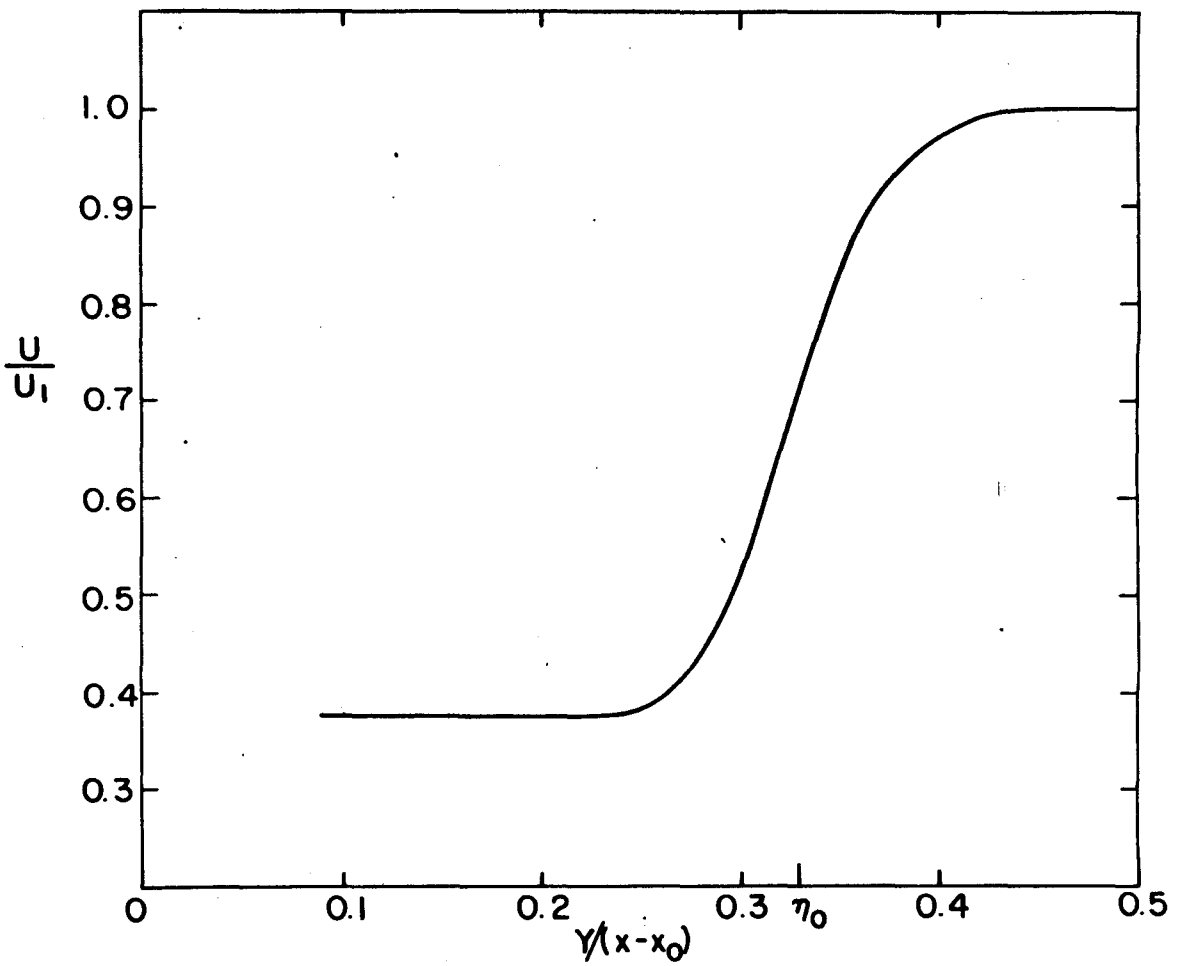

Figure 41. Velocity profile; $\alpha = 0$.

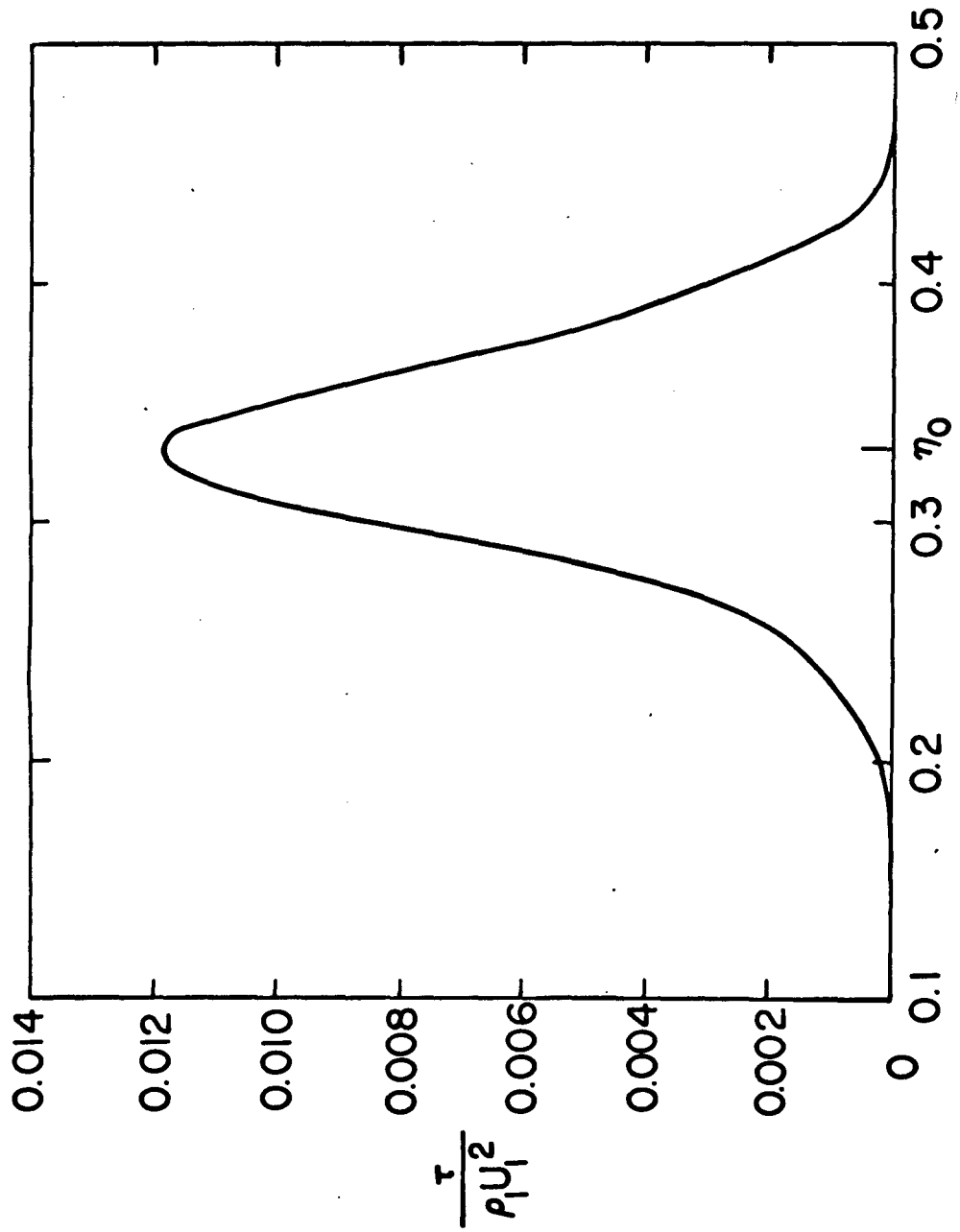

Figure 42. Shear Stress distribution; $\alpha = 0$.

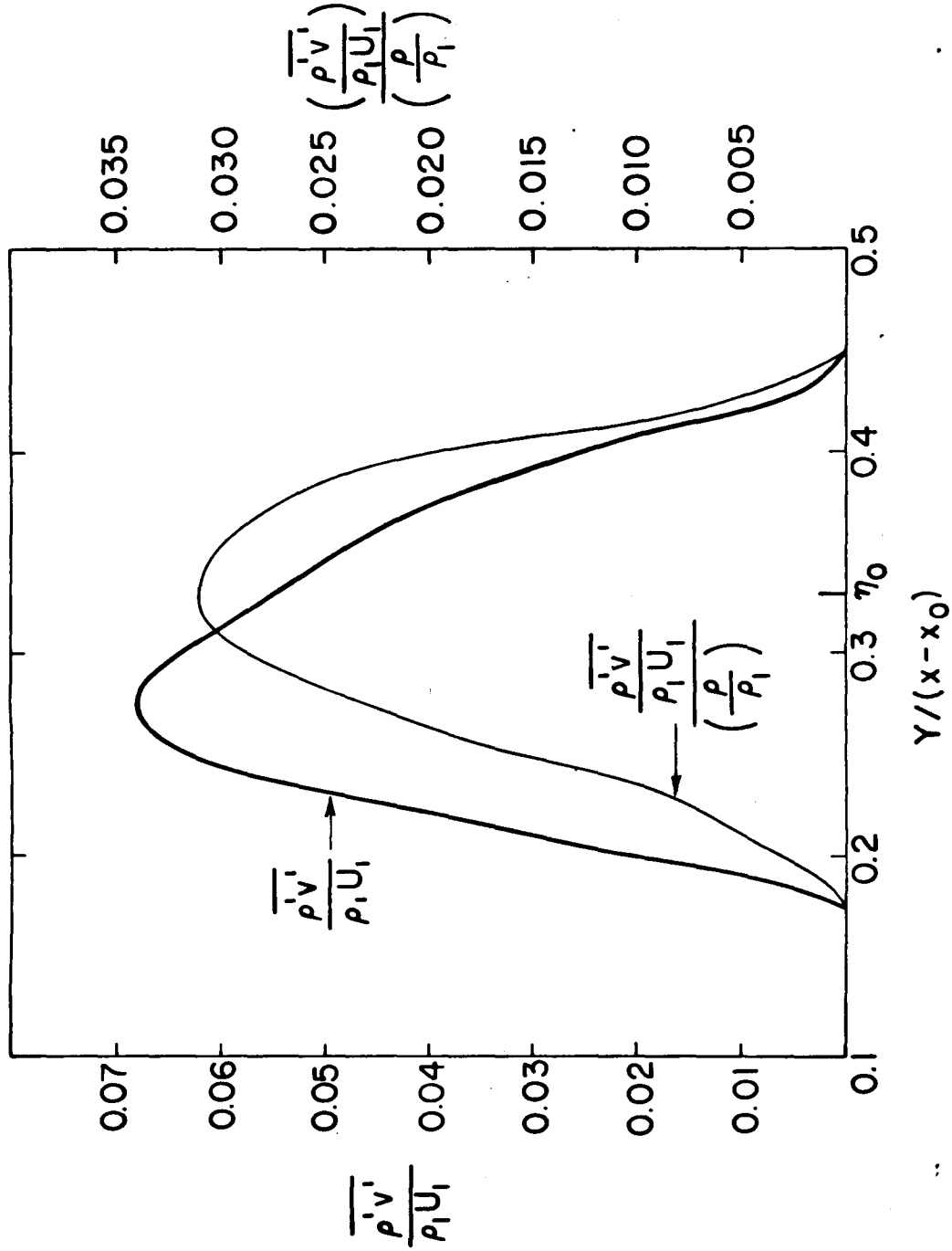

Figure 43. Turbulent mass diffusion distribution; $\alpha = 0$.

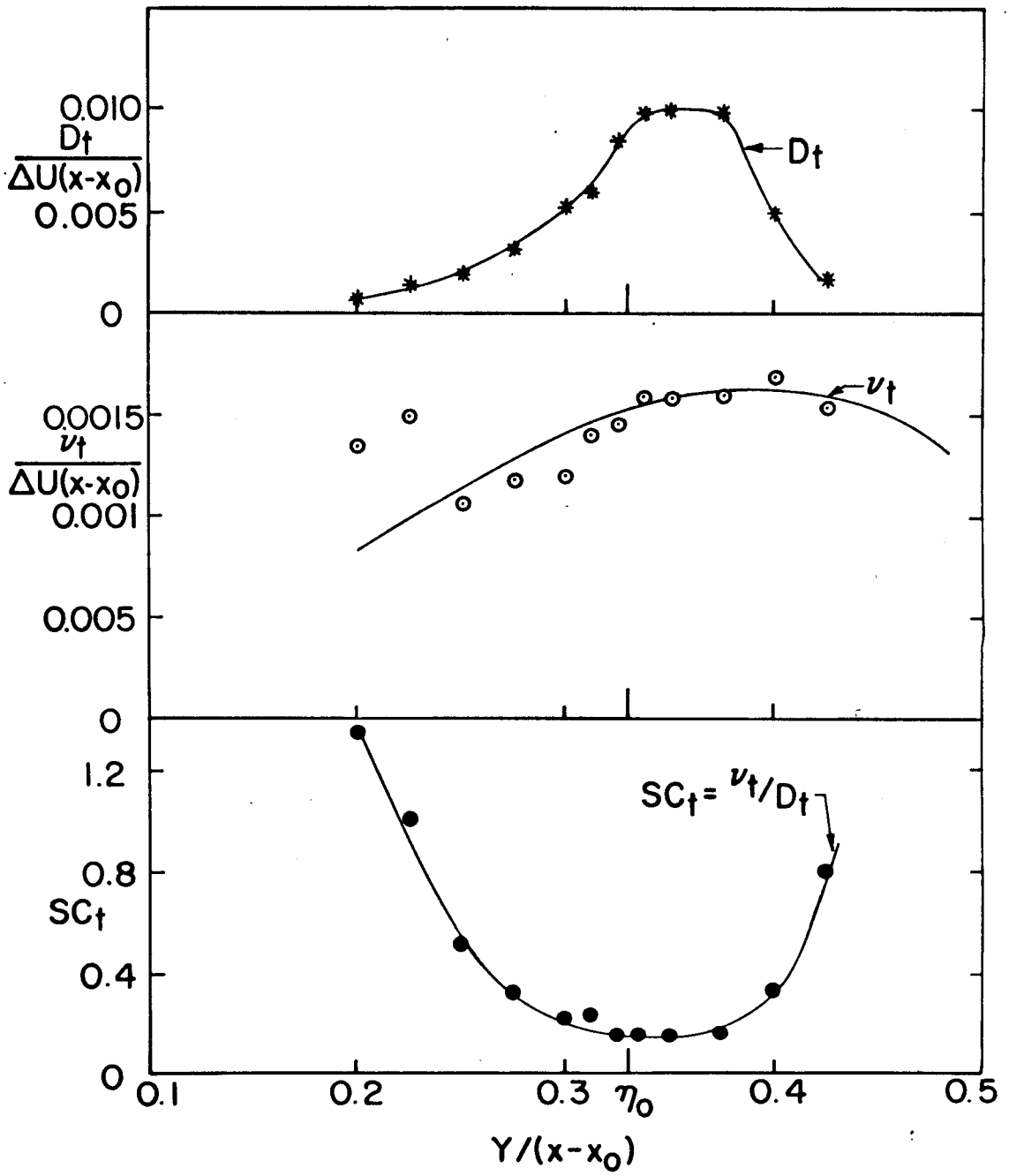

Figure 44. Eddy diffusivity, eddy viscosity, and Schmidt number distribution across the mixing layer; $\alpha = 0$.

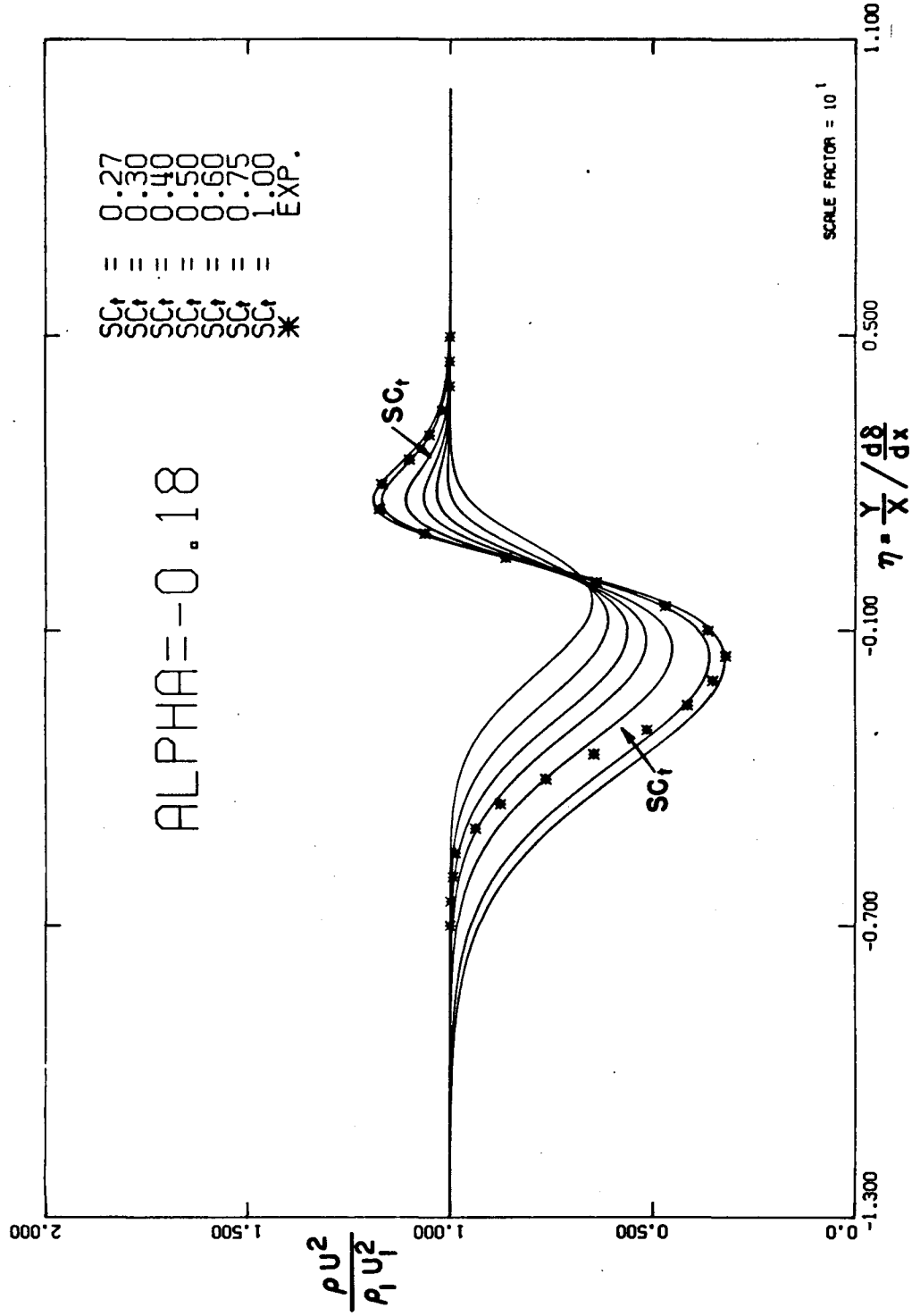

Figure 45. Comparison of numerical solutions with experimental results; dynamic pressure profiles; $\alpha = -0.18$.

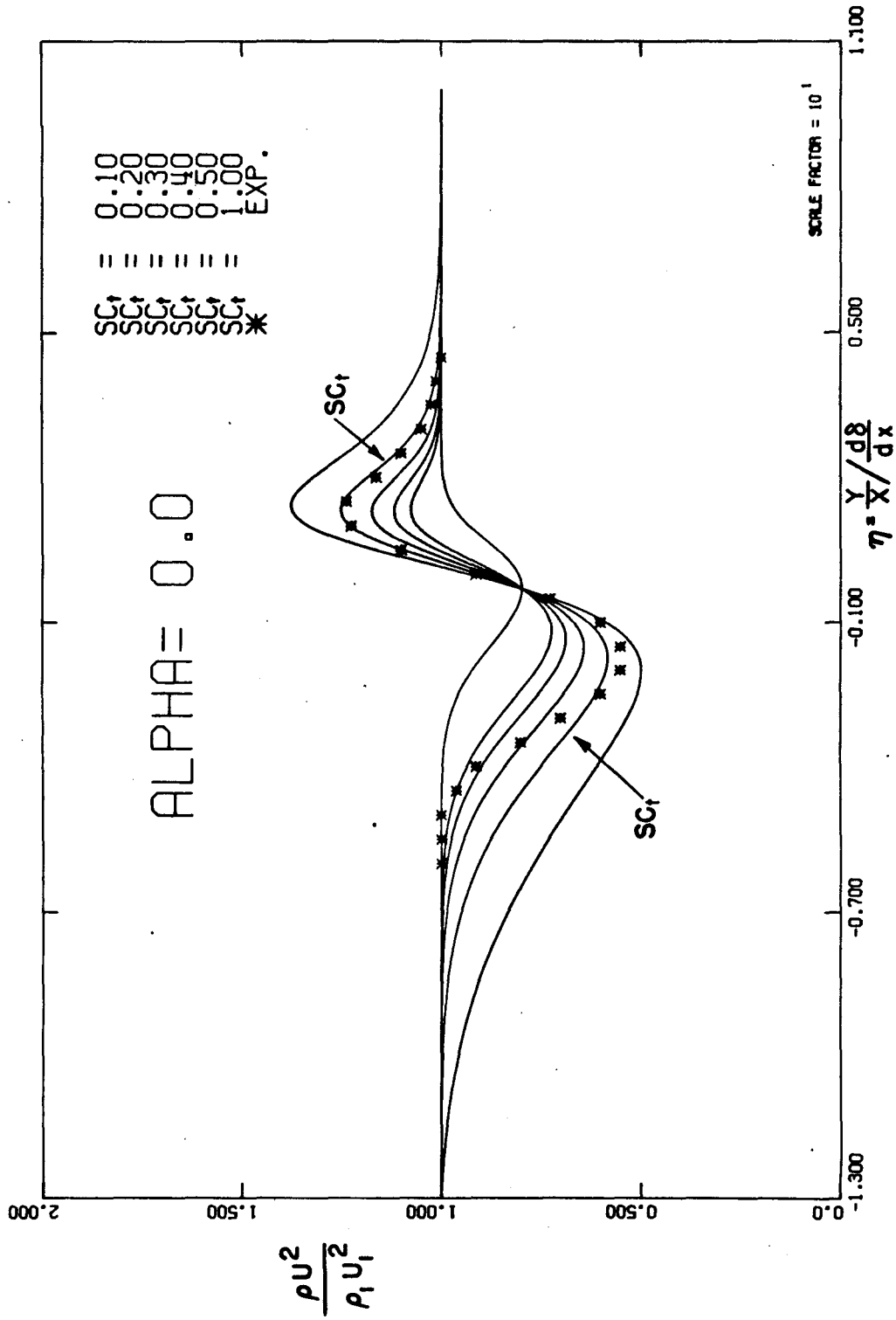

Figure 46. Comparison of numerical solutions with experimental results; dynamic pressure profiles; $\alpha = 0$.

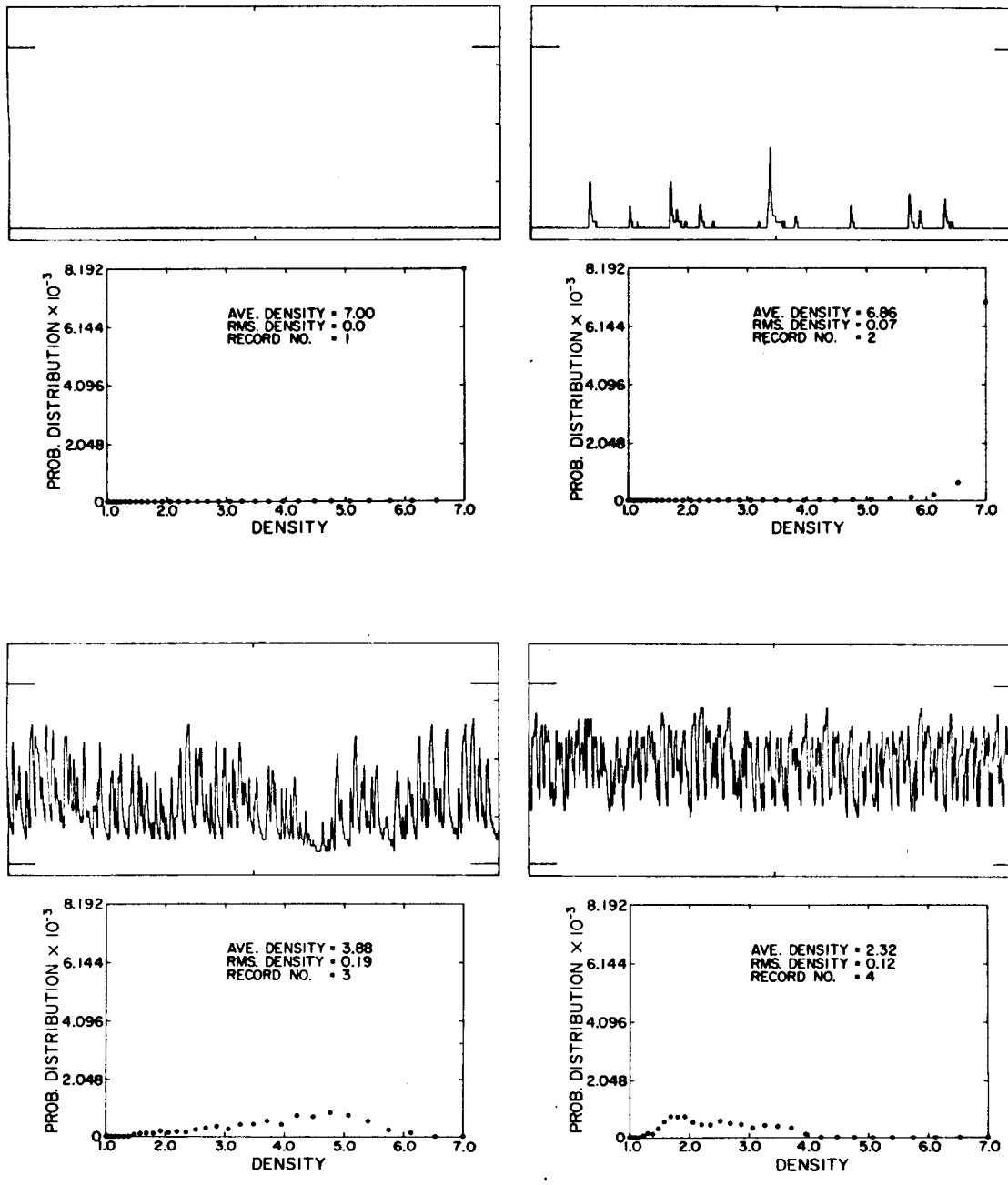

Figure 47. Density traverse; aspirating probe voltage as a function of time, and probability distribution at data points 1, 2, 3 and 4. Tank pressure = 4 atm; α = 0.

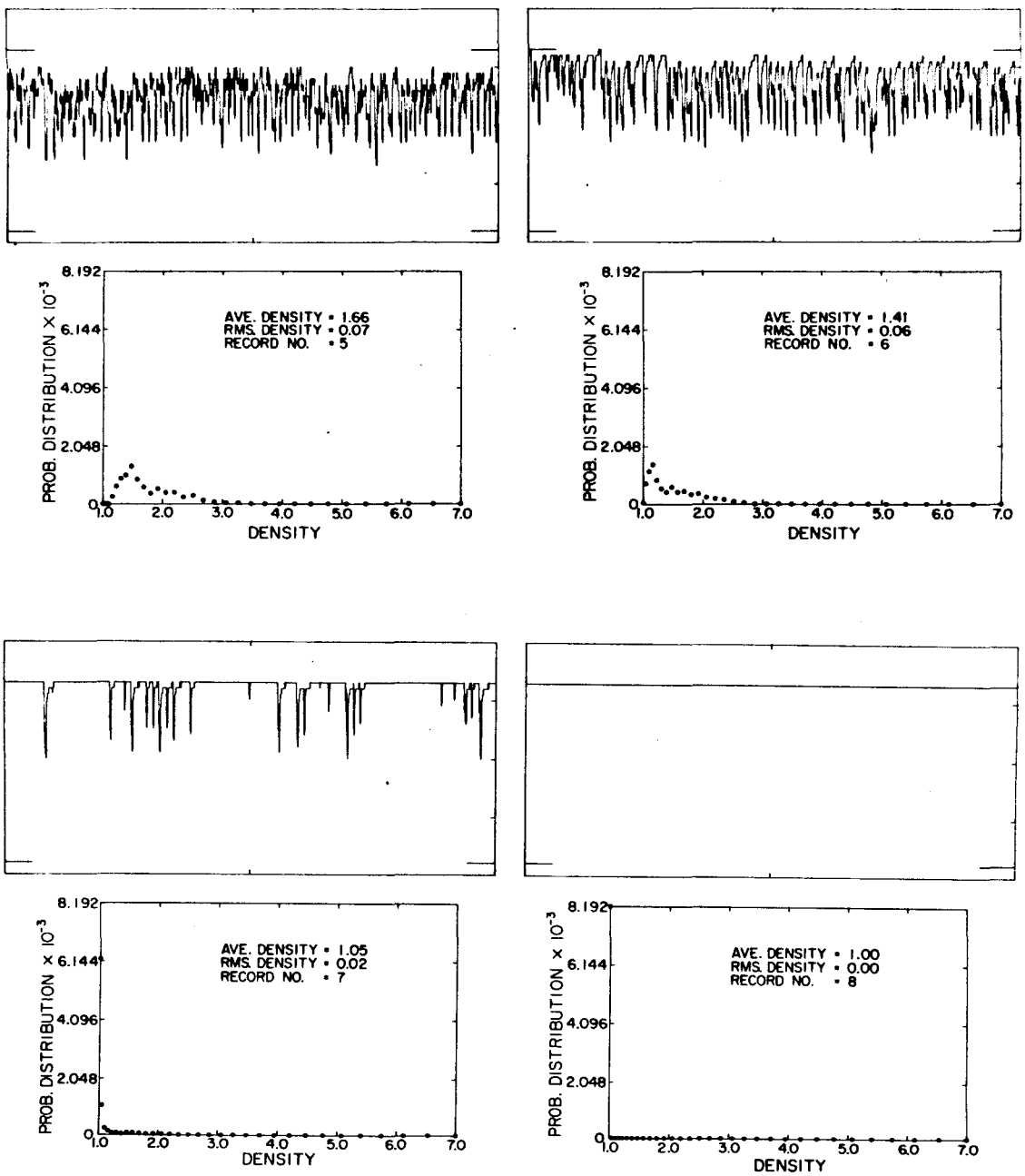

Figure 48. Density traverse; aspirating probe voltage as a function of time, and probability distribution at data points 5, 6, 7 and 8. Tank pressure = 4 atm; α = 0.

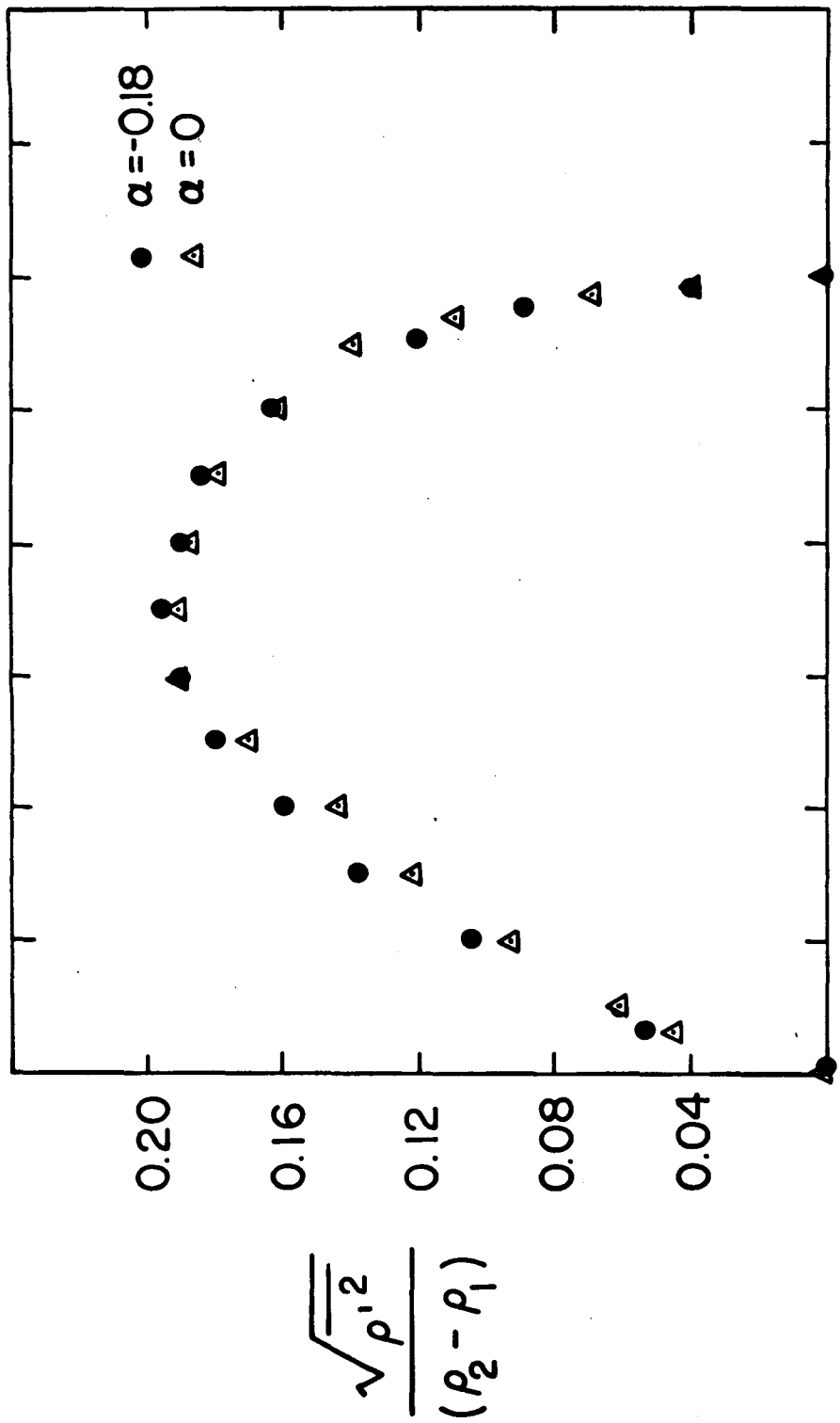

Figure 49. Root-mean-square fluctuations vs. average density for $\alpha = -0.18$ and $\alpha = 0$.